PREPARATION OF BIO-COMPATIBLE BORON NANOPARTICLES AND NOVEL MESOPOROUS SILICA NANOPARTICLES FOR BIO-APPLICATIONS

by

Zhe Gao

A dissertation submitted to the faculty of
The University of Utah
in partial fulfillment of the requirements for the degree of

Doctor of Philosophy

Department of Chemistry

The University of Utah

May 2013

The University of Utah Graduate School

STATEMENT OF DISSERTATION APPROVAL

The dissertation of **Zhe Gao**

has been approved by the following supervisory committee members:

Ilya Zharov	, Chair	**12/07/2012** Date Approved
Scott L. Anderson	, Member	**12/07/2012** Date Approved
Michael H. Bartl	, Member	**12/07/2012** Date Approved
Jennifer S. Shumaker-Parry	, Member	**12/07/2012** Date Approved
Zhigang Fang	, Member	**12/07/2012** Date Approved

and by **Henry S. White**, Chair of the Department of **Chemistry**

and by Donna M. White, Interim Dean of The Graduate School.

ABSTRACT

This dissertation presents the synthesis and characterization of several novel inorganic and hybrid nanoparticles, including the bio-compatible boron nanoparticles (BNPs) for boron neutron capture therapy (BNCT), tannic acid-templated mesoporous silica nanoparticles and degradable bridged silsesquioxane silica nanoparticles.

Chapter 1 provides background information of BNCT and reviews the development of design and synthesizing silica nanoparticles and the study of silica material degradability.

Chapter 2 describes the preparation and characterization of dopamine modified BNPs and the preliminary cell study of them. The BNPs were first produced via ball milling, with fatty acid on the surface to stabilize the combustible boron elements. This chapter will mainly focus on the ligand-exchange strategy, in which the fatty acids were replaced by non-toxic dopamines in a facile one-pot reaction. The dopamine-coated BNPs (DA-BNPs) revealed good water dispersibility and low cytotoxicity.

Chapter 3 describes the synthesis of tannic acid template mesoporous silica nanoparticles (TA-TEOS SiNPs) and their application to immobilize proteins. The monodispersed TA SiNPs with uniform pore size up to approximately 13 nm were produced by utilizing tannic acid as a molecular template. We studied the influence of TA concentration and reaction time on the morphology and pore size of the particles. Furthermore, the TA-TEOS particles could subsequently be modified with amine groups

allowing them to be capable of incorporating imaging ligands and other guest molecules. The ability of the TA-TEOS particles to store biomolecules was preliminarily assessed with three proteins of different charge characteristics and dimensions. The immobilization of malic dehydrogenase on TA-TEOS enhanced the stability of the enzyme at room temperature.

Chapter 4 details the synthesis of several bridged silsesquioxanes and the preparation of degradable hybrid SiNPs via co-condensation of bridged silsesquioxanes with tetraethoxysilane. *In vivo* studies show that the solid SiNPs accumulate in many organs due to the lack of degradability. The aim of our work is to address this shortcoming by producing novel degradable SiNPs. Bridged silsesquioxanes were used as the precursors of the particles, and upon cleavage of the carbamate groups when brought into contact with aqueous media, the particles degraded into porous structures.

TABLE OF CONTENTS

ABSTRACT iii

LIST OF ABBREVIATIONS viii

LIST OF FIGURES xiv

LIST OF TABLES xviii

ACKNOWLEDGEMENTS xix

CHAPTERS

1. INTRODUCTION 1

1.1 Aim and significance 1
1.2 Boron neutron capture therapy 4
1.3 Silica nanoparticles 9
1.3.1 Silica nanoparticle synthesis 10
1.3.2 Co-condensation for preparation of silica nanoparticles 11
1.3.3 Surface modification of silica nanoparticles 12
1.4 Mesoporous silica nanoparticles 12
1.4.1 Mechanism of mesoporous silica materials formation 13
1.4.2 Synthetic routes to mesoporous silica materials 14
1.4.3 Biomedical applications of mesoporous silica materials 16
1.5 Degradation of silica nanoparticles 17
1.6 Thesis overview 20
1.7 References 22

2. BIO-COMPATIBLE BORON NANOPARTICLES 29

2.1 Introduction 29
2.2 Experimental section 31
2.2.1 Chemicals and instruments 31
2.2.2 Preparation of air-stable boron nanoparticles 32
2.2.3 Ligand exchange reaction 33
2.2.4 Purification of boron nanoparticles 34
2.2.5 Mass spectrometry analysis of the particles 34
2.2.6 Attachment of fluorescent tags 35

2.2.7 PEGylation of boron nanoparticles 35
2.2.8. Preliminary cell study 36
2.3 Results and discussion 37
2.3.1 Preparation and characterization of dopamine-modified boron nanoparticles 37
2.3.2 Surface modification of DA-BNPs 47
2.3.3 The DA-OA-BNPs 49
2.3.4 Preliminary cell toxicity study of DA-BNPs† 52
2.4 Conclusion 57
2.5 References 58

3. TANNIC ACID-TEMPLATED LARGE-PORE MESOPOROUS SILICA NANOPARTICLES 61

3.1 Introduction 61
3.2 Experimental 63
3.2.1 Chemicals and instruments 63
3.2.2 Preparation of tannic acid-templated mesoporous silica nanoparticles 65
3.2.3 Preparation of 240 nm silica spheres 66
3.2.4 Degradation study of TA-TEOS 66
3.2.5 Surface modification of tannic acid-templated mesoporous silica nanoparticles 67
3.2.6 Preliminary study of protein adsorption 68
3.2.7 Enzyme immobilization by TA-TEOS 68
3.2.8 Enzyme activity test 69
3.3 Results and Discussion 70
3.3.1 Synthesis and characterization of TA-TEOS NPs 70
3.3.2 Degradability of TA-TEOS NPs 82
3.3.3 Surface modification of TA-TEOS 84
3.3.4 Preliminary study of physical adsorption of proteins 87
3.3.5 Immobilization of mitochondrial malic dehydrogenase 94
3.4 Conclusion 100
3.5 References 101

4. DEGRADABLE BRIDGED SILSESQUIOXANE SILICA NANOPARTICLES 105

4.1 Introduction 105
4.2 Experimental 106
4.2.1 Chemicals and instruments 106
4.2.2 Synthesis of chloromethyl ester bridged (3-aminopropyl) triethoxysilane 108
4.2.4 Preliminary study of degradation behavior of CME-APTES silica spheres 109
4.2.5 Synthesis of ethylene glycol bridged isocyanatopropyltriethoxysilane 109
4.2.6 Synthesis of ethylene glycol bridged isocyanatopropyltriethoxysilane particles 110
4.2.7 Synthesis of sorbitol-bridged isocyanatopropyltriethoxysilane 110

4.2.8 Synthesis of sorbitol bridged isocyanatopropyltriethoxysilane SiNPs..... 111
4.2.9 Synthesis of 340 nm SiNPs 112
4.2.10 Molybdenum blue colorimetric experiment 112
4.3 Results and Discussion 113
4.3.1 Synthesis of bridged silsesquioxanes 113
4.3.2 Synthesis and characterization of CME-APTES SiNPs 114
4.3.3 Degradation of CME-APTES SiNPs 118
4.3.4 ICPTES-EG SiNPs 122
4.3.5 Synthesis and characterization of ICPTES-Sorbitol SiNPs 123
4.3.6 Degradability of ICPTES-Sorbitol SiNPs 128
4.4 Conclusion 139
4.5 References 140

5. CONCLUSIONS AND FUTURE DIRECTIONS 143

5.1 Conclusions 143
5.2 Future directions 144
5.3 References 147

LIST OF ABBREVIATIONS

2D	two-dimensional
ΔC	Concentration Gradient
β-NADH/NAD	β-Nicotinamide Adenine Dinucleotide Hydrate/ Nicotinamide Adenine Dinucleotide
δ	Chemical Shift
λ_{max}	Wavelength of Maximum Absorbance
µg, mg, g	Microgram, Milligram, Gram
µM, mM, M	Micromolar, Millimolar, Molar
µm, nm, cm	Micrometer, Nanometer, Centimeter
µL, mL, L	Microliter, Milliliter, Liter
µmol, mmol, mol	Micromole, Millimole, Mole
-COOH	Carboxylic Acid
-OH	Hydroxyl group
°C	Celsius Degree
APTES	3-(Aminopropyl) triethoxysilane
BET	Brunauer-Emmett-Teller
BHb	Bovine Hemogobin
BJH	Barrett-Joyner-Halenda
BME	β-mercaptoethanol

BNCT	Boron Neutron Capture Therapy
BNP	Boron Nanoparticle
BPA	Boronophenylalanine
BSA	Bovine Serum Albumin
BSH	Sodium borocaptate
C	Concentration
$CaCl_2$	Calcium chloride
$CDCl_3$	Deuterochloroform
CH_2Cl_2	Dichloromethane
CH_3CN	Acetonitrile
$CHCl_3$	Chloroform
CME	Chloromethyl ester
CME-APTES	Chloromethyl ester bridged (3-aminopropyl) triethoxysilane
CNT	Carbon Nanotube
CTAB	Cetyltrimethylammonium Bromide
Cu	Copper
DA	Dopamine
DA-BNPs	Dopamine coated Boron Nanoparticles
DLS	Dynamic Light Scattering
DMF	*N*,*N*-Dimethylformamide
EG	Ethylene Glycol
EPR	Enhanced Permeability and Retention
Eq	Equation

EtOH	Ethanol
fcc	Face Centered Cubic
Fe	Iron
h	Hour
H	Proton
HCl	Hydrogen Chloride
H_2O	Water
HPLC	High Performance Liquid Chromatography
IR	Infrared
ICPTES	3-isocyanatopropyltriethoxysilane
ICPTES-EG	Ethylene glycol bridged 3-isocyanatopropyltriethoxysilane
ICPTES-sorbitol	Sorbitol bridged 3-isocyanatopropyltriethoxysilane
K_2CO_3	Potassium Carbonate
KCl	Potassium Chloride
$K_2HPO_4 \cdot 3H_2O$	Potassium phosphate dibasic trihydrate
KH_2PO_4	Potassium phosphate monobasic
k_B	Boltzmann Constant
kb	Kilobase
kDa	Kilodalton
LET	Linear Energy Transfer
Lz	Lysozyme
MΩ	Megaohm
MeOH	Methanol

$MgSO_4$	Magnesium Sulfate
$MgCl_2$	Magnesium chloride
MHz	Megahertz
min	Minute
m-MDH	Mitochondria Malic Dehydrogenase
mV	millivolt
MW	Molecular Weight
MSN	Mesoporous Silica Nanoparticle
nm	nanometer
N_2	Nitrogen
NaCl	Sodium Chloride
Na_2HCO_3	Sodium bicarbonate
NaOH	Sodium hydroxide
Na_2SO_4	Sodium sulfate
NH_4OH	Ammonium Hydroxide
NMR	Nuclear Magnetic Resonance
NP	Nanoparticle
OPA	O-phthaldialdehyde
OA	Oleic Acid
OA-BNP	Oleic Acid Boron Nanoparticles
PEG	Poly(ethylene glycol)
PEO-PPO-PEO	Poly(ethylene oxide)-poly(propylene oxide)-poly(ethylene oxide)
pH	Negative Logarithm of the Hydrogen Ion Concentration

*p*I	Isoelectric Point of a Protein
pK_a	Negative Logarithm of the Acid Dissociation Constant
rpm	revolution per minute
RT	Room Temperature
S	Surface Area
s, sec	Second
SBF	Simulated Blood Fluid
SEM	Scanning Electron Microscopy
Si	Silicon
SiNPs	Silica Nanoparticle
SiO_2	Silica
T	Temperature
TA	Tannic Acid
TA-TEOS	Tannic Acid templated mesoporous silica nanoparticles
TEM	Transmission Electron Microscopy
TEOS	Tetraethylorthosilicate
TGA	Thermogravimetric Analysis
THF	Tetrahydrofuran
TLC	Thin Layer Chromatography
TMB	1,3,5-Trimethylbenzene
UND	Undecylenic acid
UND-BNPs	Undecylenic acid-coated boron nanoparticles
UV/Vis	Ultraviolet/Visible

wt %	Weight Percent
XPS	X-ray Photoelectron Spectroscopy
XRD	X-ray Diffraction

LIST OF FIGURES

Figure Page

1.1. ^{10}B neutron capture event 6

1.2. Boronophenylalanine (BPA, left) and sodium borocaptate (BSH, right). 8

1.3. Stöber method using TEOS as the silica precursor 11

1.4. Mechanism for formation of mesoporous structure of MCM-41.[78] 14

2.1. Fluorescent tag attachment: OPA reacts with primary amine on the surface of BNPs. 35

2.2. The reaction between dopamine coated boron nanoparticles and PEG. 36

2.3. The molecule structures of dopamine, undecylenic acid and the scheme of ligand exchange on the BNPs. 38

2.4. DA-UND-B (left) suspended in water and UND- B (right) settled on the bottom of the vial in water 39

2.5. Representative TEM (left) and SEM (right) images of DA-BNPs. 40

2.6. Distribution of DA-UND-B according to DLS 41

2.7. XPS data for N 1s of DA-BNP particles 42

2.8. 1s XPS pattern of DA-BNP nanoparticles as a function of sputtering time. 43

2.9. TGA plots for UND-BNPs (dashed line) and DA-BNPs (solid line) under nitrogen. 45

2.10. ESI-MS spectra of aqueous solutions obtained from DA-BNPs under (upper) acidic and (lower) neutral conditions. 46

2.11. Fluorescence spectra for OPA (black), DA-BNPs (red), UND-BNPs (green), DA-BNPs treated with OPA (orange) and UND-BNPs treated with OPA (blue). 48

2.12. TGA plots of UND-BNPs, DA-BNPs and DA-PEG-BNPs 48

2.13. The molecular structure of vitamin C and oleic acid. 50

2.14. The TEM images for DA-OA-BNPs. 50

2.15. IR spectrum of DA-OA-BNPs. 51

2.16. The Reaction of DA-OA-B with dansyl chloride generated fluorescence under the UV light (left), the OA-B ethanolic solution with the addition of dansyl chloride. 52

3.1. a) Tannic acid molecular structure. b) TA 3D structure in different directions. 72

3.2. The picture of TA-EtOH-NH_4OH mixtures. The sample on the right is TA-EtOH without addition of NH_4OH. With increasing amount of NH_4OH added to the solution the mixture became milky than clear red. 73

3.3. SEM images of tannic acid template silica nanoparticles produce with different amount of tannic acid: a) TA4-TEOS; b) TA8-TEOS; c) TA16-TEOS; d) TA32-TEOS. 75

3.4. TEM images of tannic acid template silica nanoparticles produce with different amount of tannic acid: a) TA4-TEOS; b) TA8-TEOS; c) TA16-TEOS; d) TA32-TEOS. 76

3.5. a) Nitrogen adsorption–desorption isotherms and b) pore size distribution curves... 78

3.6. TEM images of tannic acid template silica nanoparticles produced in different reaction times: a) 2 h; b) 6 h; c) 24 h 79

3.7. TGA data of tannic acid template silica nanoparticles: a) produce by different reaction times; b) modified with amine groups. 81

3.8. Silicic acid released by TA-TEOS and Stöber SiNPs in water and SBF. 84

3.9. SEM images of TA-TEOS a) as made; b) in water (pH7) for a month; c) in SBF for a day; d) in SBF for a month. TEM images of TA-TEOS e) in milipore water for a month f) in SBF for a day. 85

3.10. Left vial contained TA-TEOS and right vial contained NH_2-TA-TEOS, both in the presence of dansyl chloride under the UV light. 87

3.11. Calibration curves of lysozyme, bovine hemoglobin, bovine serum albumin..... 90

3.12. Adsorption kinetics of TA-TEOS particles..... 93

3.13. Protein releasing kinetics of TA-TEOS and nonporous SiNPs. 94

3.14. The reversible conversion rection of oxaloacetate to L-Malate catalysed by m-MDH. 97

3.15. Catalysis activities of m-MDH immobilized in TA-TEOS and nonporous SiNPs and free m-MDH with the same concentration as the immobilized ones. 97

3.16. Catalysis activity of free m-MDH decreased in room temperature. 99

4.1. The synthesis of CME-APTES silsesquioxane. 108

4.2. The synthesis of ICPTES-EG silsesquioxane. 110

4.3. The synthesis of ICPTES-sorbitol silsesquioxane 111

4.4. Schematic illustration of bridged silsesquioxane with cleavable linker. 114

4.5. SEM images of CME-APTES-B-3-04-2h (CME-APTES SiNPs) 116

4.6. SEM (left) and TEM (right) images of CME-APTES-TEOS SiNPs 117

4.7. SEM images of CME-APTES SiNPs in a) ethanol b) HCl solution for 3 days and c) HCl solution for 10 days 119

4.8. TEM images of CME-APTES-TEOS SiNPs (a,b) in ethanol, (c,d) in acidic solution for 10 days. SEM images of e) CME-SiNPs in HCl solution for 1.5 months and f) CME-SiNPs in HCl solution for 2.5 months. 121

4.9. SEM images of a,b) ICPTES-EG-TEOS SiNPs c) ICPTES-EG-TEOS SiNPs in HCl solution for 1 week d) TEM image of ICPTES-EG-TEOS SiNPs. 122

4.10. SEM images of ICPTES-TEOS SiNPs synthesized with increasing ($a < b < c$) concentration of TEOS. 125

4.11. SEM images of a) ICPTES-sorbitol NPs and b)SiNPs produced in the same condition using TEOS as the only silica precursor. 126

4.12. TGA data of ICPTES-sorbitol SiNPs and TEOS SiNPs 127

4.13. Hydrolysis of ICPTES-sorbitol. 128

4.14. Dansyl chloride reacted with primary amines from the hydrolysis of the particles: (left to right) ICPTES-sorbitiol SiNPS in pH 2, pH 4, pH 8, pH 7, TEOS NPs in pH 7 aqueous solutions. 129

4.15. IR spectra of sorbitol, ICPTES, ICPTES-sorbitol SiNPs pH 4 supernatant and pH 2 supernatant. 131

4.16. SEM images of a) ICPTES-sorbitol-2 SiNPs b) ICPTES-sorbitol-2 SiNPs in HCl solution for 2 weeks c) TEOS SiNPs d) TEOS SiNPs in HCl solution for 2 weeks. 132

4.17. SEM images of ICPTES-sorbitol SiNPs a) in pH 4 solution for 1 days b) in pH 4 solution for 7 days c) in water for 1 days d) in water for 7 days. 133

4.18. The TEM images of ICPTES-Sorbitol SiNPs in a) Ethanol; b) aqueous solution for 2 days; c) aqueous solution for 7 days; d) aqueous solution for a month e) TEOS SiNPs in water for a month. 135

4.19. Sorption isothermals of ICPTES-sorbitol SiNPs before (red) and after (Blue) immersion in water for a week..... 136

4.20 Molybdenum blue tests result of ICPTES-sorbitol and TEOS SiNPs dissolution in milipore water. 138

4.21. SEM image of ICPTES-sorbitol SiNPs in aqueous solution for 3 months..... 138

LIST OF TABLES

Tables Page

1.1. Neutron capture cross-section values of multiple nuclides 5

2.1. Water suspension stability and zeta potential of DA-UND-B and DA-OA-B 50

3.1. The textural parameters of TA-TEOS from the N_2 sorption measurements 77

3.2. Zeta Potential of particles in water, phosphate buffer and KCl, phosphate buffer solution 89

3.3. Properties of the proteins selected in this study [52-55] 89

3.4. The Summary of protein adsorption by TA-TEOS and nonporous SiNPs 91

3.5 The m-MDH adsorption by TA-TEOS and nonporous SiNPs 95

4.1. Production conditions for CME-APTES SiNPs 116

4.2. DLS data of CME-APTES SiNPs 118

4.3. DLS data of CME –TEOS SiNPs 120

4.4. The reaction conditions of ICPTES-sorbitol SiNPs 125

4.5. Zeta potential of ICPTES-sorbitol NPs 128

4.6. The weight loss of ICPTES-sorbitol is acidic solutions 132

ACKNOWLEDGEMENTS

First, I would like to sincerely thank my advisor Dr. Ilya Zharov for his generous support and thoughtful guidance in science. He gave me the opportunity to challenge myself in various explorative and exiting projects, and to conduct research both in teamwork and independently. It is a great honor and pleasure for me to work with him and I enjoy every interesting conversation with him. Moreover, I am grateful to all the members of Zharov group for the valuable advice, patient help, and the pleasant lab environment. I am especially grateful to Nathan who worked with me on the boron nanoparticle project.

I am deeply thankful to my committee members who provide their insightful suggestions during each conversation. I also thank the faculties who generously allowed me to use their instruments and gave valuable comments about my research and the staff who kindly helped me.

I would also acknowledge Paulo Perez from the Anderson group who helped me with ball milling; Dr. Alexander Malugin from the Ghandehari group who helped me with the cell study; members from the Fang Group who helped me with the hydrogen storage experiment; and Fei Wu from the Minteer Group who helped me with enzyme activity tests.

Finally, I deeply thank my parents who continue providing the most precious love and support to me all the time. I love you more than I can express!

CHAPTER 1

INTRODUCTION

1.1 Aim and significance

Nanoparticles are defined as particles that possess sizes in the range from a few nanometers to a micrometer. Presently, preparation of inorganic and hybrid nanomaterials, such as carbon nanotubes,[1] quantum dots,[2] gold, [3] silver,[4] titanium oxide,[5] iron oxide[6] and silica nanoparticles (SiNPs)[7], is of great interest due to its applications for drug delivery,[1, 8] bioimaging,[7, 9] electrical and chemical sensors,[1, 10] photonic materials, [11] electronic device building blocks[1,12] and catalysis[13] over the past two decades. Advances in synthesis and fabrication enabled the production of countless new nanomaterials with various morphologies, and chemical and physical properties.

The advances in the development of new types of nanoparticles have led to the bloom of using these materials for diagnostic and therapeutic applications aimed at improving the treatment of diseases. Based on their small size, intrinsic chemical stability, multiple modification sites, and pharmacokinetic behaviors, nanoparticle systems offer alternatives in the fields of pharmaceuticals, drug delivery and bio-imaging for the treatment of various diseases.[14,15]

In the case of cancer treatment, the most universal therapeutic approaches are surgical resection, radio and chemotherapy. Recent advances in the cancer treatment have reduced the death rate; however, the number of people who suffer from cancer is still

increasing and many kinds of cancer are still considered incurable.[16] Although the government and private companies have invested a large amount of money, there has been no significant breakthrough in finding a cure to this fatal disease. Surgery is very efficient in removing the solid isolated tumors, but this traditional cancer therapy is restricted by the locations of the tumors and has uncertainty regarding the completeness of cancerous cell removal. High risk of removing tumors from the brain or other nerve- and blood vessel- intensive locations by surgery is widely recognized. Radiation and chemical therapy are affiliated treatments for the surgical resection that address the remaining cancer cells or are used as alternative treatments for early stage cancer. However, radiation and chemicals are detrimental to the patient's health, and some cancer cells become increasingly radio- and chemo-resistant.[17-19] From this perspective, it is essential to develop novel therapies that are not restricted by the tumor.

Nanoparticles with a size exceeding 7 nm are promising nanomedicine agents because they selectively accumulate in the tumor cells due to the Enhanced Permeability and Retention (EPR) effect, which was first described in 1986 by Maeda.[20] For the next decade, Maeda and his coworkers further studied this phenomenon and extensively analyzed the different factors that contributed to it.[21-23] Since the fast growth of a cancer cell requires more oxygen and other nutrition compared to normal cells, when the aggregates reach the size of 150-200 μm, they start developing their own blood supplies. [24] However, these neovasculatures are abnormal in their architecture and functions. Their lack of effective lymphatic drainage[25, 26] results in the uptake of nanoparticles without filtration. Another attractive nanoparticle biodistribution aspect is that they tend to accumulate at the site of inflammation because of the enhanced vascular

permeability, making them potential pharmaceutical and diagnostic agents for inflammatory diseases. [27] Moulari et al. reported that covalently bonding the inflammatory bowel disease drug 5ASA to the SiNPs increases the selectivity of its delivery to the inflamed intestinal tissue.[28]

SiNPs are considered potential drug carriers or bio-imaging agents, because of their tailored structure and active surface, and they are easy for chemical modification. However, the emergence of multiple biomedical applications of SiNPs is accompanied by recognition of the problem of bioaccumulation of the particles in multiple organs due to their low solubility in human serum. Considering their potential biomedical applications, it is required to address the shortcomings of the aforementioned nanomaterials systems via design and synthesis of a series of novel nanoparticles.

This dissertation is focused on synthesizing various new inorganic and hybrid nanoparticles and carefully exploring the attributes and properties of the particles. This study is beneficial as it describes new nanomaterials that have never been reported in literatures. The results provide information about rationally designing nanoparticles for biomedical applications. In addition, the particles can be used as prototypes inspiring the development of other new nanomaterials. In the long term, the novel nanoparticles can be used as bio-imaging agents or drug carriers.

In this chapter, we aim to provide background information for Boron Neutron Capture Therapy (BNCT), the synthesis and properties of nonporous and mesoporous SiNPs, and their potential biomedical applications. In subsequent chapters, we will describe in detail the experimental efforts in producing these particles and discuss the results and potential applications of the new materials.

1.2 Boron Neutron Capture Therapy

The second chapter describes the preparation of water-dispersible boron nanoparticles (BNPs) that have the potential application as boron delivery agents for Boron Neutron Capture Therapy (BNCT). Herein, the background and fundamental knowledge of BNTC and a brief overview on the approaches to discovery and synthesis of boron delivery agents will be discussed.

The limitations of current cancer treatments have spurred the development of alternative cancer therapies. Since the discovery of neutrons,[29] these newly discovered particles attracted much attention in the application to treat advanced, unresectable tumors, because of their highly penetrating properties and biological effectiveness.[30] However, neutrons are highly toxic for both tumors and healthy tissue, causing tissue necrosis. The objective to selectively destroy tumor cells while maintaining the normal tissues unaffected led to the development of neutron capture therapy.

Neutron capture therapy is a binary therapy relying on two components: neutron radiation and a neutron capture agent. Since Fermi first showed that neutrons were readily absorbed by lithium and boron,[29] more nuclides are found to be able to efficiently absorb neutrons (Table 1.1).[31] After capturing a neutron, the nuclide is promoted to an unstable, exited state from which it decays through fission into another nuclide and yields high linear energy transfer (LET).[32,33] Among all of the nuclides with high neutron capture cross-section, boron is thought to be of particular value for clinical uses. Unlike the radioactive ^{235}U [34,35] which is highly toxic; or the nonradioactive ^{6}Li which compounds easily and breaks down to lithium cations[36] [10]; B, commonly found in nature (20%, the other 80% is ^{11}B), possesses a large neutron capture cross-section, can

Table 1.1. Neutron capture cross-section values of multiple nuclides.

Element	Cross-section	Element	Cross-section
^{6}Li	942	^{149}Sm	42000
^{10}B	3838	^{151}Eu	5800
^{22}Na	32000	^{155}Gd	6100
^{58}Co	1900	^{157}Gd	255000
^{126}I	6000	^{235}U	580
^{135}Xe	2600000	^{142}Pu	1010

covalently bond with carbon, oxygen and nitrogen to form structures similar to organic molecules, and gives LET with effective path-length on the order of the dimension of a cell. Thus, ^{10}B is the focus of the majority of neutron capture therapy (BNCT) studies.[37]

BNCT is based on the nuclear reaction between ^{10}B and a thermal neutron source. When a ^{10}B atom captures a low energy (0.025 eV) thermal neutron, it becomes an unstable isotope ^{11}B, which undergoes fission into a recoiling ^{7}Li and an α particle, with a high linear energy transfer, which is sufficient to ionize tissue within an effective length of 5-9 μm (Figure 1.1).[38,39] The rationale for this therapy lies in the fact that both the low energy thermal neutron and boron-containing agents are harmless to human tissues until combined. Confining the neutron capture event within the cancer cell would cause damage to organelles, nucleus and cell membranes, and would effectively kill these cells while leaving the healthy cells unscathed—thus maximizing the treatment efficiency and reducing the undesirable side-effects.

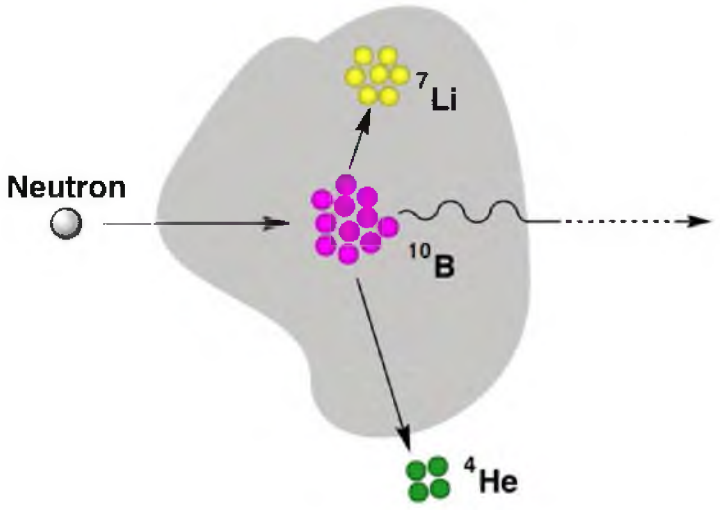

Figure 1.1. ^{10}B neutron capture event.

The studies of BNCT comprise two portion: The first one is the development of a nuclear reactor that is able to generate low energy thermal neutrons. The second one is the discovery of effective boron delivery agents.

The low energy neutrons obtained from the moderation of fast neutrons by heavy water or other media currently are limited to nuclear reactors. Nuclear reactors are difficult to manage and they usually cannot yield a sufficient flux of neutrons of the appropriate energy due to the fact that the neutrons generated from a nuclear reactor encompass diverse velocities. Early BNCT clinical trials failed partially because the nuclear reactors used were not proper for human treatment. Scientists are working on developing a clinically useful accelerator for BNCT to produce mono-energetic neutrons in the epithermal energy range (0.5-10 eV. These neutrons could penetrate deeper into the human body and reach the cancer cells without too much energy moderation by the tissues and still remain harmless to the patient's health.

So far, limited progress has been made in the area of developing efficient boron delivery agents. The major challenges in the development of these agents are low toxicity, high tumor/brain and tumor/ blood concentration ratios (>3-4:1), boron concentrations of (10^9 boron atoms/cell), water solubility and chemical stability. Many other elements in the body, such as hydrogen, nitrogen and oxygen, can capture neutrons. Although they have much smaller neutron capture cross-sections compared to boron, their sheer abundances in tissues make them a considerable obstacle in consuming neutrons and generating background radiations. Considering the probability of the occurrence of a neutron capture event, approximately 10^9 boron atoms per cell is required to assure a single neutron capture event will occur.[40,41] As a result, an effective boron delivery agent should have a high boron content to achieve this goal. Moreover, the boron delivery agents are required to be bio-compatible, and the accumulation ratio between cancer cells and blood are required to exceed 3:1.[42,43] If the accumulation of boron delivery agents in the blood stream were comparable to that in the cancer cells, the blood vessels or other healthy tissues would be harmed, leading to severe damage to the patient's health or even death.

Over the past 40 years, a variety of boron-containing agents have been synthesized, including boron porphyrins,[44,45] boron amino acids,[46] polyhedral boranes,[47] a boronated anti-epidermal growth factor receptor, [48] boronated nucleic acids and proteins,[49] DNA-binding agents[50,51] and monoclonal antibodies.[52] Boronophenylalanine (BPA) and sodium borocaptate (BSH) are the two most studied boron delivery agents that have been approved for clinical trials (Figure 1.2). [53, 54] BPA is an amino acid (phenylalanine, a cellular building block) derivative, hence it can be over-expressed by

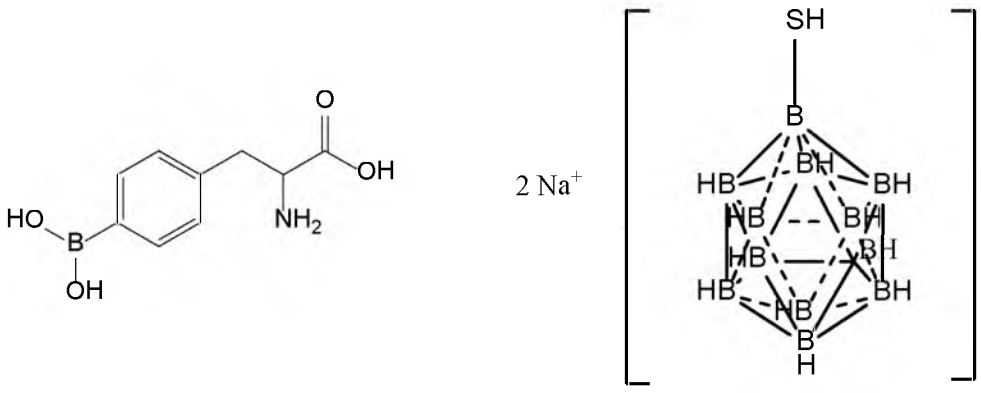

Figure 1.2. Boronophenylalanine (BPA, left) and sodium borocaptate (BSH, right).

the cancer cells whose fast growth requires a larger amount of constituents compared to the healthy cells.[55] Because of the high uptake by the cancer cells, BPA is currently one of the standard boron delivery agents. However, the low boron content is still an issue to overcome. BSH is one of the polyhedral boranes, generated from covalent bonding between boron atoms due to the unique electronic configuration of a boron valence shell. A single BSH molecule contains 10 boron atoms in a cage-like structure, which is considerably higher boron content compared to other boron containing compounds. It is proven that BSH can be uptaken by brain tumors, but the rationale behind this remains unclear.[56] In addition, the difficult synthesis of BSH derivatives hinders their further improvement.

Dendrimers are hyper-branched polymers, featured by the tree-like architecture with layers of repeat units. They hold much promise for drug delivery due to their ability to encapsulate guest molecules covalently and noncovalently. Yamamoto's group produced dendrimers carrying multiple polyhedral carboranes with high water-solubility to increase the loading amount of boron atoms,[57,58] but the difficult synthesis, expensive

cost and the demand of additional attachment of target ligands limited their applications. Other boron delivery agents were produced by the incorporation of boron-containing moieties into nucleic acids, antibodies or growth factors to achieve high selectivity. However, these methods either do not deliver enough boron atoms; or their high-boron payload results in major structural changes of the carriers, and hence affect their bio-activities and bio-functionalities.

Most of the boron delivery agents cannot deliver a sufficient number of boron atoms to cancer cells, suggesting the need to develop a new boron carrier that has high boron payload and amenable for easy modification with targeting ligands. Recently, boron-containing carbon[59] as well as boron nitride nanoparticles[60,61] have been reported as potential boron delivery agents with high boron content. Boron nanoparticles (BNPs) in the size range of 1-45 nm are synthesized by reduction of a tribromoboron salt using sodium naphthelinde. However, the particles yielded from this method are highly combustible and require further modification with a stabilizer to prevent them from reacting with oxygen in the air. We developed dopamine (DA) modified water-dispersible boron nanoparticles (BNPs) with high boron density (ca. 10^7 boron atoms per 50 nm particle) as a new boron delivery agent. Moreover, with active primary amines on the surface, the DA-BNPs are suitable for additional modification with targeting and imaging ligands.

1.3 Silica nanoparticles

Among inorganic particles for biomedical applications, silica nanoparticles (SiNPs) stand out due to their unique properties such as ease of synthesis, hydrophilic

surface, the availability of surface modification, mechanical properties, and their relatively low cytotoxicity.

1.3.1 Silica nanoparticle synthesis

Silica nanomaterials are usually produced by sol-gel chemistry[62] where silica precursors undergo a series of hydrolysis and condensation steps to form dimer, trimer and eventually particles or gels. The process of hydrolysis and condensation is catalyzed by either an acid or a base, which determines the morphology of the product and the required reaction time. The alkali conditions tend to produce solid particles while the acidic conditions yield gels or other soft networks of silica due to the difference in nucleation and particle growth under the different conditions.[63]

While there are a number of methods to produce SiNPs, one of the most studied and widely developed traditional synthesis methods is the Stöber method, which was reported in 1968 and involves the hydrolysis and condensation of tetraethoxysilane (TEOS) in a mixture of ethanol, water and ammonium hydroxide with rapid stirring (Figure 1.3).[64] The SiNPs produced by this method possess uniform spherical shape and narrow size distribution. The diameter of the SiNPs can be controlled in the range of 20 nm to 1 μm by altering the concentrations of ammonium hydroxide, TEOS and water due to the fact that ammonium hydroxide increases the solubility of silica intermediates leading to the formation of larger particles. Because of the simple procedure of particle preparation and the ease of controlling the particle size, the nonporous SiNPs were synthesized according to Stöber method in this dissertation.

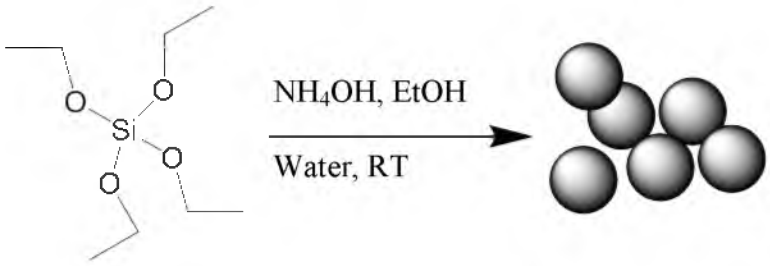

Figure 1.3. Stöber method using TEOS as the silica precursor.

1.3.2 Co-condensation for preparation of silica nanoparticles

Hybrid silica materials are typically produced by co-condensation, which usually involves alkali or acid catalyzed hydrolysis and condensation steps of multiple silanes. Most of the organosilanes with one or more organic branches cannot form SiNPs but result in loosely knit silica networks, due to reduced siloxane groups and steric effects of the organic branches. Thus, tetrasubstituted silanes such as TEOS are typically used in co-condensation reactions to assist in the formation of spheres. In addition, co-condensation with TEOS provides an alternative to produce surface-modified SiNPs. The co-condensation of TEOS with bridged silsequixaone bis(triethoxysiyl)ethane led to the formation of new SiNPs with enhanced mechanical and chemical stability.[65] Fluorescent tags and other functional moieties have been embedded into the SiNPs by co-condensation with TEOS.[66] By the encapsulation, the fluorescence tags are protected by the silica, which limits the interaction between the fluorescence dye and the environment, hence preventing the photo-bleaching and fluorescence molecule leakage. However, co-condensation still shows several disadvantages, such as low density of function groups on the surface of the particles.

1.3.3 Surface modification of silica nanoparticles

Owing to the abundance of silanol groups, the surface of SiNPs is easy to functionalize with a variety of moieties, ranging from small organic molecules to polymers, to inorganic coatings.[67] The modification of the SiNPs can not only offer functional groups but also alter the hydrophobicity, control the colloidal stability and other physical and chemical properties of the particles.

The surface modification of the SiNPs is usually accomplished through the addition of organosilane to the particle surface silanols by condensation. Moreover, polymer brushes can be grafted on the surface of the SiNPs by either directly attaching a pre-synthesized polymer on the particles, or by coupling the initiators on the surface of the particles then inducing the polymerization.[68-70]

1.4 Mesoporous silica nanoparticles

Mesoporous silica nanoparticles (MSNs), which combine the advantages of porous structure and versatile silica chemistry, have attracted much attention due to their various potential applications, including catalysis,[71] adsorption or separation medium,[72] and optical devices,[73] since the first mesoporous silica material, MCM-41 was discovered by the researchers from Mobil Oil Company in 1992.[74,75] Unlike nonporous SiNPs, the MSNs have the advantages of high surface area and porosity making them more attractive for guest molecule incorporation. During the past decade, numerous strategies were developed to produce a variety of mesoporous silica materials with diverse morphologies, pore sizes and pore arrangements.[76] Most of them were achieved by using surfactants as pore-forming agents, such as cetytrimethylammonium bromide (CTAB), triblock copolymer pluronic-123 ($PEO_{20}PPO_{70}PEO_{20}$).[77]

1.4.1 Mechanism of mesoporous silica materials formation

The formation of mesoporous silica is generally managed by the interactions between surfactant micelles and silica species such as electrostatic, hydrogen-bonding and Van der Waals interactions.[78,79] The geometry of the mesophase is known to be mainly determined by surfactant micelle morphology.[80] However, the mechanisms for cationic, anionic and non-ionic surfactants as pore-directing agents are different from each other.

The mechanism of cationic surfactant template MSNs was postulated by Beck *et al.*, where the silica-surfactant self-assembly occurs simultaneously with condensation of the silica precursors.[75] In the case of MCM-41, which was produced with cationic CTAB in alkaline condition, there are two possible mechanistic pathways. One suggested that when the surfactant concentration reaches the critical micelle concentration, the surfactant will self-assemble into micelles; and then the hydrophobic silica precursors will condensate on the polar side of the micelles and form into silica walls around the micelles (Figure 1.4). The other possible pathway suggests that supramolecular structure is formed with the mutual interactions between the silica species and surfactants by electrostatic interaction.

The mechanism of non-ionic triblock copolymer templated SBA-15 involves a combination of electrostatic and hydrogen-bonding interactions. Under the very strong acidic condition, the protonated silica species are positively charged and self-assemble with copolymers by electrostatic interaction. Moreover, the abundance of hydrogen bonding between the silica species and the hydrophilic blocks allows for the formation of silica walls around the supermolecular structure.

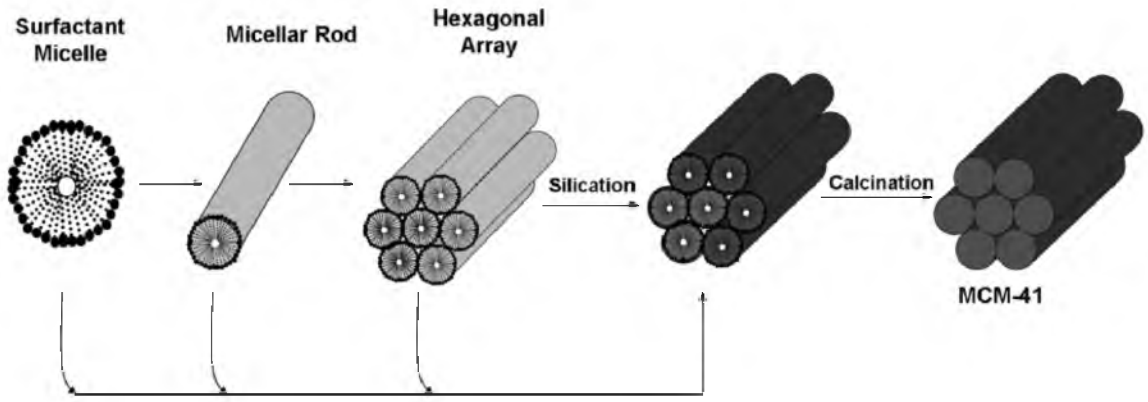

Figure 1.4. Mechanism for formation of mesoporous structure of MCM-41.[78]

1.4.2 Synthetic routes to mesoporous silica materials

Over the past decade, surfactant-templated synthetic methods for numerous mesoporous materials that possess different geometry, porosity and chemical compositions have been developed. The particle size and morphology can be controlled from sphere, to rod, to worm-like structures [81,82] by changing the molar ratio of silica precursors and surfactants, pH,[83,84] addition of co-solvents or organic swelling agents,[85] and introduction of organoalkoxysilane precursors during the co-condensation reaction.[86, 87] The diameter, morphology and arrangement of the pores are determined by the surfactant type and concentration, and reaction temperature.

The synthesis of first and most extensively studied mesoporous silica materials, MCM-41, was published by the scientists in Mobil Oil Company in 1992.[74,75] With the cationic surfactant of cetyltrimethylammonium bromide (CTAB) as liquid crystal template, tetraethyl orthosilicate (TEOS) or sodium metasilicate (Na_2SiO_3) as the silica precursor, and alkali as catalyst, MSNs with an ordered arrangement of parallel uniform two-dimensional (2D) hexagonal close-packed mesopores were synthesized and named

as MCM-41. The shape of the MCM-41 particles depends on the CTAB concentration, stirring rates and solution acidity. The aspect ratio can be tuned from 1-8 by increasing the CTAB concentration, and the particle size increases with ammonium concentration. The CTAB is removed by either calcination or solvent extraction (e.g. with HCl ethanol solution). Most of the MCM-41 materials were irregularly shaped. The Lin group made significant progress in controlling the MCM-41 shape while maintaining the highly porous structure by carefully manipulating the interaction between the CTAB and silica species.[88] The smallest MCM-41 nanoparticles were produced by the Mou group. They successfully prepared spherical MCM-41 naoparticles with a size down to 20 nm.[89]

SBA-15 is one of the most studied mesoporous silica materials due to the large tunable pore (7-50 nm) and good hydrothermal stability. The synthesis of SBA-15 is first reported by the Stucky group in 1998.[90] The hexagonal p6mm, two-dimensional channel structure was attained by utilizing nonionic triblock coplolymer as template to direct the organization of polymerizing silica species in a strong acidic condition (pH < 1) at the reaction temperatures between 35° and 80 °C. The silica species are positively charged under these conditions because the pH value is below the isoelectric point of silica (pH = 2), thus they undergo cooperative self-assembly with the triblock copolymers. The amphiphilic triblock copolymer used in SBA-15 synthesis is poly(alkylene oxide) triblock copolymers such as poly(ethylene oxide)-poly(propylene oxide)-poly(ethylene oxide) (PEO-PPO-PEO). The pore size and structure of SBA-15 can be adjusted by using poly(alkylene oxide) triblock copolymers with different mass and EO:PO block size ratios; by varying the reaction temperature and time; or by adding cosolvents such as 1,3,5-trimethylbenzene (TMB).

Compared to MCM-41 particles, SBA-15 has the advantages of large tunable pore size and thicker silica walls. Despite these advantages, molecular diffusion through the lengthy channel as well as the difficulty controlling the particle size of SBA-15 below 200 nm are the main concerns while preparing these materials for bio-medical applications.

1.4.3 Biomedical applications of mesoporous silica materials

Because of the large internal surface areas and ability to protect the sensitive cargos from the external environment, the MSNs are considered as ideal materials for pharmaceutical encapsulation, imaging and diagnostic labelling and other biomedical applications.[91] Silica walls not only reduce the interaction of the cargos with the environment but also provide surfaces for multiple modifications. The encapsulation of hydrophobic and toxic pharmaceuticals is another advantage of mesoporous silica materials.[92]

The encapsulation can be easily accomplished by immersing the MSNs into a solution of the guest molecules which enter the pores driven by diffusion, capillary forces and noncovalent interactions such as electrostatic interaction, hydrogen bonding and Van der Waals forces. For the MSNs modified with functional groups, the guest molecules are also able to be immobilized via covalent bonds. The pore opening size and pore morphology affect the efficiency and rate of encapsulation.

After the loading of the guest molecules, a cap or plug can seal the pore and the guest molecules are trapped within the particles until the removal of the caps. The caps can be designed to respond to external stimuli, such as acidity or temperature.[93,94] The variations in physical and chemical properties play an important role in determining the

compatibility of MSNs with biological systems.[95, 96] Recent studies show that the morphology of the nanoparticles influence their circulation half-life and other pharmacokinetic parameters.[97] The biocompatibility of MSNs with diameter of 150nm, 800nm and 4μm and pore sizes of 3 nm, 7 nm and 16nm has been examined in animal models. Slowing et al. reported the uptake of mesoporous silica nanoparticles by cervical cancer cells was improved by surface functionalization with cationic moieties.[98]

1.5 Degradation of silica nanoparticles

Silica-based nanomaterials have many potential bio-medical applications including drug delivery systems[99] and bio-imaging probes.[100] However, reports of long-term accumulation of silica nanomaterial in various organs with adverse health effects,[101, 102] question the potential bio-application of these materials.[103] Therefore the study of degradability of the silica materials in aqueous medium is critical.[104]

The solubility of silica in water is very low and the solubility is highly dependent on the temperature and pH. The bulk amorphous silica powder and micron-sized colloidal SiNPs show similar water solubility of approximately 0.01% due to the identical fundamental structure of amorphous silica in these materials.[105] It hydrolyzes in water to form monosilicic or polysilicic acid. Since the majority of the silicic acid degraded from silica is monosilicic acid, most of the degradation studies of the silica are based on the data of the monosilicic acid concentration. Monosilicic acid, unlike its polymeric form, is considered nontoxic (that does not show cell toxicity in up to 3 mM concentrations) and can transfer through the tissues, enter blood vessels and eventually be excreted with urine.[106]

The dissolution of silica depends on the equilibrium between the solid silica and monosilicic acid. Therefore, the low concentration promotes the degradation in order to reach the saturation of the monosilicic acid. It is known that the solubility of silica significantly increases under the basic conditions. One explanation suggested by Alexander et al.[105] is that the presence of $H_3SiO_4^-$ ions, which are produced from monosilicic acid under the basic solution, impels the further silica dissolution due to the continuous consuming of the monosilicic acids. However, the concentration of monosilicic acids is not affected by pH value.

$$Si(OH)_4 + OH^- = H_3SiO_4^- + H_2O$$

The rate at which SiNPs degrade depends on a number of factors including composition, surface area, pore structure and concentration of the silica particles. The surface area plays an important role in the degradation of silica. An increase in the surface area of nanoparticles leads to increased degradability of colloidal SiNPs because of the greater contact with water at the interfaces. The degradation rate of MSNs is higher than that of nonporous silica nanoparticles with the same diameters because of the presence of mesopores and thus larger surface area. Experiments also showed that smaller, nonporous SiNPs degrade faster than the larger, nonporous SiNPs; colloidal SiNPs degrade faster than the aggregates; and the MSNs with different diameter but same surface area show the same degree of dissolution due to the effect of surface area.[107]

The surface ligands also affect the degradation of the particles. The solvent-extracted, surfactant-templated MSNs dissolve faster compared to the calcinated MSNs due to the higher surface coverage with silano groups.[108] The modification of poly

ethylene glycols on the surface of the MSNs suppresses the degradability of the silica in SBF[109] and PBS.[110]

The nonporous SiNPs possess a mild degradation process. The degradation pathway includes initial surface bust erosion followed by a slow degradation of the bulk silica. The speed of silica degradation sharply declined after 2-7 days, then gradually approach zero.[104]

Yamada group reported that the MSNs partially retain the mesoporous structure, even at 70% degradation. They suggest that the degradation proceeds on the external and inner surfaces of particles heterogeneously due to different diffusion rates of water on the external surface and in the pores.[107] In addition, the pore structure also affects the degradation speed of the MSNs due to the different diffusion rates. For example, the MSNs with disordered 3D pore structure degrade slower than the MSNs with ordered 2D channels.[111]

Studies of the degradation of silica nanomaterials in simulated human serum are important for the applications of the materials. It is found that the metal ions in the solution affect the degradation behavior of silica.[112, 113] The degradation behavior of MCM-41 in SBF involves a fast degradation stage in the first several hours, and a decelerated degradation blocked by the formation of calcium and magnesium silicate layer.[108] The Sanchez group reported that the degradation of mesoporous silica films in PBS proceeds at high rate in the initial hours.[114] The degradation simultaneously proceeds from the external as well as the inner surfaces of MSNs, and the mesostructure and morphology are partly retained even after more than half of the MSNs are degraded.

Researchers also designed and synthesized novel SiNPs that are considered bio-degradable. Metal cations were doped into the silica networks to alter the composition of the silica shells.[115,116] Removing the cations from the silica structure by diffusion and chelation results in the destabilization of the structure. Bio-degradable polymers such as poly(L-lactic acid)[117] were incorporated into the silica matrix. Hydrolysis of the polymers led to the degradation of the silica material. Our approach to silica biodegradability is entirely different; our approach uses organosilane precursors with electron-withdrawing groups to destabilize the silica structure, as described in Chapter 4.

1.6 Thesis overview

This thesis will focus on the design and preparation of novel inorganic and organic/inorganic hybrid nanoparticles. The motivation and significance of these studies will be explained, and the potential applications of the new materials will be discussed. The first project deals with producing bio-compatible boron nanoparticles for Boron Neutron Capture Therapy (BNCT). In an effort to achieve biocompatibility, the hydrophobic boron nanoparticles obtained from ball milling underwent a ligand exchange process to replace the surface ligands with dopamine, to impart good water-dispersibility while also providing active amine groups for further functionalization of the particles with imaging or targeting ligands. In the other projects, silica nanoparticles (SiNPs) with novel structures were designed and synthesized. The synthesis of large-pore mesoporous SiNPs using tannic acid (TA) as a pore-directing template, and their application to immobilize proteins, were described in the third chapter. To achieve degradable silica nanoparticles, a silsesquioxane with a cleavable bridge was synthesized. Co-condensation

of tetraethoxysilane (TEOS) with the bridged silsesquioxane provided interesting SiNPs, which degrade into mesoporous structures in water and the simulated blood fluid.

1.7 References

[1] a) Rao, C. N. R.; Govindaraj, A. *Adv. Mater.* **2009**, *21*, 4208-4233. b) Eder, D. *Chem. Rev.* **2010**, *110*, 1348–1385.

[2] Zrazhevakiy, P.; sena, M.; Gao, X. *Chem. Soc. Rev.* **2010**, *39*, 4326-4354.

[3] Lu, L.; Randjelovic, I.; Capek, R.; Gaponik, N.; Yang, J.; Zhang, H.; Eychmüller, A. *Chem. Mater.* **2005**, *17*, 5731-5736.

[4] Sweet, M. J.; Singleton, I. *Advances in Applied Microbiology* **2011**, *77*, 115-133.

[5] Macwan, D. P.; Dave, P. N.; Chaturvedi, S. *J. Mater. Sci.* **2011**, *46*, 3669-3686.

[6] Halbreich, A.; Roger, J.; Pons, J. N.; Geldwerth, D.; Da Silva, M. F.; Roudier, M.; Bacri, J. C. *Biochim.* **1998**, *80*, 379-390.

[7] Bae, S. W.; Tan, W.; Hong, J. -I. *Chem. Commun.* **2012,** *48*, 2270-2282.

[8] Liu, Z.; Fan, A. C.; Rakhra, K.; Sherlock, S. *Angew Chem Int Ed Engl* **2009**, *48*, 7668-7672.

[9] Yezhelyev, M. V.; Qi, L.; O'Regan, R. M.; Nie, S.; Gao, X. *J. Am. Chem. Soc.* **2008**, *130*, 9006-9012.

[10] a) Lee, K.; Asher, S. A. *J. Am. Chem. Soc.* **2000**, *122*, 9534-9537. b) Wuelfing, W. P.; Murray, R. W. *J. Phys. Chem. B* **2002**, *106*, 3139-3145. c) Krasteva, N.; Besnard, I.; Guse, B.; Bauer, R. E.; Mullen, K.; Yasuda, A.; Vossmeyer, T. *Nano Lett.* **2002**, *2*, 551-555.

[11] a) Maldovan, M.; Thomas, E. L. *Nat. Mater.* **2004**, *3*, 593-600. b) Fudouzi, H.; Xia, Y. N. *Langmuir* **2003**, *19*, 9653-9660.

[12] Klein, D. L.; McEuen, P. L.; Katari, J. E. B.; Roth, R.; Alivisatos, A. P. *Appl. Phys. Lett.* **1996**, *68*, 2574-2576.

[13] Pietron, J. J.; Stroud, R. M.; Rolison, D. R. *Nano Lett.* **2002**, *2*, 545-549.

[14] Sahane, S. P.; Nikhar, A. K.; Bhaskaran, S.; Mundhada, D. R.*International Journal of Pharmacy and Technology* **2012**, *4*, 2085-2099.

[15] McNeil, S. E. *Wiley Interdiscip. Rev. Nanomed. Nanobiotechnol* **2009**, *1*, 264-271.

[16] National Cancer Institute: 2012 Report to the Nation on the Status of Cancer http://www.cancer.gov/newscenter/newsfromnci/2012/ReportNationRelease2012

[17] Gasper L.E., Fisher B.J., Macdonald D.R., et al., *int. j. radiat. Oncol. Biol. Phys.* **1992**, *24*, 55-57.

[18] Wallner K.E., Galicich J.H., Krol G., Arbit E., Malkin M.G. *J. Radiat. Oncol. Biol. Phys.* **1989**, *16*, 1405-1409.

[19] Oppitz U., Maessen D., Zunterer H., Richter S., Flentje M. *Radiother. Oncol.* **1999**, *53*, 53-57.

[20] Matsumura, Y.; Maeda, H. *Cancer Research* **1986**, *46*, 6387-6392.

[21] Fang, J.; Nakamura, H.; Maeda H. *Adv. Drug Deliv. Rev.* **2011**, *63*, 136-151.

[22] Maeda, H. *J. Cont. Release* **2010**, *142*, 296-298.

[23] Maeda, H. *Bioconj. Chem.* **2010**, *21*, 797-802.

[24] Folkman, J. *J. Natl. Cancer Inst.* **1990**, *82*, 4-6.

[25] Pepper, M.S. *Clin. Cancer Res.* **2001**, *7*, 462-468.

[26] Padera, T. P.; Kadambi, A.; di Tomaso, E.; Carreira, Carla M.; Brown, E. B.; Boucher, Y.; Choi, N. C.; Mathisen, D.; Wain, J.; Mark, E.; J. Munn, L. L.; Jain, R. K. *Science*, **2002**, *296*, 1883-1886.

[27] Morishige, T.; Yoshioka, Y.; Inakura, H.; Tanabe, A.; Yao, X.; Narimatsu, S.; Monobe, Y.; Imazawa, T.; Tsunoda, S.; Tsutsumi, Y. *Biomaterials*, **2010**, *31*, 6833-6842.

[28] Moulari, B,; Pertui, D.; Pellequer, Y.; Lamprecht, A. *Biomaterials* **2008**, *29*,4554-4560.

[29] Fermi E. Artificial radioactivity produced by neutron bombardment. In: Holberg MA, ed. Les prix Nobel in **1939**. Stockholm: Norstedt and Soner, **1939**.

[30] Friedlander, G.; Kennedy, J. W.; Macias, E. S.; Miller, J. M. In Nuclear and Radiochemistry, 3rd ed.; John Wiley & Sons: New York, **1981**.

[31] Locher, G. L. *Am. J. Roentgenol.* **1963**, *36*, 632-636.

[32] Barth R.F., Soloway A.H., Fairchild R.G.. Boron neutron capture therapy for cancer. *Sci Am* **1990**,*263*, 100-103.

[33] Soloway, A. H.; Tjarks, W.; Barnum, B. A.; Rong, F. G.; Barth, R.F.; Codogni, I. M.; Wilson, J. G. *Chem. Rev.* **1998**, *98*, 1515-1562.

[34] Knock, F. E. *Surg. Gynecol. Obstet.* **1959**, *109*, 445-449.

[35] Bases, R. E. *Science* **1957**, *126*, 164-165.

[36] Zahl, P. A.; Cooper, F.S. *Radiology* **1941**.*37*, 673-682.

[37] Locher, G.L. *Am. J. Roentgenol. Radium Therapy* **1936,** *36,* 1-13.

[38] Sweet, W. H.; Javid, M. *Trans. Am. Neurol. Assoc.* **1951**, *76*, 60-63.

[39] Krüger, P. G, *Proc. Natl. Acad. Sci. U. S. A.* **1940**, *26*, 181-192.

[40] Tolpin, E. I.; Wellum, G. R.; Dohan, F. C.; Kornblith, P. L.; Zamenhorf, R. G. *Oncology* **1975** *32*, 223-246.

[41] Javid, M.; Brownell, G. R.; Sweet, W. H. *J. Clin. Invest.* **1952**, *31*, 604-610.

[42] Valliant, J. F.; Guenther, K. J.; King, A. S.;Morel, R.; Schaffer, P.; Sogbein, O. O.: Stephenson, K. A. *Coord. Chem. Rev.,* **2002**, *232*, 173-230.

[43] Nigg, D. W. *J Neurooncol.*, **2003**, *62*, 75-86.

[44] Isaac, M. F.; Khal, S. B. *J. Organomet. Chem.,* **2003**, *680,* 232-243.

[45] Ceberg, C. P.; Brun, A.; Kahl, S. B.; Koo, M. S.; Persson B. R.; Salford, L. G. *J. Neurosurg.*, **1995**, *83*, 86-92.

[46] Lin, Y. C.; Hwang, J.-J.; Wang, S.-J.; Yang, B.-H.; Chang, C.-W.; Hsiao, M.-C.; Chou, F.-I. *Anticancer Res.* **2012**, *32*, 2657-2664.

[47] Diaz, A.; Stelzer, K.; Laramore, G.; Wiersema,R. *Research and Development in Neutron Capture Therapy*; Monduzzi Editore: Bologna, **2002**, 993-999.

[48] Yang, W.; Wu, G.: Barth, R. F.: Swindall, M. R.; Bandyopadhyaya, A. K.; Tjarks, W.; Tordoff, K.; Moeschberger, M.; Sferra, T. J.: Binns, P. J.; Riley, K. J.; Ciesielski, M. J.; Fenstermaker, R. A.; Wikstrand, C. J. *Cancer Res.,* **2008**, *14,* 883-891.

[49] Wyzlic, I. M.; Tjarks, W.; Soloway, A. H.; Anisuzzaman, A. K. M.; Rong, F.-G.; Barth, R. F. *Int. J. Radiat. Oncol. Biol. Phys.***1994**, *28*, 1203-1213.

[50] Tietze, L. F.; Griesbach, U.; Bothe, U.; Nakamura, H.; Yamamoto, Y. *Chembiochem,* **2002**, *3*, 219-225.

[51] Woodhouse, S. L.; Rendina, L. M. *Chem. Commun.*, **2001,** 2464-2465.

[52] Nakamura, H.; Miyajima, Y.; Takei, T.; Kasaoka, S.; Maruyama, K. *Chem. Commun.,* **2004**, 1910-1911.

[53] Hatanaka, H. A. *J. Neurol.,* 1975, **209**, 81-94.

[54] Mishima, Y.; Ichihashi, M.; Tsui, M.; Hatta, S.; Ueda, M.; Honda, C.; Susuki, T. *Lancet*, **1989**, *2*, 388-389.

[55] Soloway, A. H.; Tjarks, W.; Barnum, B. A.; Rong, F. G.; Barth, R. F.; Codogni, I. M.; Wilson, G. J. *Chem. Rev.***1998**, *98*, 1515-1562.

[56] Soloway, A. H.;Hatanaka, H.; Davis, M. A. *J. Med. Chem.* **1967**, *10*, 714-717.

[57] Nemoto, H.; Wilson, J.G.; Nakamura, H.; Yamamoto,Y. *J. Org. Chem.* **1992**, *57*, 435-435.

[58] Nemoto, H.; Cai, J. P..; Yamamoto,Y *Chem. Commun.* **1994**, 577-578.

[59] Hwang, K. C.; Lai, P. D.; Chiang, C. S.; Wang P. J.; Yuan, C. Y. *Biomaterials,* **2010**, *31*, 8419-8425.

[60] Mortensen, M. W.; Sorensen, P. G.; Bjorkdahl, O.; Jensen, M. R.; Gundersen H . J. G.; Bjornholm, T. *Appl. Radiat. Isot.,* **2006**, *64*, 315-324.

[61] Petersen, M. S.; Petersen, C. C. ; Agger, R.; Sutmuller, M.; Jensen, M. R.; Soerensen, P. G.; Mortensen, M. W.; Hansen, T.; Bjoerholm, T.; Gundersen, H. J.; Huiskamp R.; Hokland, M. *Anticancer Res.,* **2008**, *28*, 571-576.

[62] Brinker, C. J.; Scherer, G. W. *Sol-Gel Science* **1990** Academic Press, NY.

[63] Coenen, S; De Kruif, C. J. *J. Collid. Interface Sci.* **1988**, *124*, 104-110.

[64] Stober, W.; Fink, A.; Bahn, E. *J. Collid. Interface Sci.* **1968**, *26*, 62-69.

[65] Wyndham, K. D.; O'Gara, J. E.; Walter, T. H.; Glose, K. H.; Lawrence, N. L.; Alden, B. A.; Izzo, G. S.; Hudalla, C. J.; Iraneta, P. C. *Anal. Chem.* **2003**, *75*, 6781-6788.

[66] Burns, A.; Hooisweng, O.; Wiesner, U. *Chem. Soc. Rev.* **2006**, *35*, 1028-1042.

[67] Trewyn, B. G.; Giri, S.; Slowing, I. I.; Lin, V. S.-Y. *Chem. Commun.* **2007**, 3236-3245.

[68] Radhakrishnan, B.; Ranjan, R.; Brittain, W. J. *Soft Matter* **2006**, *2*, 386-396.

[69] Schepelina, Olga; Poth, Nils; Zharov, Ilya *Adv. Funct. Mater.* ***2010,*** *20*, 1962-1969.

[70] Smith, Joanna J.; Zharov, Ilya *Chem. Mater.* **2009**, *21*, 2013-2019.

[71] Clark, J. H.; Macquarrie, D. J. *Chem. Commun.* **1998**, 853-860.

[72] (a)Lu, S; Song, Z.; He. J *J. Phys. Chem. B* **2011**, *115*, 7744-7750. (b) Sang, L; Vinu, A.;Coppens, M. *Langmuir* **2011**, *27*, 13828-13837. (c) Lin Y.; Abadeer, N.; Hurly, K. R.; Haynes, C. L. *J. Am. Chem. Soc.* **2011**, *133*, 20444-20457.

[73] Davis M.E. *Nature* **2002**, *417*, 813-821.

[74] Kresge, C. T.; Leonowicz, M. E.; Roth, W. J.; Vartuli, J. C.; Beck, J. S. *Nature* **1992**, *359*, 710-712.

[75] Beck, J. S.; Vartuli, J. C.; Roth, W. J.; Leonowicz, M. E.; Kresge, C. T.; Schmitt, K. D.; Chu, C. T. W.; Olson, D. H.; Sheppard, E. W.; McCullen, S. B.; Higgins, J. B.; Schlenker J. Am. Chem. Soc. **1992**, *114*, 10834-10843.

[76] a) Tang F.; Li, L.; Chen, D. *Adv. Mater.* **2012**, *24*, 1504-1534. b) Asefa, T.; Tao, Z. *Chem. Res. Toxicol.* Articles ASAP

[77] Zhao,D; Feng, J.; Huo, Q.; Melosh, N.; Fredrickson, G. H.; Chmelka, B.F.; Stucky, G. D. *Science* **1998**, *279*, 548-552.

[78] Sayari, A. *Chem. Mater.* **1996**, *8*, 1840-1852.

[79] Huo, Q.; Leon, R.; Petroff, P. M.; Stucky, G. D. *Science* **1995**, *268*, 1324-1327.

[80] Wan, Y.; Zhao, D. Y. *Chem. Rev.* **2007**, *107*, 2821-2860.

[81] Bagshaw, S. A.; Prouzet, E. ; Pinnavaia, T. J. *Science* **1995**, *269*, 1242-1244.

[82] Prouzet, E.; Pinnavaia, T. J. *Angew. Chem. Int. Ed. Engl.* **1997**, *36*, 516-518.

[83] Lin, H. P.; Mou, C. Y. *Acc. Chem. Research* **2002**, *35*, 927-935.

[84] Cai, Q.; Luo, Z. S.; Pang, W. Q.; Fan, Y. W.; Chen, X. H. ; Cui, F. Z. *Chem. Mater.* **2001**, *13*, 258-263.

[85] Anderson, M. T.; Martin, J. E.; Odine, J. G.; Newcomer, P. P. *Chem. Mater.* **1998**, *10*, 1490-1500.

[86] Huh, S.; Wiench, J. W.; Yoo, J. C.; Pruski, M.; Lin, V. S. Y. *Chem. Mater.* **2003**, *15*, 4247-4256.

[87] Huh, S.; Wiench, J. W.; Trewyn, B. G.; Song, S.; Prusk, M.; Lin, V. S. Y. *Chem. Commun.* **2003**, 2364-2365 .

[88] Lai, C. Y.; Trewyn. B. G.; Jeftinijia, D. M.; Jeftinnija, K.; Xu, S.; Jeftinnija, S. Lin, V. S. –Y *J. Am. Chem. Soc.* **2003**, *125*, 4451-4459.

[89] Lu, F.; Wu, S.; Hung, Y.; Mou, C. *Small*, **2009**, *5*, 1408-1413.

[90] Zhao, D.; Feng, J.; Huo, Q.; Melosh, N.; Fredrickson, G. H.; Chmelka, B. F.; Stucky, G. D. *Science* **1998**, *179*, 548-552.

[91] Agasti, S. S.; Rana, S.; Park, M. H.; Kim, C. K.; You, C. C.; Rotello, V. M. *Adv Drug Deliv Rev* **2010**, *62*, 316–328.

[92] Patil, A.; Chirmade, U. N.; Slipper, I.; Lamprou, D. A.; Urquhart, A.; Douroumis, D. *J. Nanomedic. Nanotechnol.* **2011**, *2*, 1000111.

[93] Lee, J. E.; Lee, D. J.; Lee, N.; Kim, B. H.; Choi, S. H.; Hyeon, T. *J. Mater. Chem.* **2011**, *21*, 16869-16872.

[94] Croissant, J.; Zink, J. I. *J. Am. Chem. Soc.* **2012**, *134*, 7628-7631.

[95] Li, M.; Al-Jamal, K. T.; Kostarelos, K.; Reineke, J. *ACS Nano* **2010**, *4*, 6303-6317.

[96] Krug, H. F.; Wick, P. *Angew Chem Int Ed Engl* **2011**, *50*, 1260-1278.

[97] Hudson, S. P.; Padera, R. F.; Langer, R.; Kohane, D. S. *Biomaterials* **2008**, *29*, 1657-1668.

[98] Slowing, I; Trewyn, B. G.; Lin, V. S.-Y. *J. Am. Chem. Soc.* **2006**, *128*, 14792-14792.

[99] a) Ferrari M. *Nat Rev Cancer* **2005**, *5*, 161-171. b) Martin CR, Kohli P. *Nat Rev Drug Discov* **2003**, *2*, 29-37. c) Alivisatos P. *Nat Biotechnol* **2004**, *22*, 47-52.

[100] Taylor-Pashow, K. M. L.; Rocca, J. D.; Lin, W. *Nanomaterials* **2012**, *2*, 1-14.

[101] Radin, S.; El-Bassyouni, G.; Vresilovic, E. J.; Schepersc, E.; Ducheyne, P. *Biomaterials* **2005**, *26*, 1043-1052.

[102] Lin, W.-C.; Chiang, C.-W.; Hong, C.-Y.; Chen, P.-J.; Wu, K. C.- W. *Chem. Lett.* **2011**, *40*, 533-535.

[103] (a) Langer, R. *Nature* **1998**, *392*, 5-10. (b) Lendlein, A.; Langer, R. *Science* **2002**, *296*, 1673-1676. (c) Radin, S.; E.-Bassyouni, G.; Vresilovic, E. J.; Schepers, E.; Ducheyne, P. *Biomaterials* **2005**, *26*,1043-1052. (d) Nair, L. S.; Laurencin, C. T. *Prog. Polym. Sci.* **2007**, *32*, 762-798.

[104] (a) Roelofs, F.; Vogelsberger, W. *J. Phys. Chem. B* **2004**, *108*, 11308-11316. (b) Miyata, K.; Gouda, N.; Takemoto, H.; Oba, M.; Lee, Y.; Koyama, H.; Yamasaki, Y.; Itaka, K.; Nishiyama, N.; Kataoka, K. *Biomaterials* **2010**, *31*, 4764-4770.

[105] Alexander, G. B.; Heston, W. M.; Iler, R. K. *J. Phy. Chem.* **1954**, *58*,453-455.

[106] Popplewell, J. F.; King, S. J.; Day, J. P.; Ackrill, P.; Fifield, L. K.; Cresswell, R. G. *J Inorg Biochem* **1998**, *69*, 177-180.

[107] Yamada, H.; Urata, C.; Aoyama, Y.; Osada, S.; Yamauchi, Y.; Kuroda, K. *Chem. Mater.* **2012**, *24*, 1462-1471.

[108] He, Q.; Shi, J.; Zhu, M.; Chen, Y.; Chen. F *Micropor. Mesopor, Mater.* **2010**, *131*, 314-320.

[109] Cauda, V.; Argyo, C.; Bein, T. J. *Mater. Chem.* **2010**, *20*, 8693-8699.

[110] Lin, Y.-S.; Abadeer, N.; Haynes, C. L. *Chem. Commun.* **2011**, *47*, 532-534.

[111] Chen, K.; Zhang, J.; Gu, H. *J. Mater. Chem.*, **2012**, *22*, 22005–22012.

[112] Li, X.; Zhang, L.; Dong, X.; Liang, J; Shi, J. *Micropor. Mesopor. Mater.* **2007**, *102*, 151-157.

[113] Cauda, V.; Schlossbauer, A.; Bein, T. *Micropor. Mesopor. Mater.* **2010**, *132*, 60-71.

[114] Bass, J. D.; Grosso, D.; Boissiere, C.; Belamie, E.; Coradin, T.; Sznchez, C. *Chem. Mater.* **2007**, *19*, 4349-4356.

[115] Li, X.; Zhang, L.; Dong, X.; Liang, J.; Shi, J. *Microporous Mesoporous Mater.* **2007**, *102*, 151-158.

[116] Mitchell, K. K. P.; Liberman, Alexander; Kummel, A. C.; Trogler, W. C. *J. Am. Chem. Soc.* **2012**, *134*, 13997-14003.

[117] Avnir, D.; Zalzberg, L. *J. Sol-Gel. Sci. Technol.* **2008**, *48*, 47-50.

CHAPTER 2

BIO-COMPATIBLE BORON NANOPARTICLES

2.1 Introduction

Boron neutron capture therapy (BNCT) of cancer is based on the nuclear reaction between ^{10}B and slow neutrons, first forming an unstable isotope, ^{11}B, which undergoes fission into high linear energy transfer (LET) ^{7}Li nuclei and alpha particles. Low energy (0.025 eV) neutrons are sufficient to initiate the neutron capture reaction; this energy is below the threshold of the energy that causes damages to the tissue components. The energy generated from the neutron capture reaction is several times higher than the energy of the initial neutron beam, and can eradicate tumor cells. Moreover, because the high LET particles have limited biologically-effective path lengths in tissue (5-9 μm),[1] the destructive effects of these high-energy particles are limited to or near boron-containing cells.

The major challenges in the development of boron delivery agents are achieving high boron concentrations of 10^9 ^{10}B/cell, high tumor/brain and tumor/blood concentration ratios (>3-4:1),[2-4] low toxicity, [5] water solubility and chemical stability.[6] Over the past 40 years, a variety of boron-containing agents have been designed and synthesized, including boron porphyrins, [7,8] boron amino acids, [9] polyhedral boranes, [10] a boronated anti-epidermal growth factor receptor, [11] DNA-binding agents [12, 13] and monoclonal antibodies. [14] Among those, boronophenylalanine (BPA) and sodium

borocaptate (BSH) are the only two boron delivery agents that have been used clinically. [15,16] However, most of the boron delivery agents cannot deliver a sufficient number of boron atoms to the cancer cells. Recently, boron-containing carbon [17] and silver nanoparticles, [18] as well as boron nitride nanoparticles [19,20] have been reported as potential boron delivery agents with high boron content. In this respect, pure boron nanoparticles (BNPs) should be superior boron delivery agents with even higher boron density (ca. 10^7 boron atoms per 50 nm particle), compared to other boron delivery agents. [21]

The goal of this research project is to produce new boron delivery agents. Recently, a practical surfactant-assisted ball milling method to produce air-stable BNPs on a large scale was reported. [22,23] However, these particles are hydrophobic due to the surface fatty acid molecules, and are not suitable for biomedical applications. This chapter describes the preparation of water dispersible BNPs with surface amine functionality by exchanging the surface fatty acid ligands with dopamines (DA). Characterization of these nanoparticles was performed by transmission electron microscopy (TEM), X-ray photoelectron spectroscopy (XPS), thermogravimetric analysis (TGA), mass spectrometry, and fluorescence spectroscopy. The resulting BNPs were functionalized with fluorescence tags and poly ethylene glycol (PEG). The study also includes the exploration of the chemical modification of the amine-modified particles and initial biocompatibility studies, as well as the cellular uptake of the DA-BNPs performed on cultured murine macrophage cells.

2.2 Experimental section

2.2.1 Chemicals and instruments

Elemental boron powder (Sigma-Aldrich), Undecylenic acid (UND acid, Sigma-Aldrich), Dopamine hydrochloride (Sigma-Aldrich), anhydrous sodium carbonate (Sigma-Aldrich), O-phthaldialdehyde (OPA, Sigma-Aldrich), β-mercaptoethanol (BME, Sigma-Aldrich), oleic acid (OA, Sigma-Aldrich), L-ascorbic acid (Vitamin C, Sigma-Aldrich), dansyl chloride (Sigma-Aldrich), fluorescein isothiocyanate (FITC, Sigma-Aldrich), Rhodamine B isothiocyanate (Sigma-Aldrich) were purchased from commercial suppliers and used without further purification. N,N-dimethylformamide (DMF, Mallinckrodt) was dried by anhydrous magnesium sulfate. Hexane (technical grade, Sigma-Aldrich), chloroform (reagent grade, MACRON), methanol (ACS Reagent, Fisher Scientific) and ethanol (200 proof, ACS-grade, Pharmaco-Aaper) were used as solvents without further purification. Millipore water (18 MΩ • cm) used in all experiments was obtained from a Barnstead "E-pure" water purification system.

The ball-milling was done in a Spex-CertiPrep 8000M mixer using a tungsten carbide jar and tungsten milling balls. The transmission electron microscopy (TEM) images were recorded with a FEI Philips Techna T-12 microscope operating at 120 kV. Scanning electron microscopy (SEM, FEI Nova Nano 600, Hillsboro, OR), dynamic light scattering (DLS, A Particle Sizing Systems NICOMP 380, Santa Barbara, CA),were used to analyze the morphology and size distribution of BNPs. Zeta-potential measurements were carried out in water using a NICOMP 380 ZLS Zeta Potential/Particle Sizer (PSS • NICOMP Particle Sizing Systems). Fluorescence spectra were recorded using a RF-1501 Spectrofluorophotometer (SHIMADZU). FT-IR spectrometer (Thermo

Scientific Nicolet 8700 model) was used for surface functional group detection. The sample particles were suspended in solutions then several drops were added to the sample window and dried in the air. The spectra were recorded from 400 to 4000 cm^{-1}. Thermogravimetric analysis (TA Instruments TGA 2050 or TA Instruments TGA 2950) was performed either in nitrogen or argon atmosphere. About 10 mg of the sample was measured on an open platinum pan by TGA. X-Ray photoelectron spectroscopy (XPS, Kratos Axis Ultra instrument, Chestnut Ridge, NY), and Mass spectrometry (Waters ESI-TQD) were employed to analyze the surface of the BNPs. A Branson 1510 sonicator was used for all sonications. A Clay Adams Compact II Centrifuge (3200 rpm, Becton Dickinson) and ultracentrifuge Sorvall RC5B Plus (15000 rpm on a SA-600 rotor) were used for all centrifugations.

2.2.2 Preparation of air-stable boron nanoparticles

Micro-scale elemental boron powder (2 g) was grinded in a Spex-CertiPrep 8000M mixer mill with tungsten carbide or stainless steel balls in a tungsten carbide milling jar at an 80:1 charge ratio (ball to powder ratio). To protect boron surfaces from oxidation, 1 mL of undecylenic acid or oleic acid was added to the boron powder in 15 mL of hexane prior to milling. Since the ratio of the solvent and surfactants are crucial in optimizing the milling process,[24, 25] the above milling condition was optimized after several trials. During the first 6 h of grinding time, the boron powder was broken down rapidly. After 6 h, the diameters of the BNPs seemed to reach a minimum limit of 30 nm. Samples milled for 7 to 11 h did not show a significant size discrepancy. Thus, all nanoparticles used in this work were prepared by 7 h of milling. The resulting undecylenic acid-coated boron nanoparticles (UND-BNPs) and oleic acid coated BNPs

(OA-BNPs) were washed by methanol to remove excess fatty acid and redispersed in hexane. SEM, DLS and TEM were used to analyze morphology and size distribution of BNPs.

2.2.3 Ligand exchange reaction

The ligand exchange reaction of fatty acids by rigid diol molecules on the BNPs was proven to be a versatile method. In this chapter, we produced DA-UND-B, DA-OA-B and ascorbic acid-UND-B by the same procedure. A typical ligand exchange reaction is described below. Dopamine hydrochloride was used to substitute the fatty acids on the surface of boron nanoparticles.[26] The ligand exchange reaction took place in a 2:1 mixture of chloroform and N,N-dimethylformamide (DMF) with approximately 10 mg of anhydrous sodium carbonate and 8 mg of dopamine hydrochloride. The solution was stirred for a few minutes to homogenize. After mixing the solvents and dopamine hydrochloride, approximately 0.13 g of dry UND-BNPs (1.7×10^{15} BNPs) were added to the solution and allowed to react under the nitrogen atmosphere overnight. Hexane was then added to the suspension to precipitate the nanoparticles, while the UND acid remained in hexane. After all the particles settled to the bottom, the hexane and the UND acid were removed. The dopamine-coated boron nanoparticles (DA-BNPs) were redispersed in water leading to a solution with a brownish or reddish color. Larger BNPs and aggregates settled on the bottom of the vials after 30 min, but the smaller particles remained suspended in water for over a month. Smaller BNPs were separated by centrifugation（3000 rpm, 10 min), and had a size distribution in the range of 30-40 nm as measured by DLS, TEM and SEM. X-ray photoelectron spectroscopy,

Thermogravimetric Analyses, Mass spectrometry and proton nuclear magnetic resonance (^{1}H NMR, Unity 300) were employed to analyze the surface of these DA-BNPs.

2.2.4 Purification of boron nanoparticles

After the ligand exchange process, the DA-BNPs were purified to remove any free dopamine by either Micro-centrifuge Filters with 5K MWCO cutoff (Sigma), or Slide-A-Lyzer Dialysis Cassettes with 3.5K MWCO cutoff (Thermal Scientific). Centrifugation at 12,000 rpm for 10 min was employed to centrifuge the samples 4-5 times. The dialysis cassettes were placed in 400 mL beakers filled with water for 12 h (replacing water every 4 h).

2.2.5 Mass spectrometry analysis of the particles

The dopamine-modified BNPs (17.6 mg, containing 2.53×10^{14} BNPs), purified by dialysis, were placed in 3.2 mL aqueous solution of hydrochloric acid (pH = 2) to remove the dopamine from the surface of the particles. The particles were allowed to remain in the acidic solution for 72 h to ensure the complete removal of the dopamine. The solution was then placed in the centrifuge to remove the solids, and the supernatant was collected. A control sample was also prepared in the same fashion but with neutral aqueous solution. Mass spectrometry (Waters ESI-TQD) was then used to determine if dopamine was present in the supernatants. A standard addition analysis was then performed for the supernatant prepared under the acidic conditions to determine the amount of dopamine on the surface of the DA-BNPs. Aliquots, ranging from 50 to 400 mL, of a 116 ppm standard dopamine solution were added to 200 mL of the supernatant and diluted to a total volume of 1 mL. The dopamine intensities were recorded with different added amounts of dopamine and plotted to find the concentration of dopamine

in the supernatant. The concentration of dopamine in the unknown was found by solving for Y = 0 of the linear equation and accounting for the dilution. By plotting intensity vs. dopamine concentration in ppm ($Y = 6.44 \times 10^4 X + 4.42 \times 10^6$), we found that the supernatant contained 1.10 mg of dopamine (4.32×10^8 molecules). This information was used to calculate the number of dopamine molecules on the surface of DA-BNPs assuming 40 nm diameter particles.

2.2.6 Attachment of fluorescent tags

The reaction of O-phthaldialdehyde (OPA) with the primary amine containing BNPs in the presence of β-mercaptoethanol (BME) took place in water (Figure 2.1). [27] The OPA solution was made by dissolving 40 mg of OPA in 1 mL of methanol. The solution was then added to 1.2 mL of the purified DA-BNP solution followed by the addition of 200 µL of BME and diluted with 48 mL of water. The fluorescence was measured after 15 min reaction time. The resulting particles had blue fluorescence with maximum emission peak at 455 nm.

2.2.7 PEGylation of boron nanoparticles

Polyethylene glycol (PEG) is well-known as a biocompatible ligand that allows a slowed clearance of the nanoparticles from the blood and makes for a longer acting

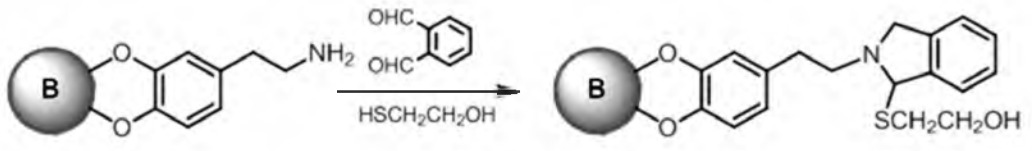

Figure 2.1. Fluorescent tag attachment: OPA reacts with primary amine on the surface of BNPs.

medicinal effect.[28,29] 10 mg PEG (n) monomethyl ether, mono (succinimidyl succinate) ester (2000 Da) were added into DA- BNPs solution and reacted overnight (Figure 2.2). The resulting DA-PEG covered boron nanoparticles (DA-PEG -BNPs) were analyzed by TGA.

2.2.8. Preliminary cell study

Murine macrophage cell line RAW264.7 was obtained from ATCC (Manassas, VA) and was maintained in Dulbecco's Modified Eagle's medium (ATCC) supplemented with 10% fetal bovine serum (HyClone, Logan, UT). Cells were cultured at 37 °C in 5% CO2 and 95% humidified air, and kept in logarithmic phase of growth throughout all experiments.

For morphological study, RAW264.7 cells were plated at the initial density 20,000 cells/cm^2, and 24 h after plating, were exposed to 10% (v/v) of the original concentration of BNPs. After 72 h incubation, cell morphology was assessed with a Nikon Diaphot-300 phase-contrast microscope (Nikon, Melville, NY). Images were captured using Nikon DXM1200C digital camera and ACT-1C 1.01 software.

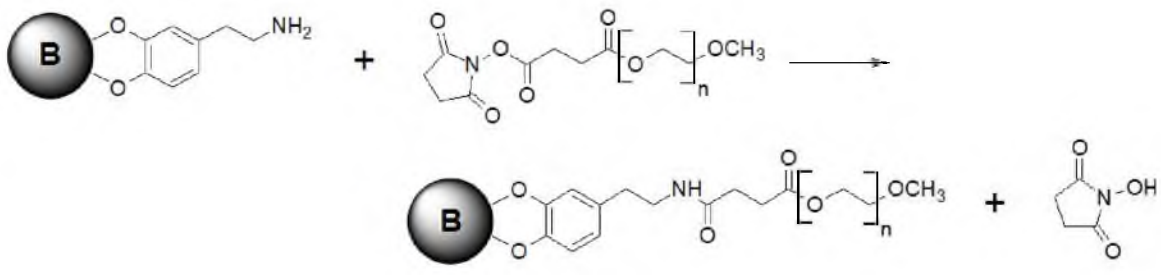

Figure 2.2. The reaction between dopamine coated boron nanoparticles and PEG.

4 mg of DA-OA-B was redisperesed in 3 mL ethanol via sonication. 13.4 mg of rhodamin B isothiocyanate or 22.8 mg fluorescein isothiocyanate (FITC) was added into the BNP suspension and followed by 5 h reaction with continuous stirring. The purification was done through a dialysis process against water. The resulting dye labeled DA-OA-BNPs incubated with RAW264.7 cells for 6 h.

2.3 Results and discussion

2.3.1 Preparation and characterization of dopamine-modified boron nanoparticles

The surfactant-assisted ball milling method was originally designed to produce oxide-free, hydrophobic BNPs stabilized by fatty acid ligands, e.g., oleic acid (OA).[22,23] Such particles are not suitable for bio-applications because of their hydrophobic nature. To change their surface properties, we considered ligands with high boron-affinity, such as diols, glycerols, and other molecules with more than one hydroxyl group. [30-32] However, moieties containing flexible linkers between hydroxyl groups might result in binding to other BNPs, leading to severe coalescence. On the other hand, molecules with two hydroxyl groups attached to a rigid unit should be able to bind to the same boron particle simultaneously without causing particle aggregation. Dopamine is known to form bidentate bonds to metal oxides, such as iron oxide, and to replace oleic acid from the surface of iron oxide nanoparticles.[30,31] Thus, we decided to investigate the possibility of using dopamine in a ligand-exchange reaction with fatty acid-modified boron nanoparticles (Figure 2.3). With the amine group, dopamine should make the BNPs water dispersible and allow for further surface modification of the particles.

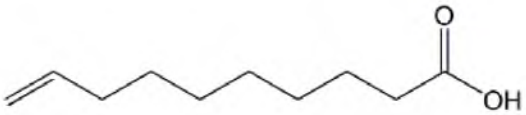

Undecylenic acid

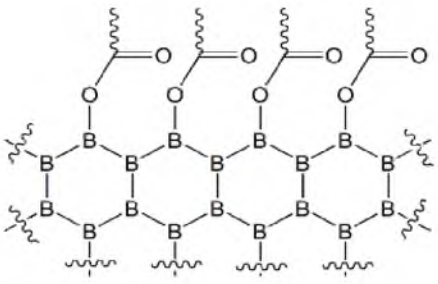

Fatty acid coated BNP surfaces

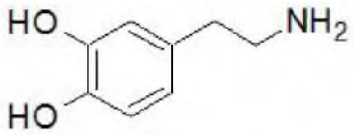

Dopamine

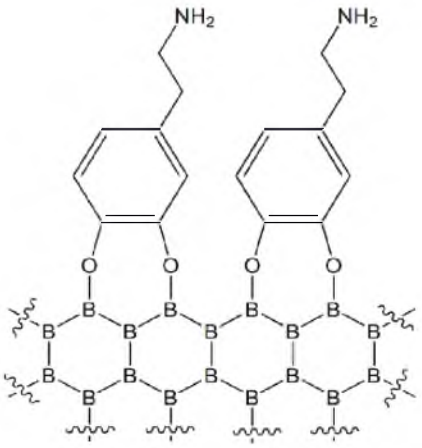

Dopamine coated BNP surfaces

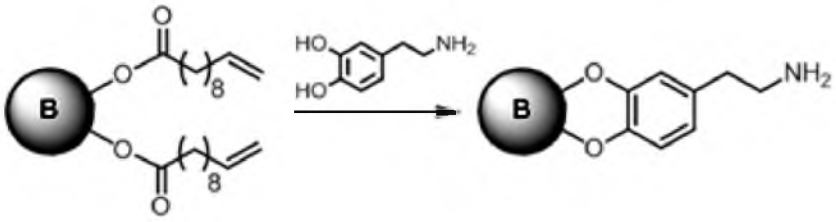

Figure 2.3. The molecule structures of dopamine, undecylenic acid and the scheme of ligand exchange on the BNPs.

In order to perform the ligand exchange, we treated UND-BNPs with dopamine hydrochloride in a 2:1 mixture of chloroform and DMF at room temperature under the nitrogen atmosphere. The resulting nanoparticles would not redisperse in hexane, but could be dispersed in water (Figure 2.4), indicating that the surface of these particles became hydrophilic after the ligand exchange.

The size distribution and surface morphology were obtained by TEM. TEM is a standard imaging technique to study the morphology and particle size distribution for nanoparticles depending on the penetration of electron beam at high voltage.[33] Upon solvent evaporation during the TEM sample preparation, the particles became aggregated and most of the TEM images were obtained for agglomerates of the particles.[34] Since boron has a low electron density, it was difficult to find separated BNPs under the scope. As evident from TEM image analysis, BNPs were produced with diverse morphology due to the mechanical ball milling. However, irregularly shaped BNPs with the average diameter of 33 nm still could be identified (Figure 2.5).

Figure 2.4. DA-UND-B (left) suspended in water and UND- B (right) settled on the bottom of the vial in water.

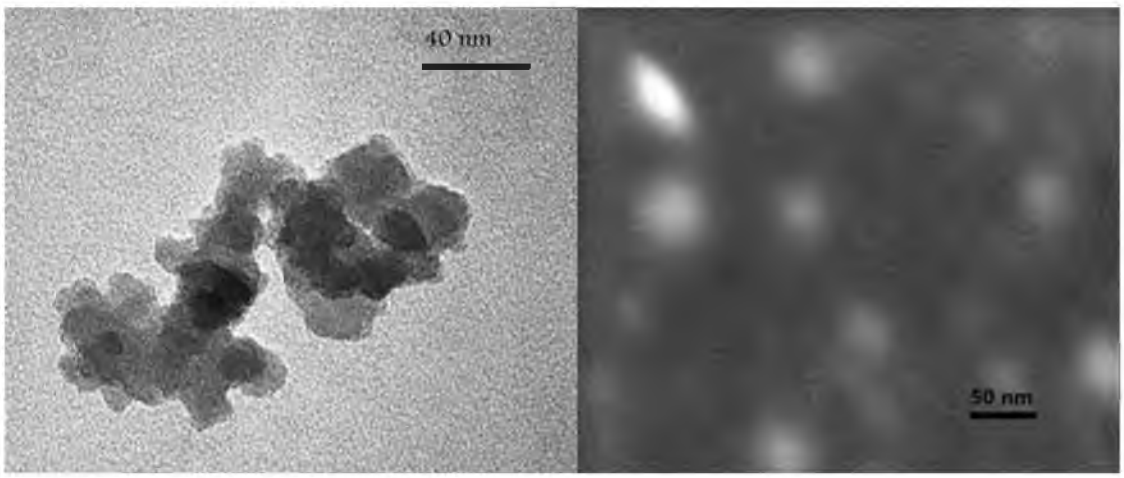

Figure 2.5. Representative TEM (left) and SEM (right) images of DA-BNPs.

The size distribution and surface morphology were also observed by SEM. DA-BNP samples for SEM were prepared by drying a drop of the BNP solution on a copper grid. Based on SEM images (Figure 2.5), the average diameter of dopamine-covered boron nanoparticles was about 40 nm.

Both of the TEM and SEM require the sample in a solid, dry state and do not provide hydrodynamic size of the nanoparticles in solution. Therefore, the electron microscopy techniques are usually combined with dynamic light scattering (DLS) to further investigate the size profile of the particles. The particles were suspended in water, and the DLS measurements were performed at room temperature and a scattering angle of 90°. Since these particles were produced by the milling machine, they were not uniform and had a broad size distribution. Even after the small particles were purified by centrifugation, they showed a broad major peak (up to 99.8%) ranging from 11-70 nm with an average diameter of 38 nm by DLS (Figure 2.6). The second peak which was around 150 nm was due to the remaining large particles or aggregation of the particles.

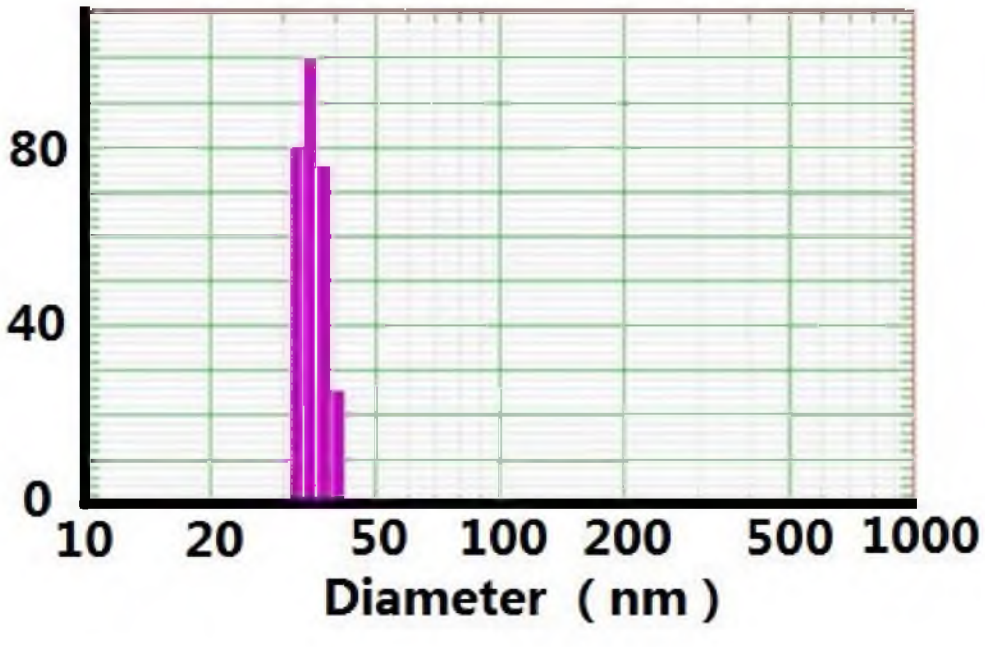

Figure 2.6. Distribution of DA-UND-B according to DLS.

The surface characteristics have a profound influence on the interaction of the BNPs with water or other mediums, controlling the dispersibility of the particles and their cytotoxicity. The DA-modified nanoparticles were studied by XPS to examine their surface composition. An intense peak of chloride interfering with boron peak was detected for the unpurified sample while purified samples did not possess this peak. The chloride originated from dopamine chloride. Therefore, its disappearance in purified samples demonstrated the success of the purification process by dialysis. Most importantly, the presence of an N 1s peak (Figure 2.7) confirmed the presence of dopamine on the surface of DA-BNPs.

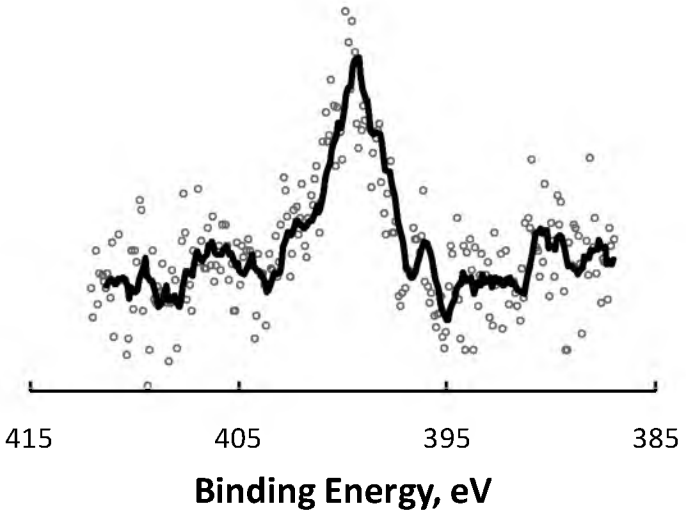

Figure 2.7. XPS data for N 1s of DA-BNP particles.

As seen in the B 1s photoelectron spectra of the purified, dried DA-BNP sample (Figure 2.8), the DA-BNPs possess two peaks: the most intense one for elemental boron at 189 eV; and the second peak at 193 eV, which can be identified as the BxOy peak. [35] After analyzing as-prepared samples, they were sputtered with argon. Longer sputtering times led to a higher percentage of elemental boron on the surface; and after 6 minutes of argon sputtering, the BxOy peak decreased significantly, suggesting that the majority of the oxide was due to physisorbed oxygen. The oxide formation may originate from UND-BNPs whose surfaces were not fully covered by UND acid. Regardless of the boron oxide presence, DA-BNPs can generate high linear transfer energy particles, and thus, can be used as a BNCT agent.[20]

Thermogravimetric data for dopamine-modified BNPs were collected to further study the surface coverage of these nanoparticles. TGA measurements were first performed under the nitrogen atmosphere to avoid oxidation of boron in the air.

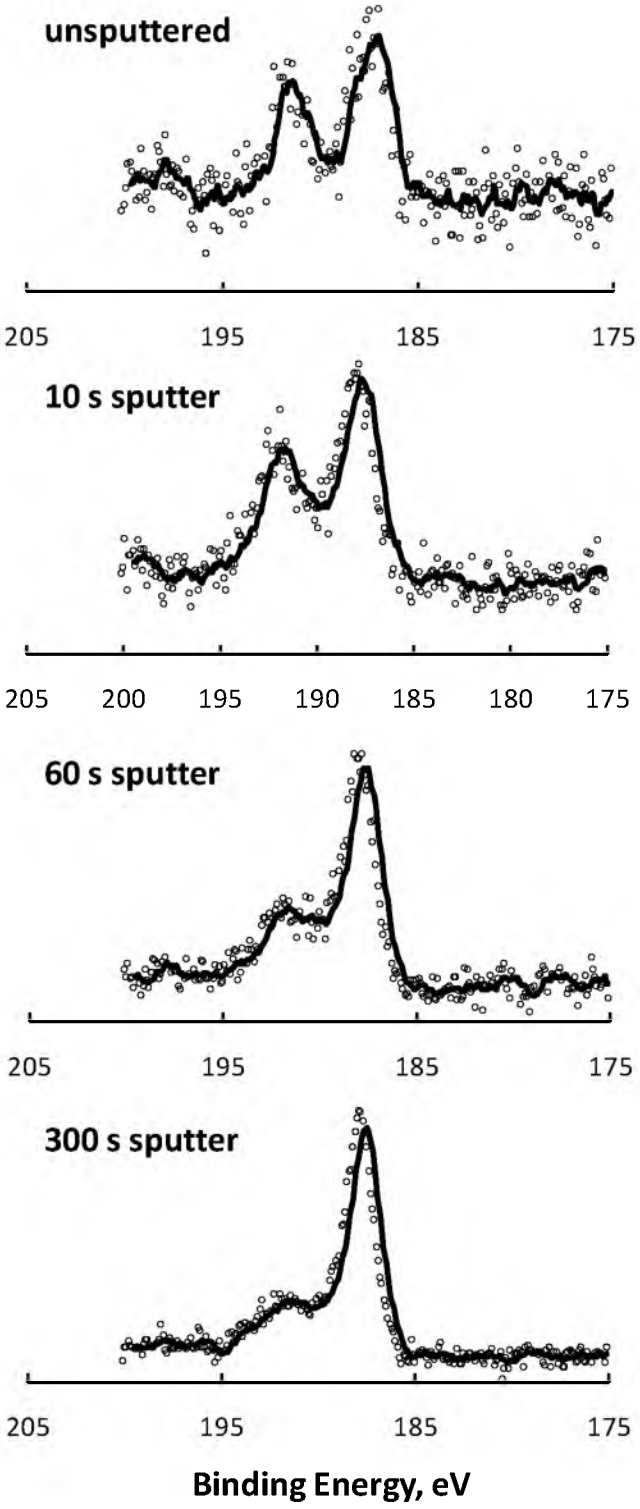

Figure 2.8. 1s XPS pattern of DA-BNP nanoparticles as a function of sputtering time.

However, a gradual weight increase was observed above 600 °C. This may be the result of boron reacting with nitrogen at elevated temperature. It is known that this reaction starts at 320 °C, accelerates at 470 °C, and ignition occurs between 650 and 800 °C.[36] Thus, the observed weight increase might have been caused by the formation of boron nitride. To avoid this problem, TGA analysis was performed under the argon atmosphere. Under these conditions, TGA showed a smaller, but visible weight increase above 600 °C as well (Figure 2.9), possibly due to the presence of impurities in argon. The TGA of DA-BNPs showed the total %w loss of 6.4% at ca. 400 °C, corresponding to four molecules of dopamine per nm^2 of the nanoparticle surface.For comparison, we performed TGA analysis of UND-BNPs. The weight loss of UND-BNPs occurred at ca. 380 °C in one step; the %weight loss was 3.9%, corresponding to two UND molecules per nm^2 of the nanoparticle surface. The lower number of UNDs on the nanoparticle surface may result from the larger size of these molecules. The equation of surface coverage calculation is listed here:

$$\frac{n_{ligand}}{SA} = \frac{W_L \times N_A \times W_{sp}}{M_w \times W_R \times SA_{sp}}$$

where n_{ligand} is the number of the ligands, and SA is the surface area (nm^2), we assumed that the BNPs were spherical and had a uniform size of 40 nm; the surface area equates to $4\pi r^2$, SA_{sp} is the surface area of a single particle (nm^2), W_L is the weight loss percentage, W_R is the weight remaining, W_{sp} is the weight of single particle (g) calculated under the assumption that the particles consist of pure elemental boron.

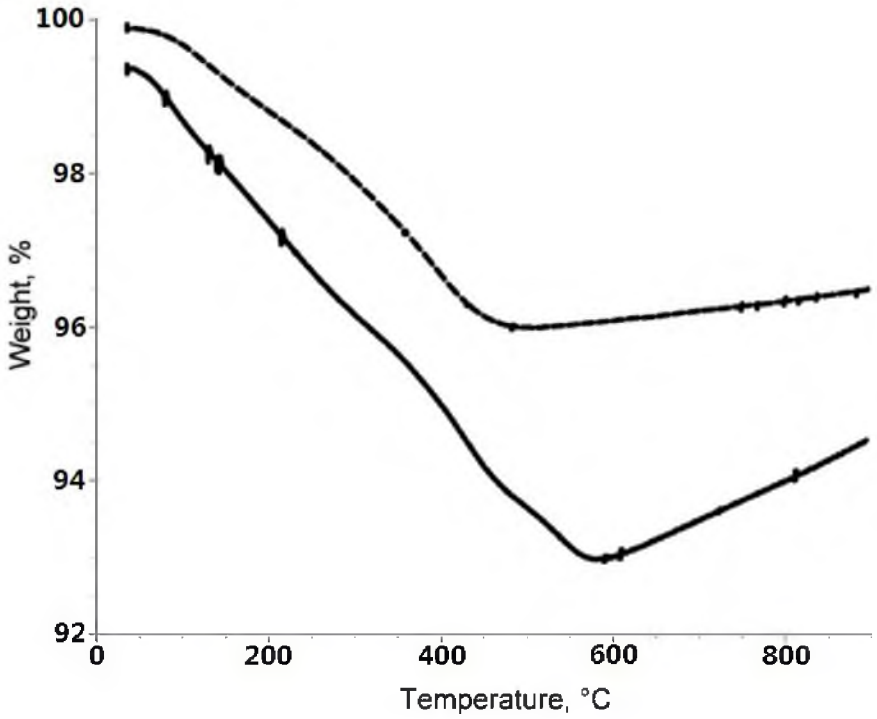

Figure 2.9. TGA plots for UND-BNPs (dashed line) and DA-BNPs (solid line) under nitrogen.

Mass spectrometry was used to analyze solutions obtained from treating DA-BNPs under both neutral and acidic conditions. When the acidic sample was analyzed, a dopamine peak was found with a m/z of 154 (Figure 2.10 upper). However, when the neutral sample was analyzed, no dopamine peak was observed (Figure 2.10 lower). This demonstrates that the dopamine on BNPs are stable in water. Next, we performed a standard addition analysis to find the amount of dopamine present on the BNPs. We added different concentrations of dopamine to the sample and plotted dopamine peak intensity vs. added concentrations of dopamine. Using this method, we calculated that the dopamine coverage of the BNPs was 3.8 DA molecules per nm^2, which is similar to the value determined by TGA.

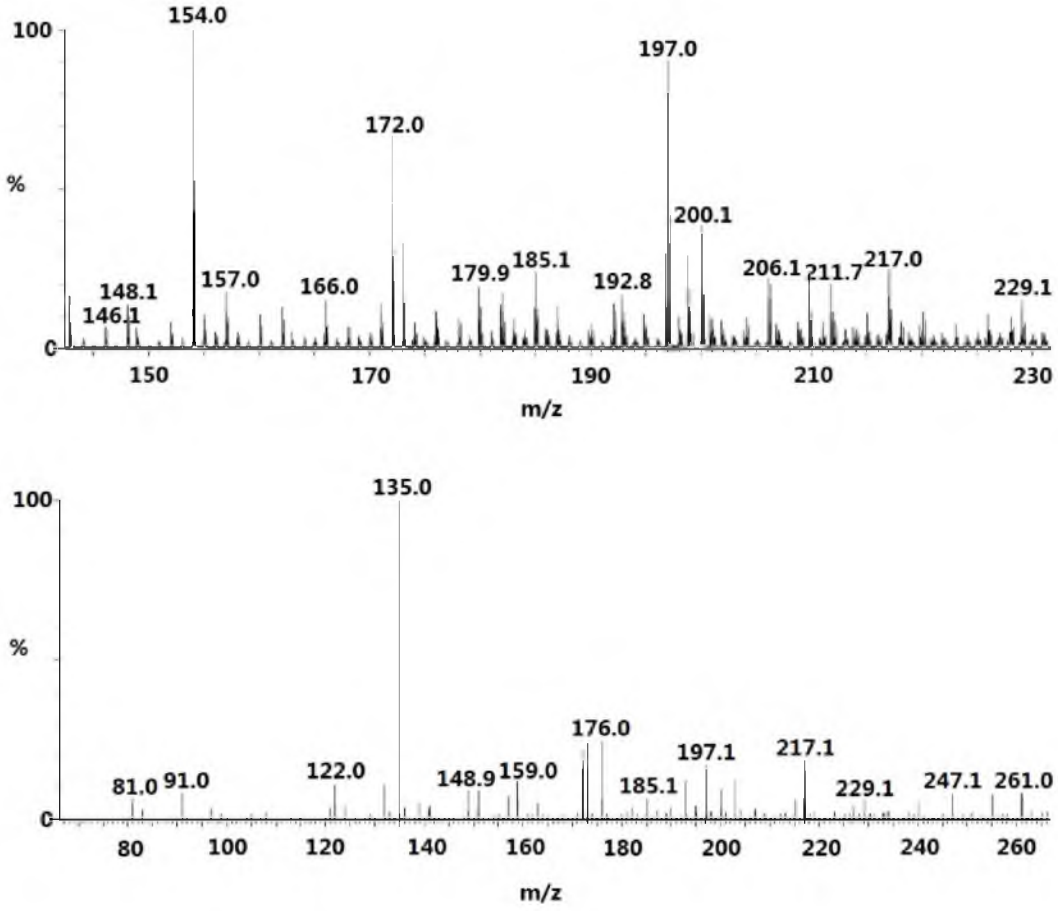

Figure 2.10. ESI-MS spectra of aqueous solutions obtained from DA-BNPs under (upper) acidic and (lower) neutral conditions.

We also attempted to use ^{1}H NMR in D_2O to study the surface information of BNPs. Microcentrifuge filters (5K DA) were used to replace water into D_2O and remove the free DA. However, no NMR signal was detected. This was probably because the rigidity of the surface dopamine structure did not allow for bond rotation, which indirectly supported the idea of dopamine attaching to BNP surface with both of the hydroxyl groups. There was also the possibility that the BNPs were too bulky, or the amount of the dopamine was not enough to be detected by ^{1}H NMR.

2.3.2 Surface modification of DA-BNPs

Fluorescence could be a useful method of locating the BNPs *in vitro*. With this in mind, and to chemically confirm the presence of dopamine on the surface of DA-BNPs, we treated them with an amine-reactive fluorescent dye. The reaction of O-phthaldialdehyde (OPA) with primary amines in the presence of β-mercaptoethanol (BME) takes place in water,[27] and the resulting species possess blue fluorescence with excitation wavelength of 340 nm and emission wavelength at 450 nm.

Thus, we treated DA-BNPs with OPA in water (Figure 2.1). After the purification, the treated particles showed blue fluorescence under the UV light. In order to demonstrate the selectivity of the OPA surface modification, we examined the fluorescence of the following samples: (1) OPA + BME; (2) DA-BNP; (3) DA-BNP + OPA + BME; (4) UND-BNP; (5) UND-BNP + OPA + BME (Figure 2.11). All fluorescence measurements were performed using an excitation wavelength at 325 nm and the emission wavelength in the range from 350 to 600 nm. Figure 2.11 shows five fluorescence spectra, the reference samples of DA and OPA, and surface-modified BNPs. Only the DA-BNPs treated with OPA revealed a fluorescence emission peak at ~455 nm, while the other samples showed no significant emission. This showed that the primary amines on the surface of DA-BNPs reacted with OPA, confirming that dopamine moieties were indeed attached to the BNP surface.

PEGylation, the covalent attachment of PEG, is a proven method to provide nanoparticles with better biocompatibility, resistance to the plasma coadsorption, and longer circulation and body retention. Thus, the DA-UND-BNPs were modified with PEG.[28,29] Figure 2.12 shows the TGAs of UND, DA, DA-PEG covered BNPs in Ar.

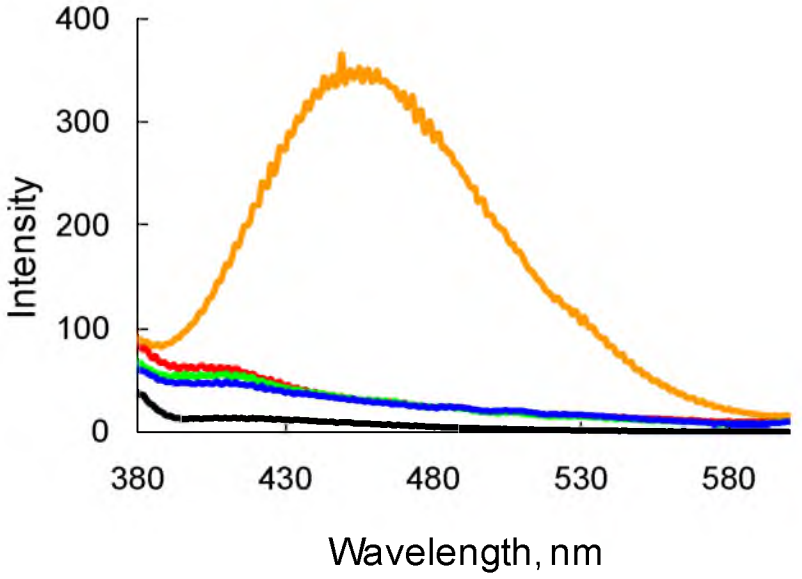

Figure 2.11. Fluorescence spectra for OPA (black), DA-BNPs (red), UND-BNPs (green), DA-BNPs treated with OPA (orange) and UND-BNPs treated with OPA (blue).

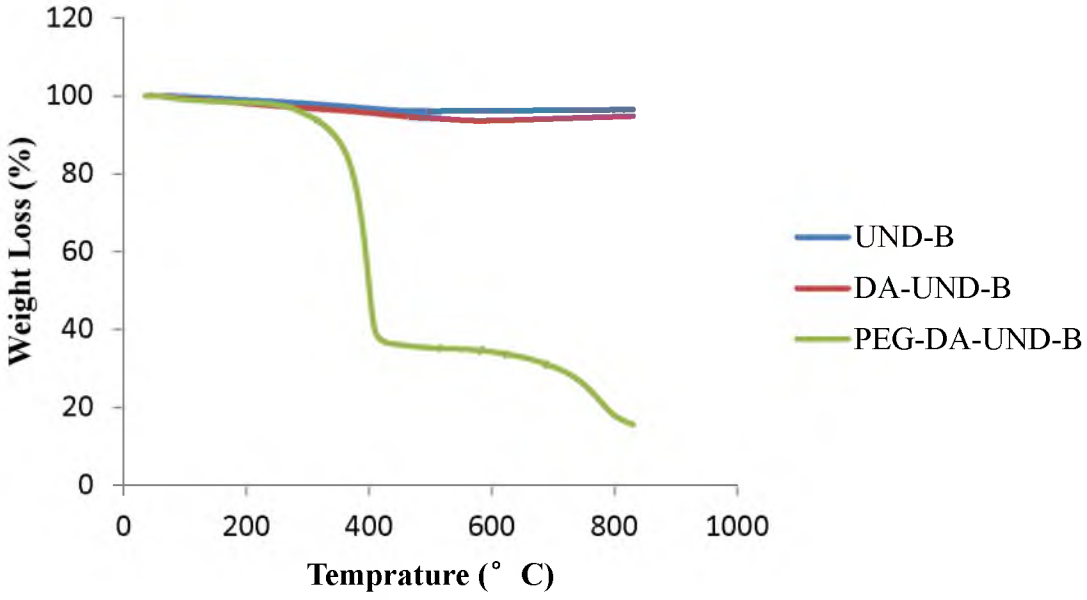

Figure 2.12. TGA plots of UND-BNPs, DA-BNPs and DA-PEG-BNPs

TGA of PEG-coated BNPs revealed a significant weight loss (83%), starting from 200 °C to 400 °C, attributed to the decomposition of PEG. Calculated from the weight loss percentage, the surface coverage of UND acid, DA, DA-PEG, were 2, 4 and 7 ligands/nm^2, respectively. The reason that the PEG coverage was slightly larger than the expected number might be due to the free PEGs that noncovalently attached on the PEGylated BNPs.

2.3.3 The DA-OA-BNPs

The ligand exchange is a versatile method to convert the hydrophobicity of the ball-milled BNPs. Vitamin C with two hydroxyl groups that rigidly bonded on a heterocyclic ring was attached on the surface of the BNPs following the same procedure as DA coating (Figure 2.13). The resulting BNPs can disperse in aqueous solution after the ligand exchange, indicating the success of the vitamin C attachment. Moreover, the OA-BNPs produced by ball-milling with oleic acid as the boron stabilizer were produced and underwent the same ligand exchange procedure as UND-BNPs. The other experiments are based on the dopamine-coated BNPs produced by ligand exchange on the OA-BNPs.

The resulting DA-OA-BNPs showed better colloidal stability in water than the DA-UND-BNPs due to their larger surface charge. Table 2.1 shows the zeta potential discrepancy between the DA-UND-BNPs and DA-OA-B in aqueous solutions. The better dispersibility of DA-OA-BNPs was also demonstrated by TEM images. The particles are more separated from each other, and particle size and morphology were more uniform. The average diameter obtained from the TEM images is 18.2±3.1 nm (Figure 2.14).

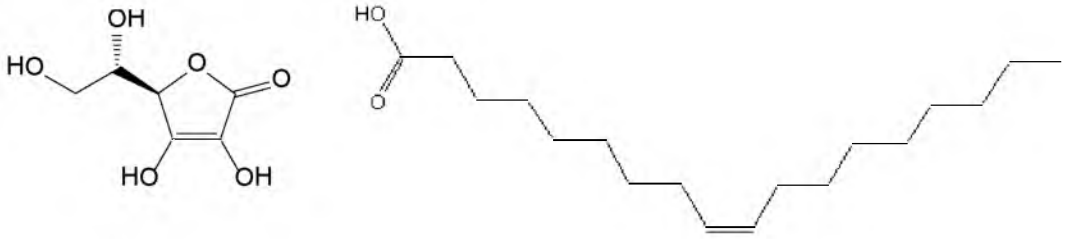

Figure 2.13. The molecular structure of vitamin C and oleic acid.

Table 2.1. Water suspension stability and zeta potential of DA-UND-B and DA-OA-B

Sample	Stability in water	Zeta Potential
DA-UND-BNPs	1 Day	- 2.20 mV
DA-OA-BNPs	months	- 62.73 mV

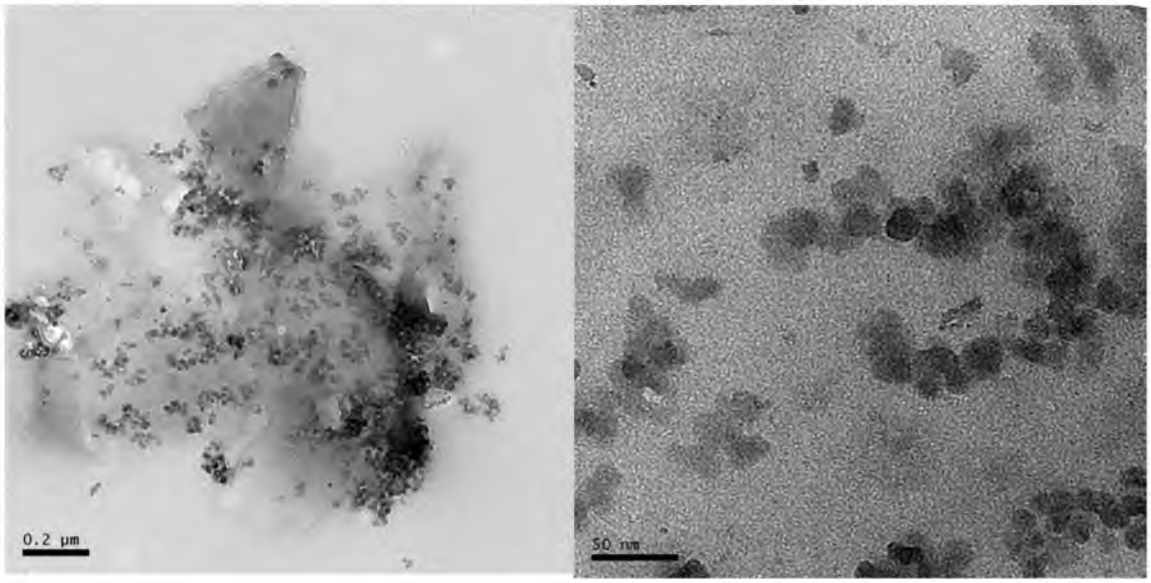

Figure 2.14. The TEM images for DA-OA-BNPs.

The IR spectrum of DA-OA-BNPs shows that the dopamine was modified on the surface of the BNPs (Figure 2.15). The intensive peak at 1720 cm^{-1} is attributed to the C=O from the fatty acid residue on the BNPs. Not all of the fatty acids were replaced by dopamine, and the negative surface charge of DA-BNPs in aqueous solution contributed to the carboxyl groups left on the boron surface. The strong bands at 1210 cm^{-1} (C-N vibration) and 1550 cm^{-1} (NH_2 scissoring) are characteristics of primary amine suggesting the presence of dopamine.

It is known that dansyl chloride reacts with primary amine and generates fluorescence emission under the UV irradiation. This approach is frequently used to demonstrate the presence of primary amine. The ethanolic suspensions of the same

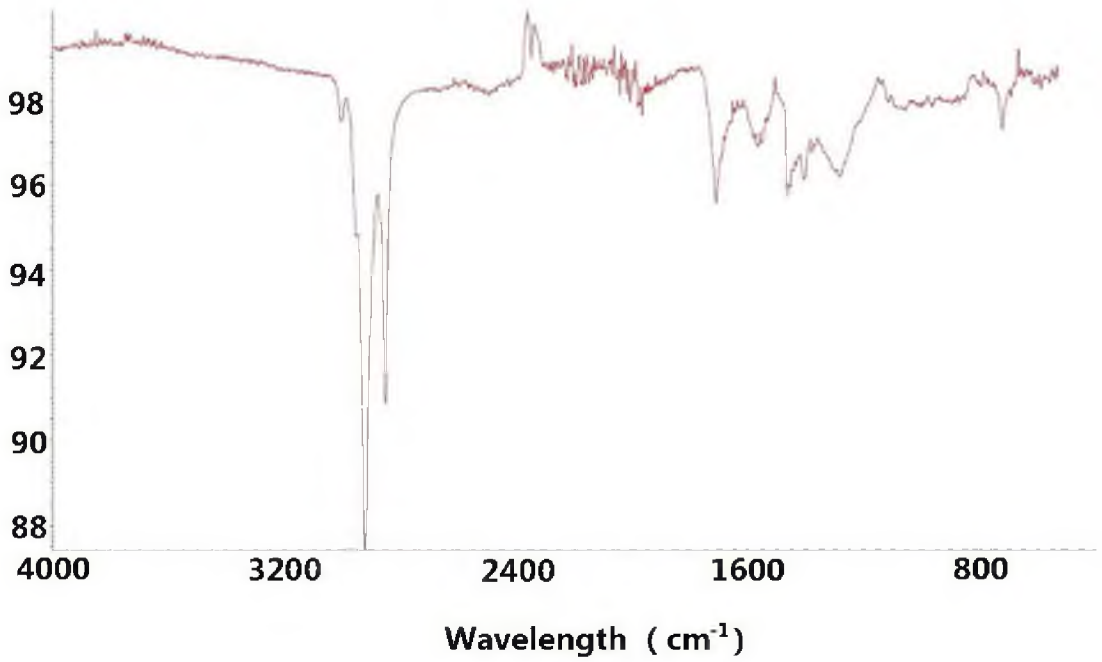

Figure 2.15. IR spectrum of DA-OA-BNPs.

amount of DA-OA-BNPs and OA-BNPs were prepared by sonication. After the addition of the dansyl chloride solution, the DA-OA-BNPs suspension emitted the green fluorescence indicating the presence of primary amine on the DA-OA-BNPs particles. The OA-BNPs suspension was used as a comparison, which remained nonluminous under the UV light (Figure 2.16).

2.3.4 Preliminary cell toxicity study of DA-BNPs†

Macrophages are immune system-related cells that are abundantly present at inflamed areas and many important organs such as the liver, lung, spleen, and bone

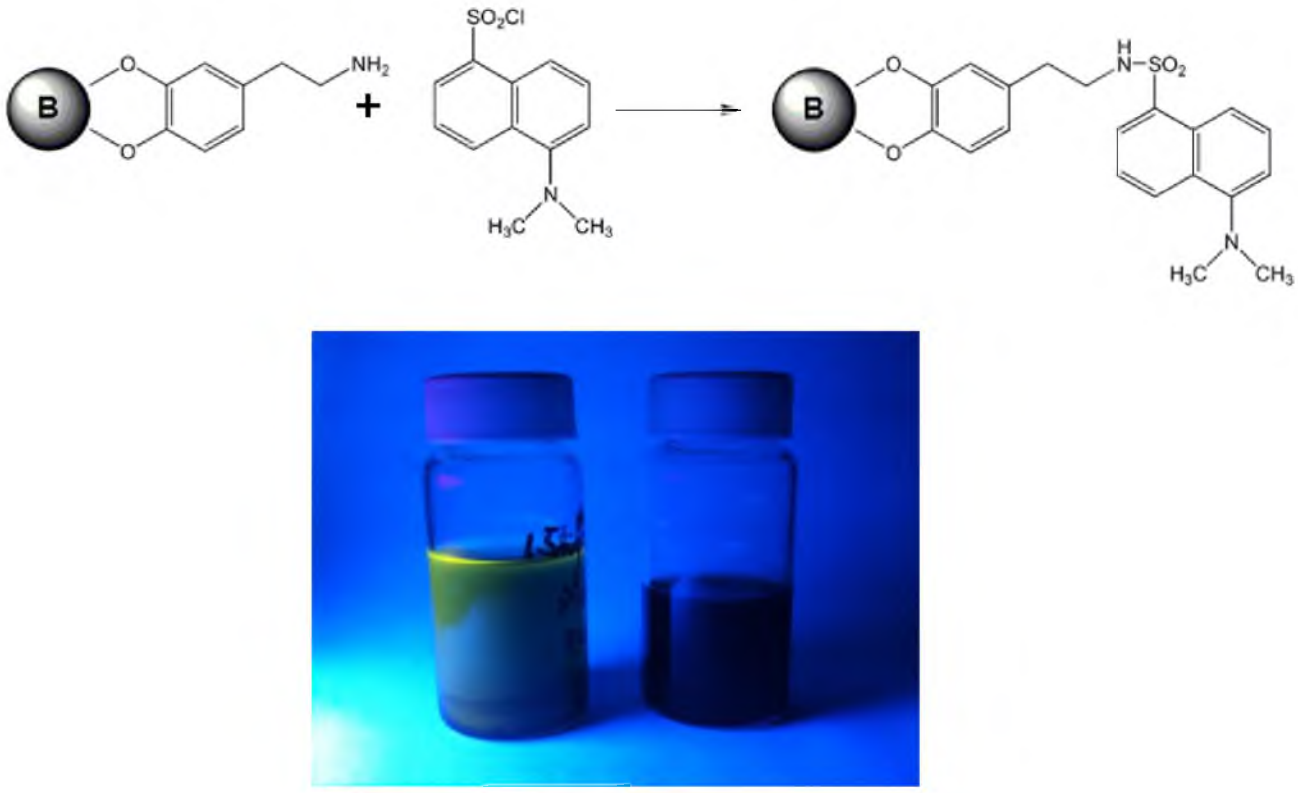

Figure 2.16. The reaction of DA-OA-B with dansyl chloride generated fluorescence under the UV light (left); the OA-B ethanolic solution with the addition of dansyl chloride generated no fluorescence (right).

† performed with the help of Dr. Alexander Malugin, Department of Pharmaceutics and Pharmaceutical Chemistry, University of Utah.

marrow.[37] Taking advantage of their ability to scavenge nanoparticles and their distribution, drug delivery researchers often study the interaction of the nano-carriers with macrophages.[38] We performed preliminary biological evaluation of BNPs on a murine peritoneal macrophage cell line RAW264.7. This cell line possesses many essential characteristics of 'professional' phagocytes: it secretes lysozymes; expresses Fc receptors for immunoglobulins; and it is capable of antibody-dependent lysis of sheep erythrocytes and tumor cell targets, as well as pinocytosis and phagocytosis.[39] RAW264.7 cells are a widely used as a model cell line to study the interaction of nanomaterials with biological systems.

To avoid the potential interference from synthesis residues and solvents prior to incubation with the cells, DA-BNPs were purified by extensive dialysis against a large amount of millipore water. The resulting suspension was separated by ultracentrifugation; the supernatant collected and solid nanoparticles re-dispersed in water at 0.25 mg/mL concentration, which was determined gravimetrically. DA-BNPs were added to RAW264.7 cells at 10% (v/v) of the original concentration, and cells were incubated with DA-BNPs for 72 h. Cells treated with the same volume of millipore water containing no DA-BNPs were used as control. Since the particles and the supernatant were prepared at usual lab environment and were not sterile, bacterial contamination of cultured media was observed in 4-5 days. Incubation of RAW264.7 cells with DA-BNPs (or with their supernatant) resulted in no apparent changes of cell confluency or cell density, indicating that neither BNPs suspension nor the supernatant of freshly prepared plain BNPs appeared to be toxic toward RAW264.7 cells after 72 h of continuous incubation. The morphology of the RAW264.7 control cells and cells grown in the presence of DA-BNPs

in the DMEM with 10% serum showed little difference (Figure 2.17). The majority of the cells in both cultures had a spherical morphology typical for RAW264.7 at high cell density. The only noticeable difference was a slightly higher proportion of spread, elongated cells with dendritic-like morphology in the culture treated with DA-BNPs. A similar phenomenon was observed with cells that incubated with the supernatant. These morphology changes due to the cytoplasmic spreading could be a result of macrophages activation, which was observed in the cells incubated with SiNPs.[40]

Rhodamine B isothiocyanate and FITC were attached to the DA-OA-BNPs in order to obtain fluorescently-labeled BNPs suitable for investigating the cellular uptake of DA-BNPs by macrophage cell lines, RAW 264.7. The rhodamine B and FITC labeled DA-BNPs incubated with RAW264.7 cells for 6 h, and the interaction of dye-labeled BNPs with RAW 264.7 cells was detected by confocal microscopy (Figure. 2.18). Black spots in Differential Interference Contrast Microscopy (DIC) images represented the aggregation of BNPs. The observable BNP aggregations were distributed on the cell membranes. The intensity of green color represented the rhodamine B-labeled BNPs, and purple color corresponded to the nucleus stained with DRAQ5 (magenta). Both diffused and spot-like fluorescence distributions were observed. Diffused fluorescence staining was found in the cytoplasm and nucleus of some cells indicating that dye-labeled BNPs enter RAW264.7 cells. Similar fluorescence staining was observed for FITC-labeled BNPs, but images were not taken due to bacterial contamination of the sample. It appeared that BNPs' association with cells was uneven: there were cells completely without BNPs, and there were cells that accumulated a significant amount of BNPs.

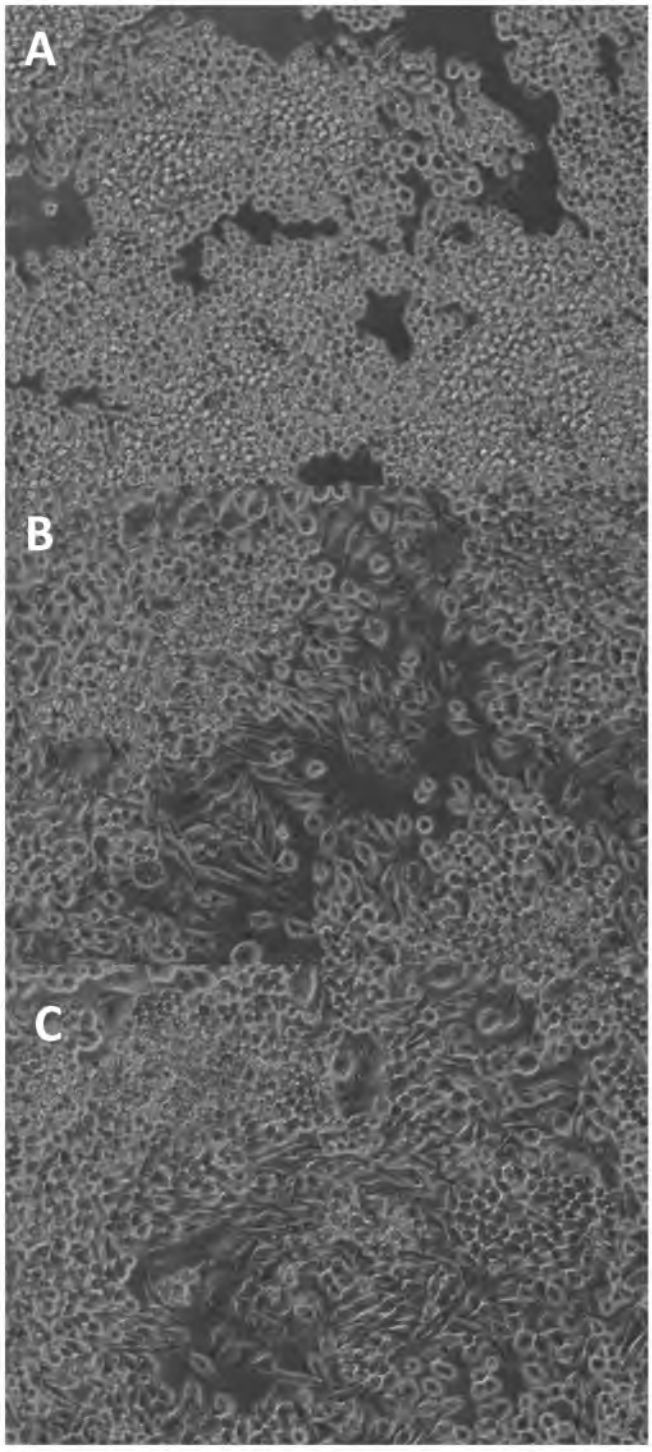

Figure 2.17. Phase-contrast images of RAW264.7 cells: (A) control; (B) incubated with DA-BNPs for 72 h; (C) incubated with DA-BNPs supernatant for 72 h Images were taken at 20X magnification.

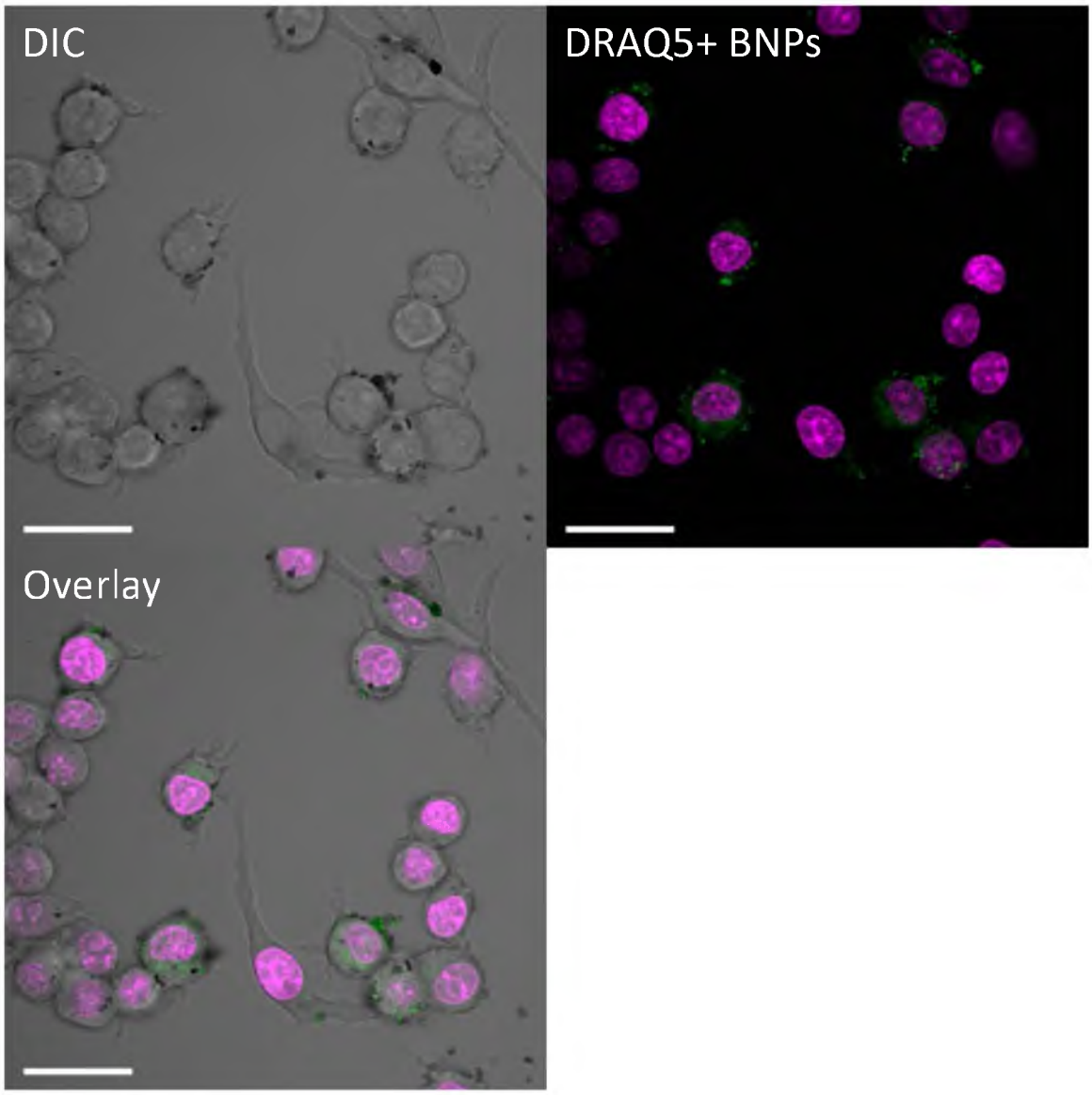

Figure 2.18. Cellular internalization (association) of rhodamine-labeled BNPs (pseudo-green) after 6 h incubation with RAW264.7 cells. Single plain scan was used for DIC and overlay images. Z-stack scans were used for fluorescence combined image. Representative images are shown. Scale bar is 20 μm.

2.4 Conclusion

We have developed a versatile method to attach dopamine to the surface of boron nanoparticles (BNPs) by replacing fatty acids on the surface. TGA and XPS measurements, as well as fluorescent-dye modification, confirmed that these nanoparticles carry dopamine ligands on their surfaces. DA-BNPs are water dispersible and DA-OA-B suspensions are colloidal stable in water for months. In the concentration studied, DA-BNPs did not show signs of toxicity toward murine macrophage cells and the DA-BNPs were able to enter the cells. These results suggest that DA-BNPs are promising agents for boron neutron capture therapy.

2.5 References

[1] Barth, R. F.; Coderre, A.; Vicente, M.; Blue, T. E. *Clin. Cancer Res.*, **2005, *11***, 3987-4002.

[2] Hawthorne, M. F. *Angew. Chem. Int. Ed.*, **1993**, *32*, 950-984.

[3] Valliant, J. F.; Guenther, K. J.; King, A. S.; Morel, R.; Schaffer, P.; Sogbein O. O.; Stephenson, K. A. *Coord. Chem. Rev.*, **2002**, *232*, 173-230.

[4] Nigg, D. W. *J Neurooncol.*, **2003**, *62*, 75-86.

[5] Javid, M.; Brownell G. L.; Sweet, W. H. *J. Clin. Invest.*, **1952**, *31*, 604-610.

[6] Tolpin, E. I.; Wellum, G. R.; Jr Dophan, F. C.; Kornblith, P. L.; Zamenhof G. Z., *Oncology*, **1975,** *32*, 223-246.

[7] Isaac, M. F.; Khal, S. B. *J. Organomet. Chem.*, **2003**, *680*, 232-243.

[8] Ceberg, C. P.; Brun, A.; Kahl, S. B.; Koo, M. S.; Persson. B. R.; Salford, L. G. *J. Neurosurg.*, **1995**, *83*, 86-92.

[9] Kabalka, G. W.; Yao, M. L. *Synthesis*, **2003**, *18*, 2890-2893.

[10] Diaz, A.; Stelzer, K.; Laramore, G.; Wiersema, R. *Research and Development in Neutron Capture Therapy*; Monduzzi Editore: Bologna, **2002**, 993-999.

[11] Yang, W.; Wu, G.; Barth, R. F.; Swindall, M. R.; Bandyopadhyaya, A. K.; Tjarks, W.; Tordoff, K.; Moeschberger, M.; Sferra, T. J.; Binns, P. J.; Riley, K. J.; Ciesielski, M. J.; Fenstermaker, R. A.; Wikstrand, C. J. *Cancer Res.*, **2008**, *14*, 883-891.

[12] Tietze, L. F.; Griesbach, U.; Bothe, U.; Nakamura H.; Yamamoto, Y. *Chembiochem*, **2002**, *3*, 219-225.

[13] Woodhouse, S. L.; Rendina, L. M. *Chem. Commun.*, **2001,** 2464-2465.

[14] Nakamura, H.; Miyajima, Y.; Takei, T.; Kasaoka, S.; Maruyama, K. *Chem. Commun.*, **2004**, 1910-1911.

[15] Hatanaka, H. A. *J. Neurol.*, **1975**, *209*, 81-94.

[16] Mishima, Y.; Ichihashi, M.; Tsui, M.; Hatta, S.; Ueda, M.; Honda, C.; Susuki, T. *Lancet* , **1989**, *2*, 388-389.

[17] Hwang, K. C.; Lai, P. D.; Chiang, C. S.; Wang P. J.; Yuan, C. Y. *Biomaterials*, **2010**, *31*, 8419-8425.

[18] Kennedy, D. C.; Duguay, D. R.; Tay, L. L.; Richeson, D. S.; Pezacki, J. P. *Chem. Commun.,* **2009**, 6750-6752.

[19] Mortensen, M. W.; Sorensen, P. G.; Bjorkdahl, O.; Jensen, M. R.; Gundersen, H. J. G. Bjornholm, T. *Appl. Radiat. Isot.,* **2006**, *64*, 315-324.

[20] Petersen, M. S.; Petersen, C. C.; Agger, R.; Sutmuller, M.; Jensen M. R.; Soerensen, P. G.; Mortensen, T.; Hansen, M. W.; Bjoerholm, T.; Gundersen, H. J.; Huiskamp, R.; Hokland, M. *Anticancer Res.* **2008**, *28*, 571-576.

[21] Soloway, A. H.; Tjarks, W.; Barnum, B. A.; Rong, F. G.; Barth, R.F.; Codogni, I. M.; Wilson, J. G. *Chem. Rev.* **1998**, *98*, 1515-1562

[22] Van Devener B.; Perez J. P. L.; Anderson S.L. *J. Mater. Res.*, **2009** *24*, 2462-2464.

[23] Van Devener B.; Perez J. P. L.; Jankovich J.; Anderson S.L, *Energy Fuels,* **2009**, *23*, 6111-6120.

[24] Wang, Y.; Li, Y.; Rong, C.; Liu, J. P. *Nanotechnology,* 2007, **18**, 465701/1-4.

[25] Yue, M.; Wang, Y. P.; Poudyal, N.; Rong, C. B.; Liu, J. P., *J. Appl. Phys.*, 2009, **105**, 07A708/1-5.

[26] Rajh T., Nedeljkovic J. M.; Chen L.X.; Poluektov O.; Thurnauer M. C. *J. Phys. Chem. B* **1999**, *103*, 3515-3519.

[27] Church F. C.; Swaisgood H. E., Porter D.H., Catignani G. L. *J. Dairy Sci* **1983**, *66*, 1219-1227.

[28] Cauda, V.; Argyo, C.; Bein, T.; *J. Mater. Chem.*, **2010**, *20*, 8693-8699.

[29] Britcher, L.; Barnes, T. J.; Griesser, H. J.; Prestidge, C. A. *Langmuir* **2008**, *24*, 7625-7627.

[30] Xu, C,; Xu, K.; Gu, H.; Zheng, R.; Liu, H.; Zhang, X.; Guo, Z.; Xu, B. *J. Am. Chem. Soc.*, **2004**, *126*, 9938-9939.

[31] Peng, S.; Wang, C.; Xie, J.;Sun, S. *J. Am. Chem. Soc.* **2006**, ***128***, 10676-10677.

[32] Rajh T., Chen L.X., Lukas K., Thurnauer M. C., Tiede D. M. *J. Phys. Chem. B* **2002**, *106*, 10543-10552.

[33] Erni, R.; Rossell, M. D.; Kisielowski, U.; Dahmen, U. *Phys. Rev. Lett* **2009**, *102*, 0961601/1-4.

[34] Pascal, C.; Pascal, J. L.; Favier, F.; Elidrissi, M. L.; Moubtassim, M. L.; Payen, C. *Chem. Mater.*, **1999**, *11*, 141-147.

[35] Wagner, C. D.; Naumkin, A.V.; Kraut-Vass, A.; Allison, J. W.; Powell, C. J.; Rumble Jr., J. R. NIST X-ray Photoelectron Spectroscopy Database, NIST Standard Reference Database 20, Version 3.5, **2003**.

[36] Li, S.; Jin, R.; Guo, J. *Energetic Mater.*, **1996**, ***4***, 102-108.

[37] Fischer, H. C.; Chan, W. C. *Curr. Opin. Biotechnol.* **2007**, 18, 565-571.

[38] Park, M. V. D. Z.; Lynch, I.; Ramírez-García, S.; Dawson, K. A.; de la Fonteyne, L.; Gremmer, E.; Slob, W.; Briedé, J. J.; Elsaesser, A.; Howard, C. V.; van Loveren, H.; de Jong, W. H. *J. Nanopart. Res.* **2011**, *13*, 6775-6787.

[39] Raschke, W. C.; Baird, S.; Ralph, P.; Nakoinz, I. *Cell,* **1978**, *15*, 261-267.

[40] Park, E.; Park, J. *Toxicology Letters* **2009**, *184*, 18-25.

CHAPTER 3

TANNIC ACID-TEMPLATED LARGE-PORE MESOPOROUS SILICA NANOPARTICLES

3.1 Introduction

Because of their unique features, such as mesoporous structures, high surface area and easily functionalized surface, mesoporous silica nanoparticles (MSNs) have many potential applications[1] as delivery agents for drugs and biomolecules,[2] and as host materials for catalysis, imaging and sensing.[3-6] To fulfil this promise, MSNs should be created with a narrow size range in the nanoscale, preferably 50 to 200 nm, to facilitate entrance into the cell, and with large pores to encapsulate large pharmaceuticals and biomolecules such as proteins, enzymes and nucleotides. In the past decades, numerous strategies were developed to produce a variety of mesoporous silica materials with diverse morphologies, pore sizes and pore arrangements.[7,8] The particle size and morphology can be controlled by tailoring the molar ratio of silica precursor and surfactant; pH can be controlled by using base catalyst with the addition of co-solvents or organic swelling agents, and introduction of organoalkoxysilane precursors during the co-condensation reaction.

Size of the particles is a crucial factor that affects their permeability into the tissue membranes in vitro and bio-distribution in vivo. A study comparing the cellular association of MSNs with different sizes by cancerous epithelial cells concluded that

cellular uptake of MSNs is size-dependent, and that cells uptake smaller particles better.[9] Therefore, the size control of the particles is crucial to design and synthesis materials for drug delivery systems.[10] Mou and coworkers have manipulated the diameter of the MCM-41 nanoparticles from 30 to 280 nm;[11] however, the maximum pore size was limited to 6 nm, which limits their application as a carrier for adsorption and releasing large molecules. SBA-15 is the most studied large-pore mesoporous material and was first reported by Stucky group.[12] By varying the nonionic triblock-copolymer as the surfactant template, and the use of co-solvent and swelling agents, the pore size of SBA-15 can be controlled from 6 to 50 nm. However, the size of the smallest SBA particles reported so far is around 500 nm, which is not suitable for intracellular applications.[13,14] Ying et al. describe a method to produce polydispersed mesoporous SiNPs (50-300 nm) with tuneable pore sizes from 5 to 30 nm from a dual-surfactant system: a nonionic tricopolymer surfactant is used to template the porous structure (a swelling agent is used to increase the pore size) and a cationic fluorocarbon surfactant is used to manipulate the particle size.[15] However, the technique of controlling the uniformity of the dual-surfactant templated MSNs is not fully developed.[16]

Despite encouraging progress in controlling the morphology and pore size of the mesoporous materials, a simple route to synthesize monodispersed, relatively large-pore mesoporous silica nanospheres—whose sizes are smaller than 200 nm—still remains a challenge. Herein, we present a "one-pot" synthesis route of novel mesoporous silica nanoparticles with a tunable pore size from 5-13 nm by an ammonia catalyzed sol-gel reaction in the presence of an environmentally friendly nonsurfactant pore-forming agent, tannic acid (TA). The pore size of the tannic acid templated (TA-TEOS) silica

nanoparticles (NPs) can be tuned from 4-13 nm. Additionally, the study of these new materials expands the field of mesoporous silica material chemistry and facilitates a better understanding of interactions between organic molecules and silanes.

Compared to the conventional MSNs, the TA-TEOS NPs have several advantages. First, TA is inexpensive, nontoxic and abundant in nature, whereas other surfactants are expensive, toxic and difficult to synthesize. In biomedical applications, traces of toxic surfactant left in the particles are unacceptable. Second, the simple "one-pot" synthesis route of TA-TEOS NPs is suitable for large scale industrial production. Third, TA-TEOS NPs are the first kind of MSN that achieves uniform size/shape, small dimension (200 nm), and large pore size (13 nm)—at the same time making them excellent candidates for large molecule storage and drug delivery. Finally, the TA-TEOS NPs are capable of dual-modification in the interior of the pores and on the external surface. With TA acting as a protecting agent for the interior of the pores, the external surface of the TA SiNPs can undergo conventional silica surface modification. Since the TA template is removed using water, there is no need to subject the particles to calcination or harsh acid conditions, which are necessary to remove traditional surfactants. Therefore, the surface ligands remain on the particles after the removal of the TA molecules from the pores. Once TA is removed, the interior of the pores can be further modified.

3.2 Experimental

3.2.1 Chemicals and instruments

Tannic acid (ACS-grade, Alfa Aesar), tetraethoxysilane (TEOS, 99.999+%, Alfa Aesar), ammonium hydroxide (28-30% as NH_3, EMD Chemicals, Inc.), ethanol (200 proof, ACS-grade, Pharmaco-Aaper), 3-aminopropyltriethoxysilane (APTES, 99%,

Sigma-Aldrich), dansylchoride (Sigma-Aldrich), potassium phosphate monobasic (Sigma-Aldrich), potassium phosphate dibasic trihydrate (Mallinckrodt), sodium chloride (Mallinckrodt), sodium bicarbonate (Mallinckrodt), potassium chloride (Mallinckrodt), magnesium chloride (Aldrich), calcium chloride (Mallinckrodt), sodium sulphate (MACRON), sodium hydroxide (Mallinckrodt), Hydrogen Chloride (Sigma-Aldrich), tris(hydroxymethyl) aminomethane (Mallinckrodt), sodium silicate solution ($Na_2Si_3O_7$, 20% SiO_2, Mallinckrodt), ammonium molybdate tetrahydrate (Alfa Aesar), sulfuric acid (Fisher Scientific), oxalic acid dehydrates (Aldrich), L-ascorbic acid (Research Products International Corp.), lysozyme (from chicken egg white, Sigma-Aldrich), albumin (from bovine serum, lyophilized powder, Sigma-Aldrich), hemoglobin (from bovine blood, lyophilized powder, Sigma-Aldrich), β-Nicotinamide Adenine Dinucleotide Hydrate (β-NADH, Research Products International) and oxaloacetate acid (Sigma-Aldrich) were all used as received. Mitochondria Malic Dehydrogenase from porcine heart (ammonium sulfate suspension, Sigma-Aldrich) underwent dialysis in a 0.5-3 ml 3500MWCO dialysis cassette against phosphate buffer for 18 h at 4ºC. Acetonitrile (HPLC grade, VWR Scientific) was freshly distilled from calcium hydride. Millipore water (18 MΩ • cm) used in all experiments was obtained from a Barnstead "E-pure" water purification system.

The visual characterization was carried out by scanning electron microscopy (SEM, FEI NanoNova instrument) and transmission electron microscopy (TEM, FEI Philips Tecnai T-12 instrument). The surface area and pore volume were measured by nitrogen sorption measurements, which were collected on a Micrometrics ASAP 2010 (Norcross, GA) instrument at 77.3 K. All samples (~ 0.1 g) were degassed in the

degassing port of the adsorption apparatus at 80 °C for approximately 6 h prior to the nitrogen sorption measurements. The surface-area measurement was based on the Brunauer-Emmett-Teller (BET) method by using adsorption data at relative pressure from 0.05-0.20. The pore-size distribution was based on the Barrett-Joyner-Halenda (BJH) method. Philips type PW3040/00 XPert Pro XRD (Spectris, England) using Cu K α radiation at 45 kV and 40 mA was used to analyse the X-ray Diffraction (XRD) patterns of TA SiNPs. The XRD spectrum was recorded in the 2θ range of 1.8 – 10 with a step size of 0.02° in a 2θ scattering angle and a scan speed of 0.01 degree/s. UV/Vis measurements were performed using an Ocean Optics USB4000 instrument or a Thermo Scientific Evolution 260 B10. The particle hydrodynamic size and zeta-potential measurements were conducted in water using a NICOMP 380 ZLS Zeta Potential/Particle Sizer (PSS • NICOMP Particle Sizing Systems). Thermogravimetric analyses were performed using a TA Instruments TGA 2950 Thermogravimetric Analyzer. A Vortex-Genie 2 laboratory mixer from Scientific Industries was used to re-disperse the protein-loaded SiNPs in the solutions.

3.2.2 Preparation of tannic acid-templated mesoporous silica nanoparticles

Tannic acid (TA) was thoroughly dissolved in 50 mL ethanol. Twenty-five mL of concentrated ammonium hydroxide were added to the ethanolic solution under vigorous stirring following the addition of TEOS. Water from the concentrated ammonium was the source of trace water for the sol-gel hydrolysis reaction to occurring. The onset of turbidity after the addition of TEOS indicated the start of silica sphere formation. After 2 h of stirring, the particles were centrifuged out at 3400 rpm for 40 min and resuspended in water. The TA, and unreacted TEOS were removed by repeatedly washing with water

and ethanol until the supernatants were colorless. After the final rinsing, the particles were air-dried overnight.

3.2.3 Preparation of 240 nm silica spheres

The nonporous SiNPs was prepared by hydrolysis and condensation of TEOS according to the Stöber method,[17,18] which has been used as a model system to synthesize colloidal silica nanoparticles. 250.0 mL of an ethanolic solution containing TEOS (26.7 mL, 0.10 mol) and an equal volume of an ethanolic solution containing NH_4OH (13.4 mL, 0.20 mol) and water (144 mL, 8.0 mol) were mixed together and vigorously stirred at room temperature. After 24 h, the mixture was then centrifuged and washed in a gradient series water/ethanol solution. After the final rinsing, the supernatant was decanted, and the silica spheres were dried under ambient conditions.

3.2.4 Degradation study of TA-TEOS

All the solutions were contained in polyethylene bottles. Simulated blood fluid (SBF) was made by mixing the following components: 7.996 g NaCl, 0.350 g $NaHCO_3$, 0.224 g KCl, 0.228 g $K_2HPO_4 \cdot 3H_2O$, 0.305 g $MgCl_2 \cdot 6H2O$, 0.278 g $CaCl_2$, 0.071 g Na_2SO_4, 40 ml of 1 M HCl and 6.075 g of tris(hydroxymethyl) aminomethane with millipore water in a 1 L volumetric flask.[19]

Standard silicic acid solution was made by diluting the sodium silicate solution ($Na_2Si_3O_7$, 242.23 g/mol). Three stock solutions were prepared: 1) 3.1 g ammonium molybdate tetrahydrate dissolved in 50 mL 1M sulfuric acid. 2) 6.3 g oxalic acid dehydrates dissolved in 50 mL milipore water. 3) 1.76 g ascorbic acid dissolved in 50 mL millipore water. Sonication was used to help dissolve the salts. A calibration curve was made using the standard silicic solutions with concentrations of 1.72×10^{-5}M, $8.56 \times 10^{-}$

^{5}M, 1.703×10^{-4}M, 2.54×10^{-4}M, 3.37×10^{-4}M, and 4.195×10^{-4}M . 100 μL of solution 1 was added to 2 mL of the sample. After 10 min, the solution became yellow due to the formation of thephosphate molybdenum complex. A hundred μL of solution 2, which removes the interfering phosphate molybdenum complex, were then added and the yellow color faded in 1 min. The addition of 100 μL of solution 3 resulted in the blue color of the solution. The mixture sat for another 10 min to allow the completion of the blue complex formation. The wavelength of the blue molybdenum-complex peak is at 810 nm in UV-vis adsorption. By the UV-vis absorbance measurements, the concentration of silicic acid was obtained.

Ten mg of 240 nm Stöber SiNPs and TA-TEOS NPs were separately dispersed in 20 ml of millipore water or SBF. An aliquot of each solution was taken out and centrifuged hourly. A hundred μL of each supernatant were diluted by 2 ml of water or SBF, and the resulting solutions were tested by the aforementioned procedure.

3.2.5 Surface modification of tannic acid-templated mesoporous silica nanoparticles

To modify the surface of TA-TEOS with primary amine functionalities, 15 mg TA-TEOS NPs were redispersed in 10 ml freshly distilled acetonitrile by sonication. After the addition of 0.2 ml APTES, the solution was stirred under nitrogen flow overnight. The aminated particles were collected by centrifugation and washed extensively with distilled acetonitrile five times to remove the excess APTES. The amine modified TA-TEOS was dried in the air and stored in powder form.

3.2.6 Preliminary study of protein adsorption

Ten mM pH 6 phosphate buffer was prepared by mixing 0.136 g $K_2HPO_4 \cdot 3H_2O$ and 1.280 g KH_2PO_4 in 1 L milipore water.

Thirty mg of both Stöber SiNPs and TA-TEOS NPs were separately dispersed into 6.0 mL pH 6, 10 mM phosphate buffer (pH 6, 10 mM) and each colloidal solution was then divided into three 2 mL aliquots. Individual stock solutions (0.1 mM) of Lz, BSA and BHb were prepared in the same buffer and 2.0 mL of each were added separately to an aliquot of nonporous SiNPs and TA-TEOS NPs followed by incubation for 24 h at ambient conditions. The mixtures were centrifuged (40 min, 3200 rpm), and the UV/Vis absorbance was recorded for each of the supernatants.

The protein adsorption rate studies monitored the amount of protein adsorbed by TA-TEOS for 24 h in the phosphate buffer. 40 mg of TA-TEOS NPs were suspended in 8 mL phosphate buffer, then mixed with an additional 8 mL of 0.1 mM protein phosphate buffer solution. One and a half mL aliquots were periodically removed and centrifuged, and the supernatant was analyzed by UV spectroscopy.

The protein release from the loaded TA-TEOS was studied in phosphate buffer with 0.1 M of potassium chloride by redispersing 10 mg of protein-loaded TA-TEOS in 8 mL of phosphate buffer at room temperature by a vortex mixer. At each time interval, 1.5 mL of the solution were withdrawn, and the particles were isolated by centrifugation. The protein concentration in the supernatant was analyzed by UV-vis spectrophotometer.

3.2.7 Enzyme immobilization by TA-TEOS

The m-MDH was stored as an ammonium sulfate suspension at 4°C. Before all the experiments, the enzyme was transferred to phosphate buffer by dialysis (Slide-A-

Lyzer Dialysis Cassettes with 3.5K MWCO cutoff, Thermal Scientific) for 18 h at 4 ℃. The resulting enzyme solution was concentrated in a centrifuge filter by centrifugation, and the concentration was calculated using the calibration curve attained from the standard BSA assay.

A hundred mM phosphate buffer was prepared by mixing 15.223 g $K_2HPO_4 \cdot 3H_2O$ and 4.536 g KH_2PO_4 in 1 L millipore water and was adjusted to pH 7.5 with 12 M KOH solution.

Identical concentrations of particles (2.5 mg/mL) and enzymes (0.05 mM) as the previous protein immobilization experiment were used. Two hundred and forty nm Stöber method SiNPs were used as a nonporous reference. The particle suspensions and the m-MDH phosphate buffers were mixed together and followed by incubation for 24 h at ambient conditions. The mixtures were centrifuged (10 min, 12000 rpm), and the UV/Vis absorbance was recorded for each of the supernatants.

3.2.8 Enzyme activity test

A lower concentration of m-MDH phosphate buffer (100 mM, PH 7.5) was prepared. 5 mg/mL TA-TEOS and nonporous 240 nm SiNPs incubated in the m-MDH solution for 2 days at 4°C to allow the complete adsorption of m-MDH at low temperature. The m-MDH-loaded particles were separated from the enzyme stock solution via centrifugation for 40 min at 6000 rpm and 4 °C. The particles were redipersed in phosphate buffer by the vortex mixer for 10 min. The solution was then tested for its catalysis activity via a standard method described below. Two fresh stock solutions were prepared before each experiment: 1) 0.14 mM β-NADH phosphate buffer solution, 2) 7.6 mM oxaloacetate phosphate buffer solution. 1.4 mL of 1) was added to

the cuvette followed by the addition of 50 μL 2) and 50 μL sample solution. The mixture was shaken by hand and quickly put into the spectrometer. The reading of absorbance at 340 nm was recorded at 15 or 30 s intervals for 5 min. A free m-MDH solution with the same concentration of the enzyme as the ones loaded in the TA-TEOS was prepared. The catalysis activity was measured following the procedure previously described. Blank samples with phosphate buffer instead of the sample solution were also prepared and tested as references.

3.3 Results and discussion

3.3.1 Synthesis and characterization of TA-TEOS NPs

Surfactants such as CTAB, triblock copolymers and others are the usual pore-forming agents that self-assemble into micelles, creating the voids in the silica matrix during the preparation of mesoporous silica materials. The electrostatic interactions between the ionic surfactant and silicate species direct the formation of the mesoporous structure. For the non-ionic surfactants, the hydrogen bonding between the surfactants and the silicate is suggested to be the main driving force. There are a number of groups who produced mesoporous silica materials utilizing nonsurfactant templates. Wei *et al.* reported the synthesis of mesoporous silica materials achieved by NaOH and HCl catalyzed sol-gel methods through incorporation of dibenzoyl-L-tartaric acid, D-glucose and D-maltose into the silica frameworks.[20,21] The resulting materials have large surface areas, narrow pore size distribution (smaller than 4 nm), and disordered pore assembly upon the removal of the organic compounds.

In our study, TA is used as the pore-forming agent for the first time in the preparation of mesoporous silica nanoparticles by base-catalized hydrolysis of TEOS

(Sukhishvili *et al.* and Tsukruk *et al.* employed TA as a component in the hydrogen-bonded layer-by-layer films.[22,23]). TA is a polymer of gallic acid and glucose molecules with multiple hydroxyl groups which partially deprotonate in the basic condition (Figure 3.1). There are no reports about the self-assembly of TA. However, we assume that similar to the anionic surfactants, the negatively charged TA could have electrostatic interactions with ionic ammonium and silicic acid. In addition, although the sol-gel reaction took place under the basic conditions with a low acidity (pKa~10), not all the hydroxyl groups are deprotonated; as a result, they form H bonds between the TA and the soluble silicic acid species. We believe that the electrostatic and H-bonding interactions are the main driving force for the TA to form some supramolecular structure that imparts the formation of large voids in the silica framework.

One advantage of using TA is that it is a cheap and environmentally friendly pore-directing agent compared to the expensive and toxic surfactants used in other synthesis methods of mesoporous materials. As a natural molecule found in many plants, tannic acid is generally recognized as safe by the FDA to be used as a food additive.[24] It is also an effective antioxidant that is proven to be anti-mutagenic and anti-carcinogenic.[25-27] With its unique structure and properties, tannic acid also displays great potential in materials synthesis. Phillip et al.[28] and Zhang et al.[29] reported the synthesis of Au nanoplates and nanoparticles using tannic acid as both a reducing and a stabilizing agent. Xu *et al.* prepared a cross-linked chitosan/attapulgite composite resin by an emulsion method using TA as an imprinting template to enhance the adsorption of TA.[30]

Several batches of the TA-TEOS were prepared to optimize the synthesis variables. The concentration of the catalyst is a critical factor to the sol-gel reactions

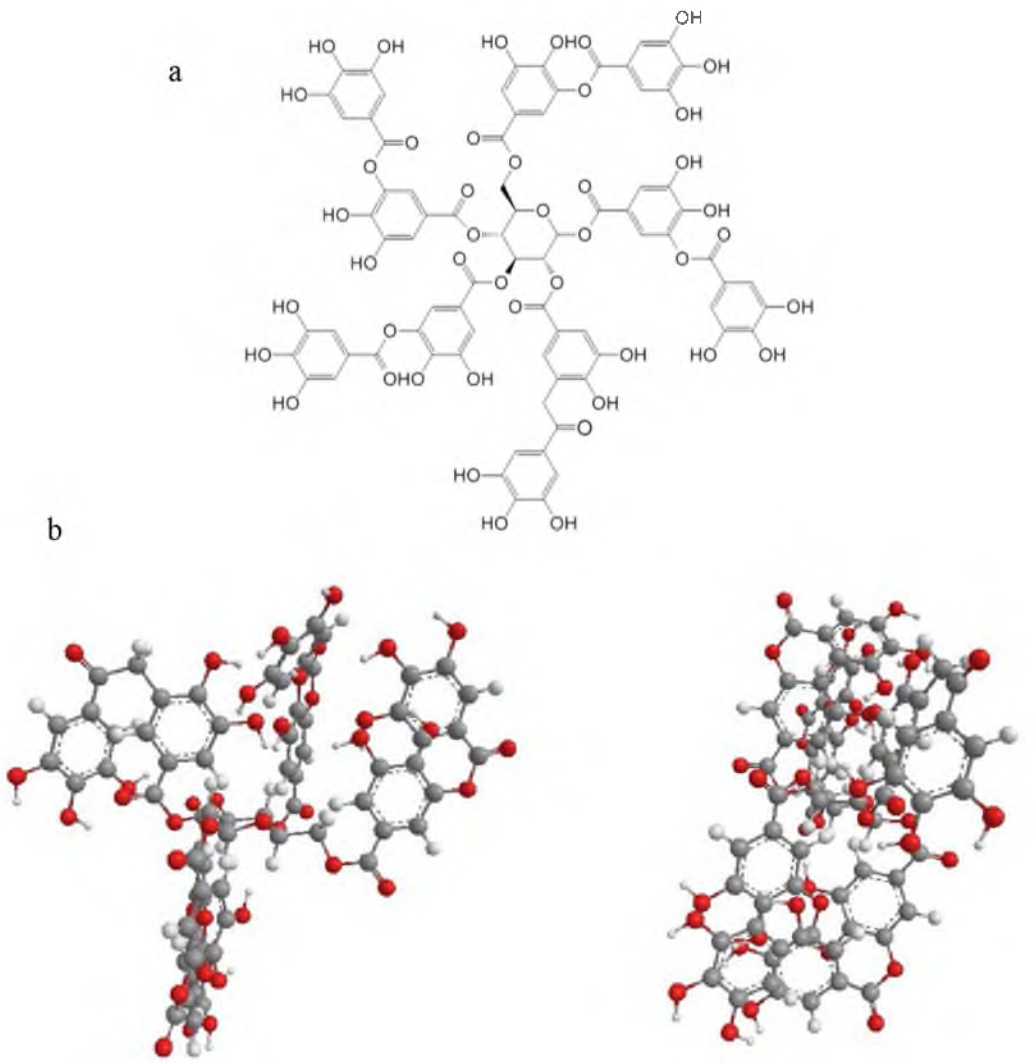

Figure 3.1. a) Tannic acid molecular structure. b) TA 3D structure in different directions.

because it affects the reaction rate and the morphology of the product.[31] Hydrolysis and polycondensation reaction rates accelerated with the increasing concentration of the catalyst. The higher concentration of ammonium hydroxide led to the formation of SiNPs with larger size. The ammonium hydroxide concentration was fixed at 1/3 of the total reaction solution volume in the synthesis of TA-TEOS for two reasons. The relatively high concentration of ammonium hydroxide quickly produced TA-TEOS. Moreover,

when the volume ratio of ammonium hydroxide added was less than 30%, turbidity appears. With further addition of ammonium hydroxide, the TA ethanolic solution became clear again with a red color (Figure 3.2).

The pore size of TA-TEOS was tuned from 5-13 nm by varying the TA concentration. TA4-TEOS, TA8-TEOS, TA16-TEOS and TA32-TEOS were prepared by adding 5.3×10^{-4} M, 10.6×10^{-4} M, 2.13×10^{-3} M, 4.26×10^{-3} M TA separately into each reaction solutions. The samples prepared from diverse TA concentrations were analyzed via TEM, SEM, and nitrogen adsorption-desorption measurements.

The size distribution and surface morphology were characterized by SEM. The SEM images demonstrate that the TA8-TEOS and TA16-TEOS particles were mostly spherical and monodisperse with negligible aggregation, and TA concentration had little influence of the sizes of the silica nanospheres. TA4-TEOS particles were less uniform, but presented a comparable average size with TA8-TEOS and TA16-TEOS. Due to their irregular shapes, TA32-TEOS exhibited agglomeration, and the average size of the TA32-TEOS particles was larger than the other samples.

Figure 3.2. The picture of TA-EtOH-NH_4OH mixtures. The sample on the right is TA-EtOH without addition of NH_4OH. With increasing amount of NH_4OH added to the solution the mixture became milky than clear red.

As shown by TEM (Figure 3.4), TA4-TEOS, TA8-TEOS, TA16-TEOS possess increasing porosity, similar to what was observed for most of the templated materials where the increase in the templating molecule concentration leads to a more porous structure. However, too much TA present in the reaction disturbs the formation of the spherical particles, and irregularly shaped, rough-surface solid agglomerates were obtained in the sample TA32-TEOS (Figure 3.3). High concentrations of template molecules preventing the pore formation were reported by other groups.[12]

The accurate measurement of TA-TEOS surface area and pore morphology is necessary to develop the applications of the particles in adsorption and separations. For the ordered mesoporous particles, which have cylindrical, close-packed pores, the porosity description is relatively straightforward and well-defined;[32] while in the case of the non-surfactant molecule templated particles, exploring the amorphous structure remains a challenge. Nitrogen sorption analysis can be used to characterize the surface area, pore size distribution, and other porosity related profiles. The sample is degased first to expel the adsorbed gases; it is placed in a vacuumed sample tube where the temperature is maintained at the cryogenic temperature, and exposed to nitrogen. With the increase of pressure, the nitrogen molecules are adsorbed on the surface of the particles and the pressure at each adsorption equilibrium state and the amount of nitrogen adsorbed is recorded. In the process of desorption, while the pressure is systematically reduced, pressure and the amount of nitrogen adsorbed are also recorded.

The Brunauer-Emmett-Teller (BET) surface area, pore volume and pore parameters listed in Table 3.1, confirm the presence of uniform pores, large surface area and pore volume for the particles prepared with relatively small amounts of TA. In

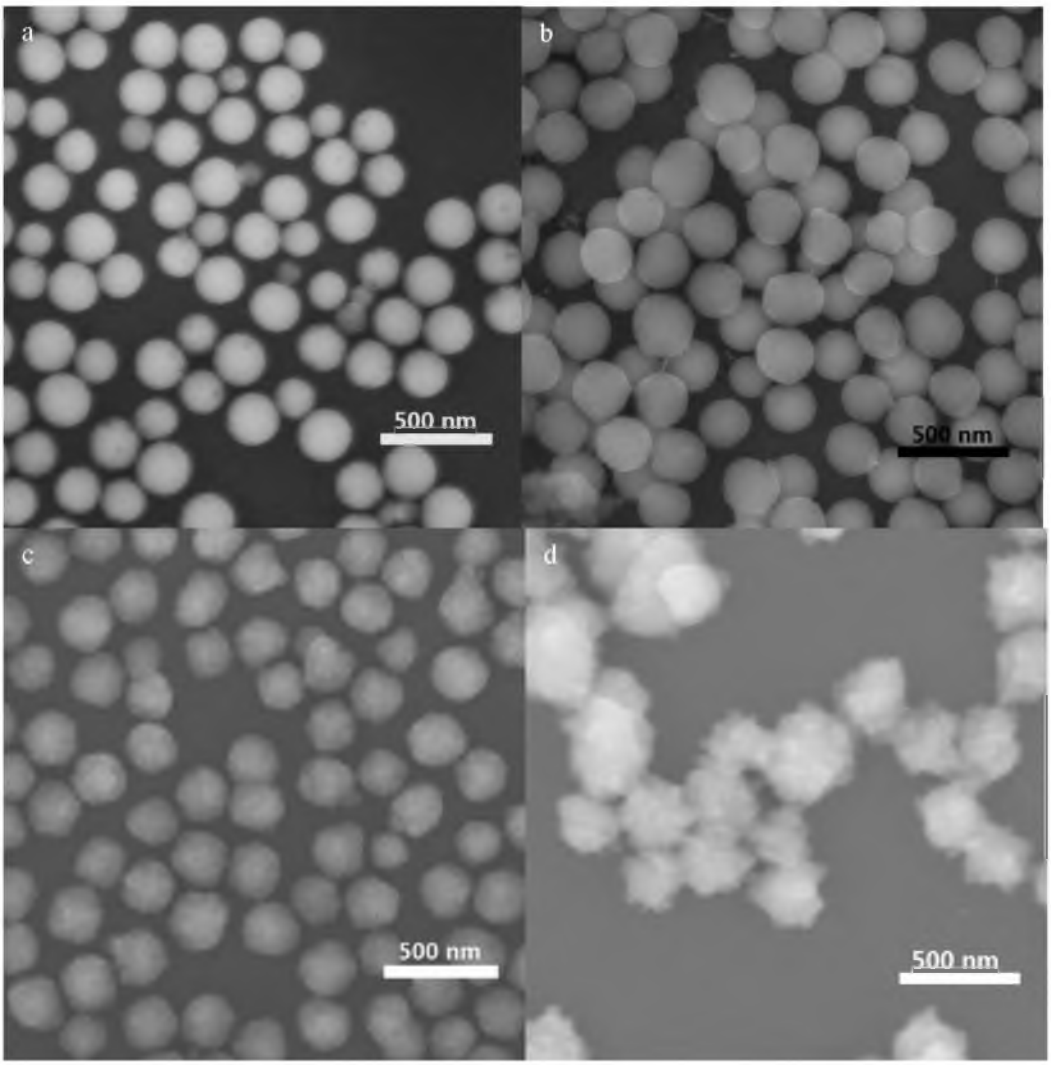

Figure 3.3. SEM images of tannic acid template silica nanoparticles produce with different amount of tannic acid: a) TA4-TEOS; b) TA8-TEOS; c) TA16-TEOS; d) TA32-TEOS.

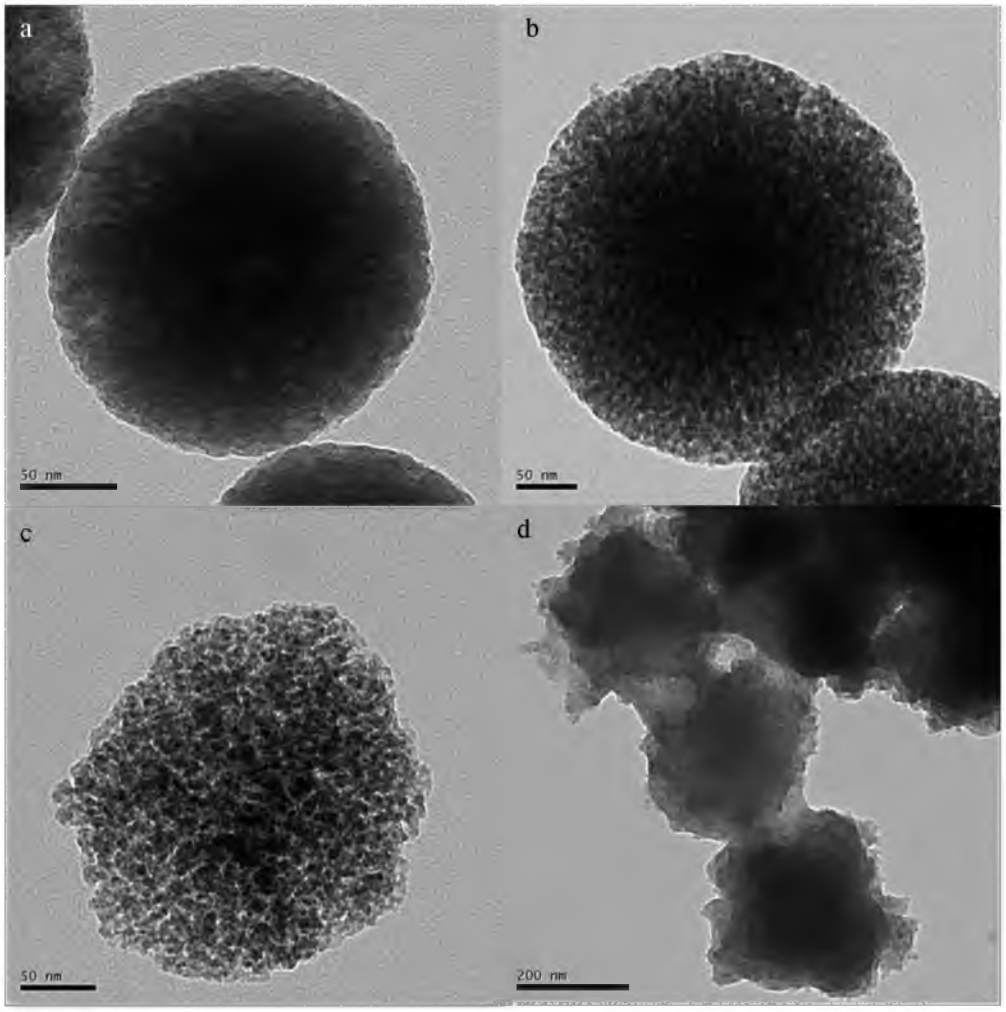

Figure 3.4. TEM images of tannic acid template silica nanoparticles produce with different amount of tannic acid: a) TA4-TEOS; b) TA8-TEOS; c) TA16-TEOS; d) TA32-TEOS.

general, an increase in the TA concentration in the template-containing solutions results in a larger surface area and pore volume. The nitrogen sorption measurements show type IV isotherms for the TA4-TEOS, TA8-TEOS and TA16-TEOS with two distinct adsorption steps, which are characteristic of a mesoporous structure (Figure 3.5).[33] The small hysteresis loops around 0.3 p/p_0, 0.5 p/p_0, and 0.7 p/p_0 correspond to the pore size distribution centered at 6, 10 and 13 nm, respectively (Figure 3.5). The hysteresis loop at

Table 3.1. The textural parameters of TA-TEOS from the N_2 sorption measurements

Sample	BET Surface Area (m^2/g)	Pore Volume (cm^3/g)	Pore Size (nm)[a]
TA4-TEOS	419.9	0.46	5.9
TA8-TEOS	445.4	0.82	9.7
TA16-TEOS	560.6	1.53	12.9
TA32-TEOS	9.4	0.12	---

a) BJH Adsorption average pore width

higher relative pressure (about 0.9) can be attributed to inter-particle porosity. In the case of TA32-TEOS, the N_2 sorption isotherm shows a type II isotherm characteristic of macroporous material (>50 nm) with only one hysteresis loop at higher pressure due to the agglomeration of the particles. The BET surface area of TA32-TEOS is 9.4 m^2/g, which is comparable to nonporous silica nanoparticles.

We also studied the influence of the reaction time on the nanoparticle morphology. The SEM and TEM images of the products of the 2, 6, and 24 h reactions (TA-TEOS-2h, TA-TEOS-6h, TA-TEOS-24h) are shown in Figure 3.6. All of the reactions produced monodisperse nanoparticles with rough surfaces. However, only TA-TEOS-2h and TA-TEOS-6h displayed a porous structure, while nonporous structure was observed for TA-TEOS-24h particles. The core of TA-TEOS-24h had high density so that the TEM could not confirm the inner structure of these samples. In order to better understand the formation of the TA-TEOS at different reaction times, TGA was conducted to analyse TA-TEOS-2h, TA-TEOS-6h, TA-TEOS-24h samples. The weight loss in the temperature

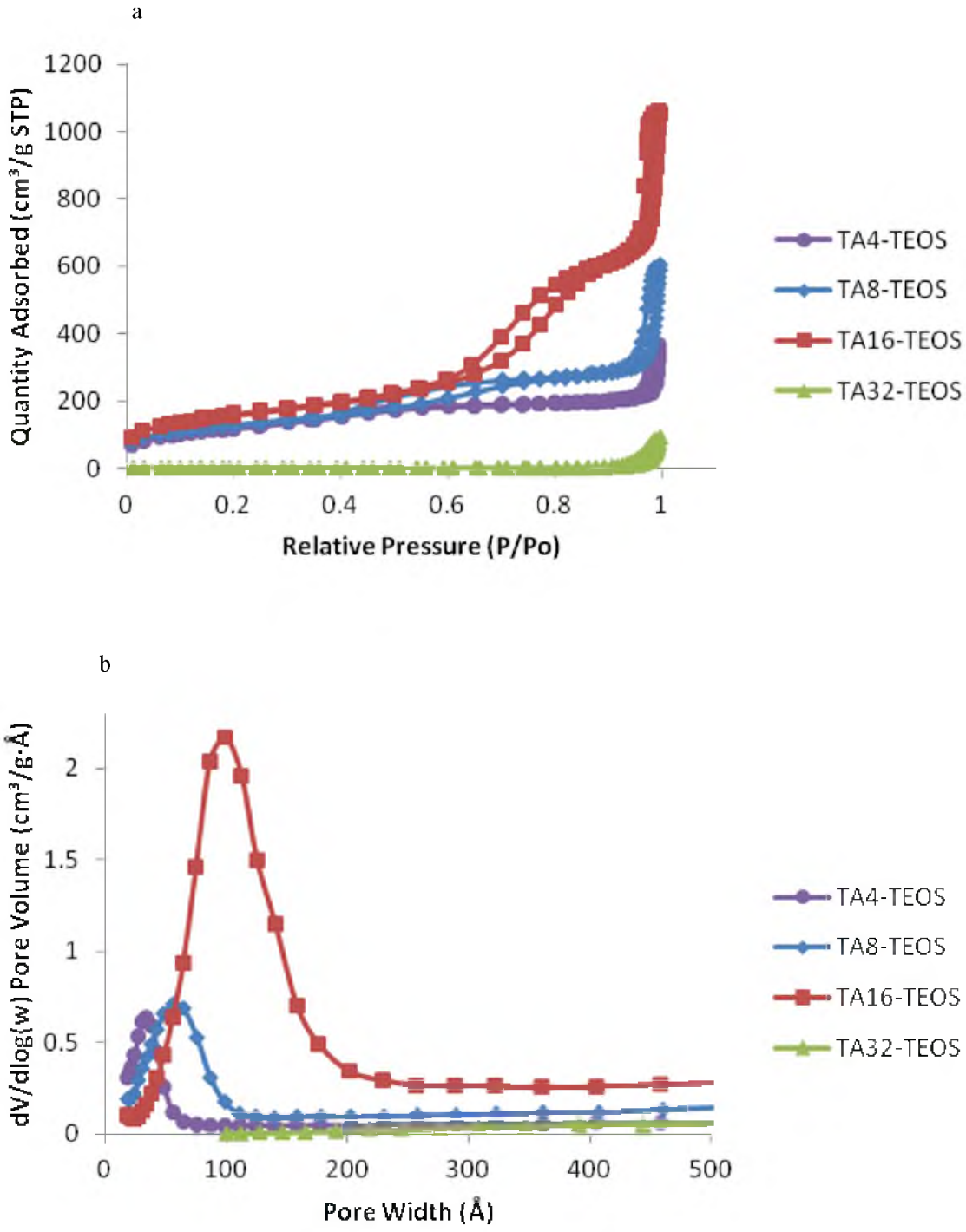

Figure. 3.5. a) Nitrogen adsorption–desorption isotherms and b) pore size distribution curves.

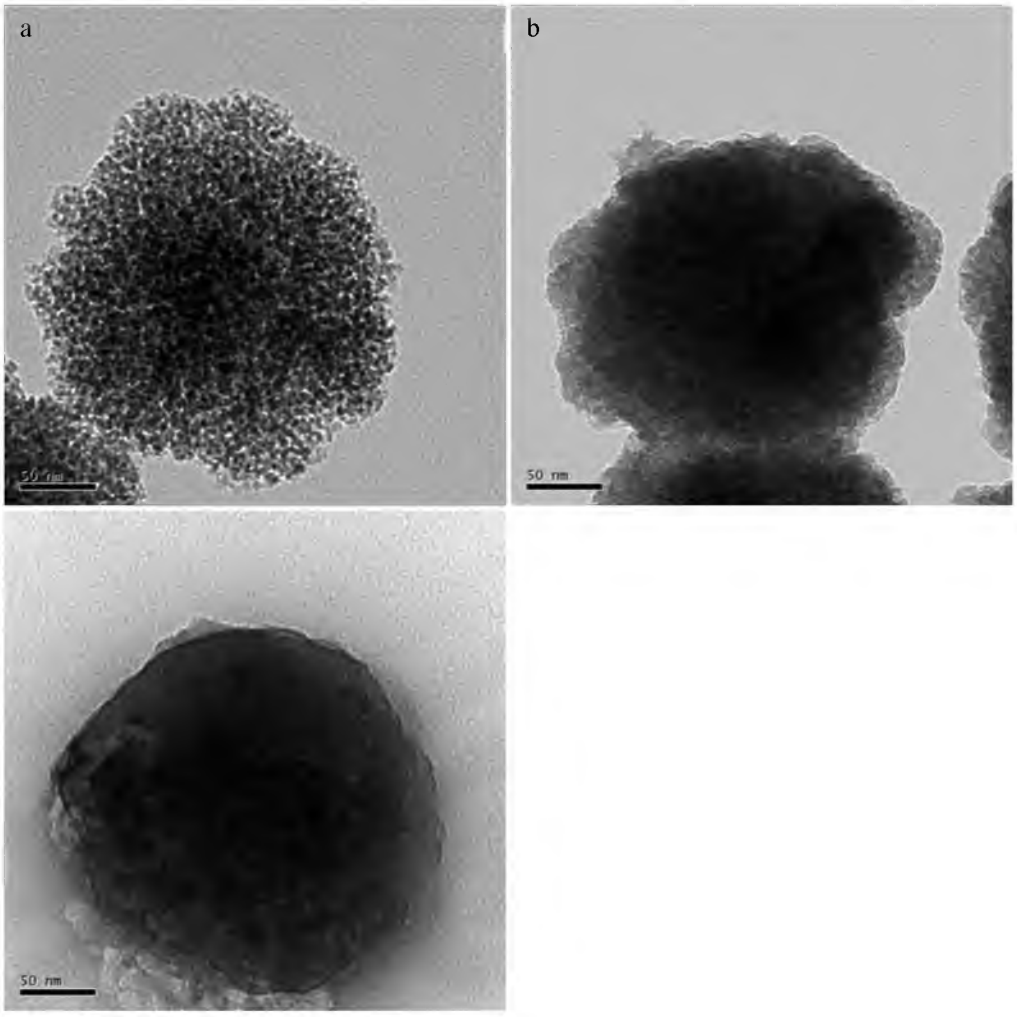

Figure. 3.6. TEM images of tannic acid template silica nanoparticles produced in different reaction times: a) 2 h; b) 6 h; c) 24 h.

ranging from 35 to 200 °C was mostly attributed to the degradation of silanol groups, and the weight loss above 200 °C was due to the calcination of TA (Figure 3.7). According to the TGA analysis, TA-TEOS-24h had a larger weight loss in the higher temperature range compared to the other two samples. The difference of weight loss suggests that TA-TEOS-24h contains more TA. A possible explanation for this is that TA formed a supramolecular structure with TEOS by the hydrogen bonding at the beginning of the reaction; after 2 h, the excess TEOS molecules entered the interior of the particles and continued to condense in the pores and on the external surface of the particles to form a silica shell, which eventually blocked the pores completely. Because of the blocking of the pores, TA could not be removed by water extraction; it remained inside the particles, which was detected by TGA analysis. Moreover, the ashes of TA-TEOS-2h and TA-TEOS 6h displayed a blue color after the calcination due to the carbonization of the TA residues. At the same time, because the TA was trapped inside the TA-TEOS-24h particles, the color of the ash of TA-TEOS-24h remained white.

The ashes obtained after the TGA measurements were analysed by SEM. According to the SEM images, calcination at 800 °C did not induce the collapse of the TA16-TEOS, indicating these TA16-TEOS SiNPs have thick silica walls and high thermal stability. However, in the case of the TA32-TEOS SiNPs, the irregularly shaped particles fused together after the calcination.

As seen in the TEM images, the contrast of the TA-TEOS SiNPs at the center is low due to the disordered pore arrangement. The XRD spectra of TA-TEOS SiNPs did not display any specific peak, which further illustrates the lack of the pore order of the

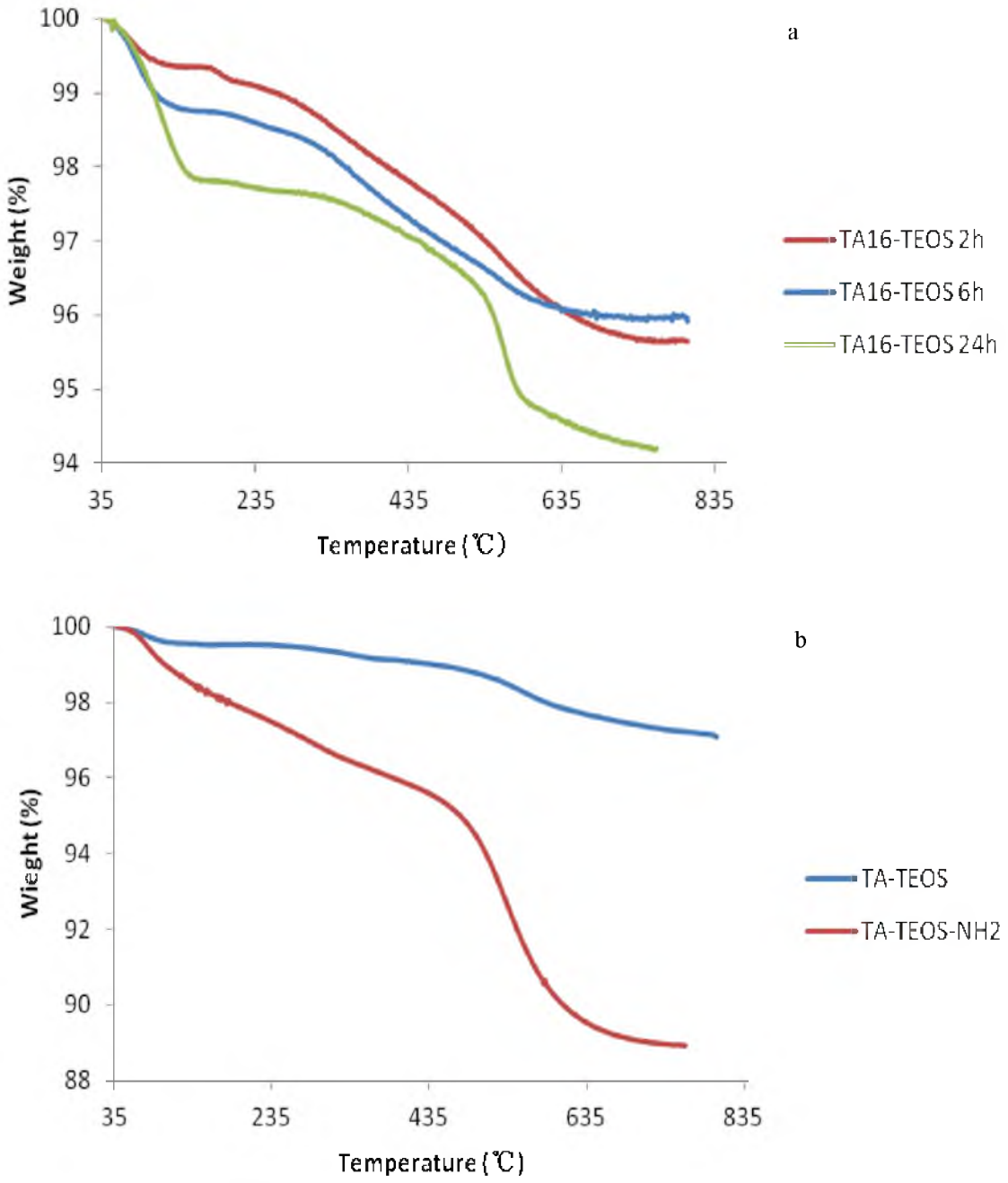

Figure 3.7. TGA data of tannic acid template silica nanoparticles: a) produce by different reaction times; b) modified with amine groups.

TA-TEOS particles. In contrast, the well-ordered hexagonal or cubic arrangements of the pores in periodic mesoporous silica materials give diffraction patterns in powder X-raydiffraction experiments. The disordered arrangement in our particles likely resulted from the inability of TA to form regular micelles with well-defined geometries. In addition, the fast condensation generally leads to a less condensed and less ordered silica framework.[17]

All our later experiments used the TA16-TEOS-2h particles which had large pore sizes. In addition to electron microscopy, the hydrodynamic size and water dispersibility of TA-TEOS were measured by DLS. According to DLS, the TA16-TEOS particles have an average hydrodynamic diameter of 249.2±60.5 nm. Due to the shrinkage during the electron microscopy experiments, the sizes of the TA16-TEOS particles obtained by SEM were smaller than those measured by DLS (193.6 ± 14.2 nm). Zeta potential measurements showed that TA-TEOS nanoparticles were highly negatively charged (-37.8±3.5 mV), indicating a fairly stable suspension in aqueous medium, and resistance to aggregation due to the electrostatic repulsions.

3.3.2 Degradability of TA-TEOS NPs

Although the degradation of silica is fairly slow, mesoporous SiNPs with higher surface area have more interaction with water which increases the degradation rate of the material. [34] Moreover, disordered structures are more vulnerable to dissolution.[35] Herein, we describe our preliminarily studies of the degradation behavior of TA-TEOS NPs in water and in simulated blood fluid (SBF).

The degradation rate of TA-TEOS NPs was monitored through the well-established molybdenum blue colorimetric method, which has been used to detect the

trace concentrations of monosilicic acids. The molybdenum ions react with monosilicic acid and reveal a blue color due to the formation of siliconmolydbate complex. [36,37] TA-TEOS SiNPs and 240 nm SiNPs synthesized by the Stöber method were dispersed in millipore water and SBF. An aliquot of each suspension was taken out and centrifuged hourly in the first 5 h, and then every 24 h. The supernatants were measured by the molybdenum blue method. The molybdenum blue test detected the releasing of silicic acid in 3 days, which showed the degradation behaviors of different SiNPs (Figure 3.8). When immersed in water, the TA-TEOS NPs showed a constant degradation rate. The Stöber particles were barely degradable in water. They exhibited a faster degradation rate in SBF; but after 48 h, the degradation rate slowed down and the silicic acid concentration eventually remained constant. The degradation rates in water were slower than in SBF because calcium and magnesium ions in SBF affect the degradation behavior of silica. [38,39] TA-TEOS NPs showed a faster degradation rate compared to the Stöber particles in both solvents. TA-TEOS NPs degraded quickly during the first 8 hours in SBF, then the degradation slowed down; this is similar to the degradation behavior of MCM-41 nanoparticles reported by the Chen group,[40] who reported that the degradation of MSNs proceeds in different stages: fast bulk degradation in the first several hours, and a decelerated degradation blocked by the formation of calcium and magnesium silicate layer on a day-scale.

The morphology changes of TA-TEOS NPs induced by degradation were observed by SEM and TEM as shown in Figure 3.9. The pore openings became larger and detectable by SEM after the TA-TEOS NPs were immersed in water for a month. Continuous wrinkled structures were found on the TA-TEOS NPs that were immersed in

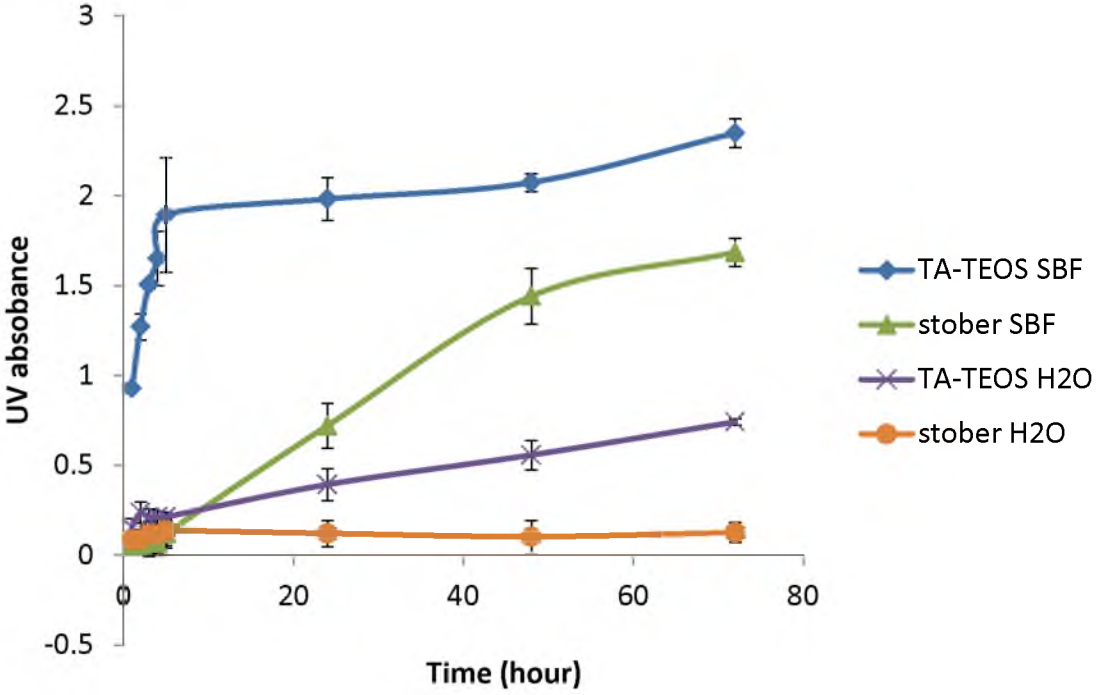

Figure 3.8. Silicic acid released by TA-TEOS and Stöber SiNPs in water and SBF.

SBF for one day. Moreover, the particles that were immersed in SBF for a month became flower-like in shape. The slow degradation of TA-TEOS with larger diameter of pore openings suggests future application of the particles as drug delivery agents, which could slowly release the guest molecules.

3.3.3 Surface modification of TA-TEOS

Removal of the template by solvent extraction from TA-TEOS nanoparticles exposes silanols on the external surface and inside the pores, which can be silylated.[41] A variety of functional groups such as amine, thiol and carboxyl groups can be attached to the silica nanoparticles, facilitating further conjugation with various guest species such as imaging dyes or targeting ligands.

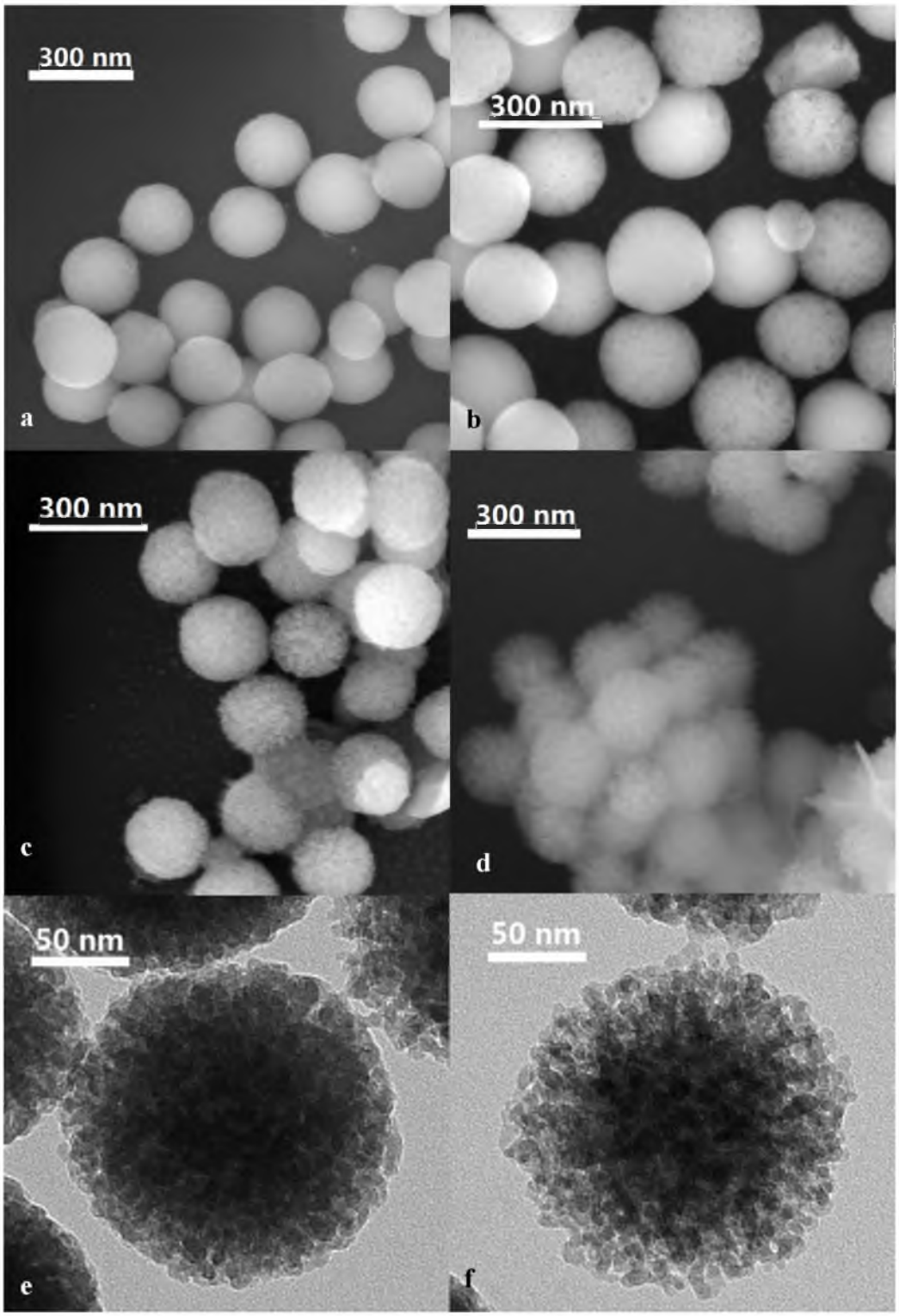

Figure 3.9. SEM images of TA-TEOS a) as made; b) in water (pH7) for a month; c) in SBF for a day; d) in SBF for a month. TEM images of TA-TEOS e) in milipore water for a month f) in SBF for a day.

The amination procedure of Stöber SiNPs was also applicable to the TA-TEOS particles. Herein, we used one of the most commonly used silane-coupling agents, 3-aminopropyltriethoxysilane (APTES) to attach primary amine groups onto the outer- and inner-surfaces of the porous silica particles. The characterization of amine modified TA-TEOS particles (NH_2-TA-TEOS) was done by using colorimetric method, TGA and zeta potential measurements. The fluorescence generated by the reaction between dansyl chloride and primary amines is a simple qualitative method to test the presence of primary amines. After the addition of two drops of dansyl chloride, ethanolic solutions of NH_2-TA-TEOS glowed under UV irradiation; the unmodified TA-TEOS solutions did not fluoresce at all (Figure 3.10). The quantitative measurement of amine coverage on the TA-TEOS particles was achieved through TGA, where a significantly larger weight loss of the NH_2-TA-TEOS compared to TA-TEOS was measured. As shown in Figure 3.6, the TGA of NH_2-TA-TEOS under N_2 displayed 1.7% weight loss from 35 to 200 °C for dehydration of silanols in the silica structures, and 9.5% weight loss from 200 to 800 °C for the decomposition of the amines. Using the TA-TEOS surface area of 560 m^2/g, and assuming that the amine groups were evenly distributed both onto the external and internal surfaces, the surface coverage is estimated to be about 1 amine per nm^2. This reasonable coverage density suggests successful attachment of the amine groups both onto the external surface and into the pores. This should allow functional moieties to be attached inside the pores of TA-TEOS particles, which would efficiently protect them from the outside environment. In addition to the TGA results, the zeta potential of the NH_2-TA-TEOS, which was 18.2 ± 0.6 mV, demonstrated the presence of positively charged amine groups on the particles.

Figure 3.10. Left vial contained TA-TEOS and right vial contained NH_2-TA-TEOS, both in the presence of dansyl chloride under UV light.

3.3.4 Preliminary study of physical adsorption of proteins

In the past decade, mesoporous silica materials with large pore diameter attracted attention to be used as adsorbents for various biomolecules.[42-44] Immobilizing proteins inside the nanopores not only protects them from the environment and increases the stability of proteins to heat, pH and chemicals, but also has the possibility of enhancing the bioactivity of the proteins whose structure would be confined in the restricted pore space.[45,46] However, the one-dimensional channel system of periodic mesoporous silica particles do not have interconnecting pores with each other, rendering them ineffective as carriers for biomolecule loading.[47] One objective of this work was to investigate the possible application of TA-TEOS particles as protein carriers. Since the pore morphology of nanopaticles is considered to be one of the key conditions causing different

efficiencies of biomolecule uptake, the study of protein adsorption by the TA-TEOS nanoparticles, which have unique pore structures, would broaden our knowledge with respect to biomolecule adsorption by porous materials.

It is known that protein adsorption is strongly influenced by the relative sizes of the proteins and nanopores,[48] the pH of the solution,[49] and the surface characteristics of the porous materials and the proteins. Since TA-TEOS particles were purified by solvent extraction, there are abundant silanol (Si-OH) groups on the surface of the particles. The TA-TEOS surfaces possess a negative charge of -37.8±3.5 mV in water, and a slightly less negative charge of -25.5±3.6 mV in 10 mM PBS (pH 6) (Table 3.2), because of the salt effect. The major driving forces of protein adsorption by silica materials are electrostatic interactions[50] and hydrogen bonding[51] between the silanol groups and the carboxylic or amino groups in the protein molecules.[52] Lysozyme (Lz),[52, 53] bovine hemoglobin (BHb)[54] and bovine serum albumin (BSA)[52, 55] were chosen as model proteins in this work for their relatively smaller dimensions compared to the size of the mesopores of TA-TEOS particles, varied isoelectric points as listed in Table 3.3, and the large amount of information available in literature. The concentration of the proteins was measure using UV/Vis analysis (Figure 3.11). The equilibrium adsorption capacities and kinetic characteristics of the three probe proteins on the TA-TEOS were studied.

Nonporous silica nanoparticles with an average diameter of 244.8±13.8 nm were synthesized by the Stöber method and served as a reference. The three proteins were adsorbed more significantly by the porous TA-TEOS NPs compared to the Stöber particles due to the greater surface area, as well as larger amounts of silanol groups of TA-TEOS (Table 3.4). In addition, the significant increase in the protein adsorption by

Table 3.2. Zeta Potential of particles in water, phosphate buffer and KCl, phosphate buffer solution.

	Zeta Potential (H_2O, mV)	**Zeta Potential (10mMPBS, mV)**	**Zeta Potential (10mMPBS + 0.1M KCl, mV)**
TA-TEOS	37.8±3.5	-25.5±3.6	-1.4±0.3
Stöber SiNPs	49.9±0.0	-49.2±0.2	-4.0±0.3
Lz	-	10.0±0.3	1.5±1.2
BHb	-	12.7±0.3	-0.7±0.3
BSA	-	-13.6±0.1	-2.0±0.2

Table 3.3. Properties of the proteins selected in this study [52-55]

	lysozyme	**bovine hemoglobin**	**bovine serum albumin**
Dimensions (nm)	3.2	6.4 × 5.5 ×5	4 × 4 × 14
pI	11.4	7.4	4.8
Mass (KDa)	14	64	67
λ_{max} Abs (nm)	280	499	277

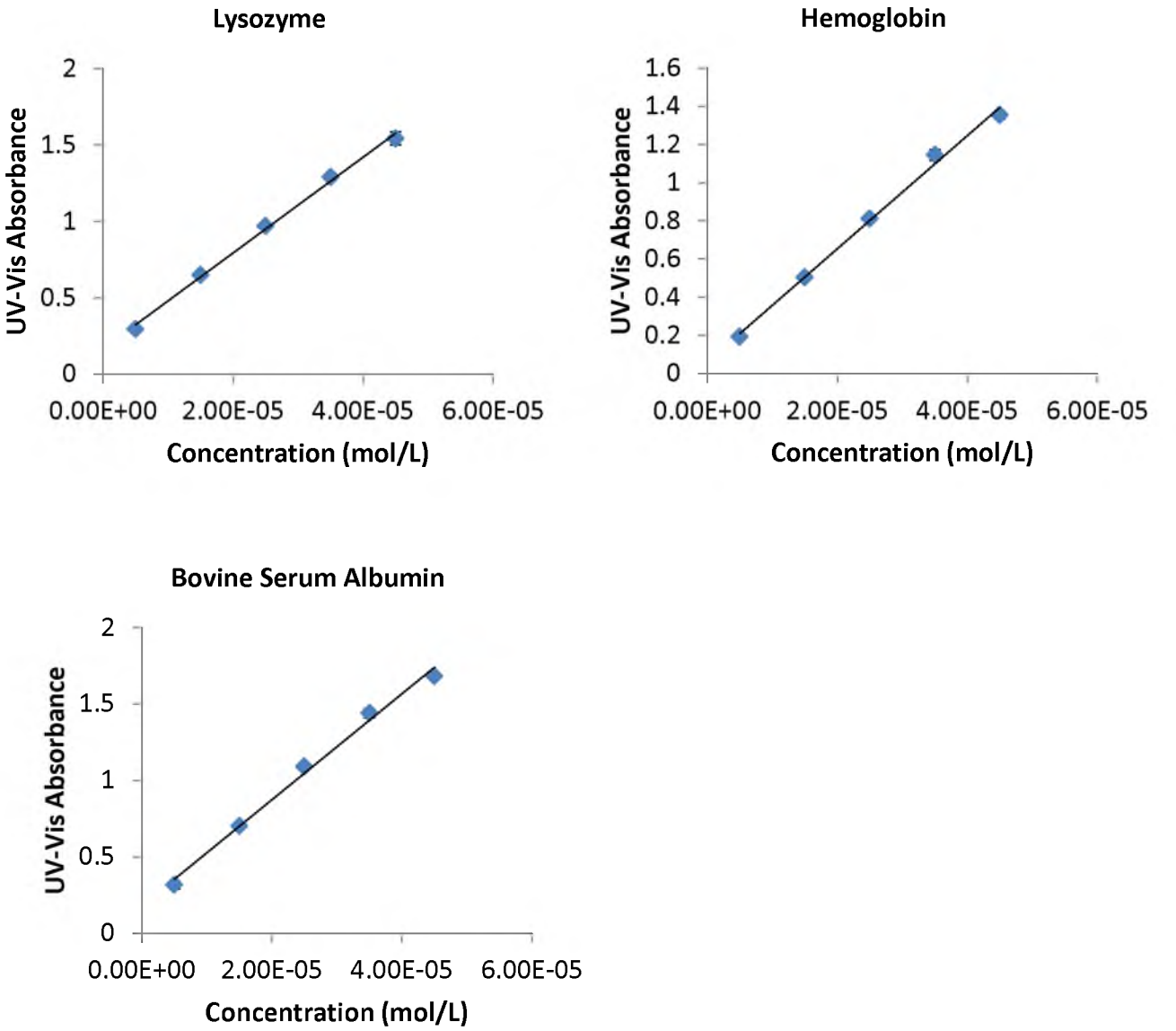

Figure 3.11. Calibration curves of lysozyme, bovine hemoglobin, bovine serum albumin.

Table 3.4. The summary of protein adsorption by TA-TEOS and nonporous SiNPs

	Initial Conc. (mM)	TA-TEOS NPs Adsorption %	TA-TEOS NPs Adsorption (mg/g TA-TEOS)	Nonporous SiNPs Adsorption %	Nonporous SiNPs Adsorption (mg/g SiNPs)
Lz	0.05	27.5±4.4	77.1±12.4	1.2±1.4	3.3±3.9
BHb	0.05	31.0±2.8	396.5±35.8	21.3±2.4	272.7±30.9
BSA	0.05	9.7±3.1	130.0±41.4	0	0.5±0.9
Lz-KCl	0.05	11.2±1.4	31.3±3.9	0	0
BHb-KCl	0.05	23.8±2.6	304.5±33.7	8.5±1.7	109.2±22.3
BSA-KCl	0.05	2.4±3.1	32.2±40.9	0.6±0.6	8.2±7.4

the TA-TEOS illustrated that the proteins were not only adsorbed on the external surface of the particles, but also immobilized inside the mesopores. The positively charged lysozyme and hemoglobin possessed a greater affinity to the TA-TEOS NPs compared to the negatively charged BSA. Although the nonporous silica NPs absorbed a negligible amount of BSA, TA-TEOS trapped a noticeable amount of this negatively charged protein via hydrogen bonding (Table 3.4). Here the pore size was a key factor that strongly influenced protein capacity and uptake rate because the diffusion rate is geometry-dependent,[56] and a relatively wide pore opening allows protein molecules to enter the pores of the particles with less resistance.[57] In addition, the large volume of the mesopores ensured the abundant adsorption capacity of proteins. The different adsorption of proteins by TA-TEOS NPs created potential application of TA-TEOS NPs in protein separation.

The kinetic plots of the proteins adsorbed by the TA-TEOS are shown in Figure 3.12. Because of the large pore openings, the protein adsorption rate of TA-TEOS particles is faster than the MCM-41 and SBA particles,[52, 58] which make TA-TEOS particles more efficient protein adsorbents. The smallest protein, lysozyme, reached its saturation in 3 h, while the larger proteins, BHb and BSA, reached their saturation points in 6 and 8 h. The different adsorption rates could also make the TA-TEOS a potential material for protein separation.

To confirm that the hydrogen bonding played a crucial role in the adsorption of proteins, salts were added to the protein solution to screen electrostatic interactions. In 0.1 M KCl solution, zeta-potentials of silica particles and of the proteins were close to zero (Table 3.3). Table 3.4 shows a decrease in adsorption for all proteins under these

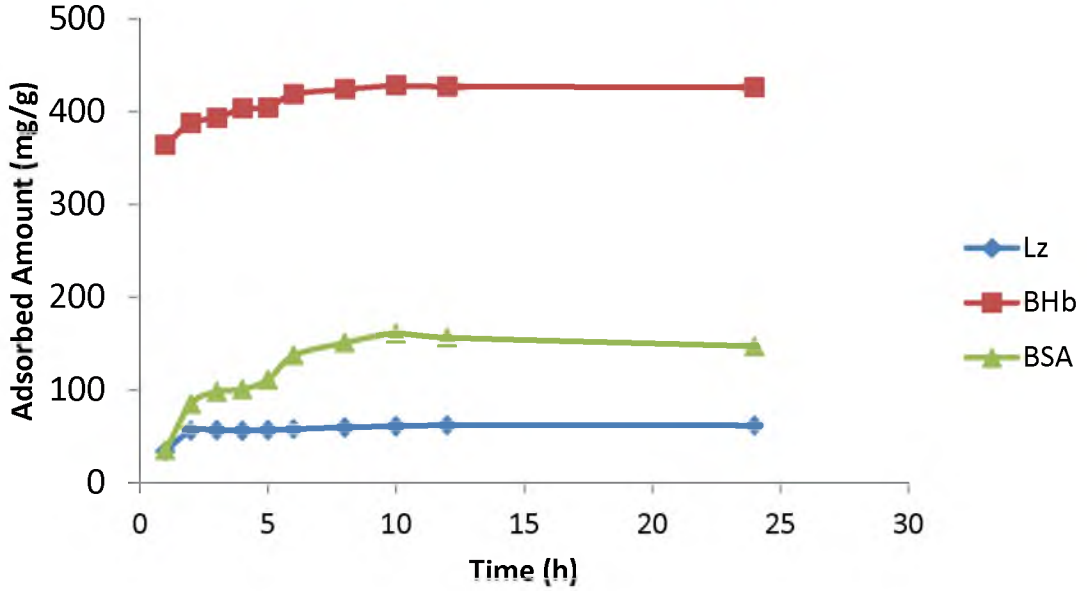

Figure 3.12. Adsorption kinetics of TA-TEOS particles.

conditions. However, the fact that a significant amount of proteins, in particular BHb, was still uptaken by the TA-TEOS in the presence of KCl illustrated that hydrogen bonding played a central role in the protein adsorption by TA-TEOS NPs (Table 3.4).

Since the adsorption capacities of the particles were affected by the ionic strength of the solution, we hypothesized that proteins initially loaded under lower ionic strength condition could be released under higher ionic strength conditions. The particles loaded with proteins in 10 mM phosphate buffer were redispersed in 8 mL 10 mM phosphate buffer in the presence of 0.1 M KCl by votex. One and a half mL of each sample was taken out in the time intervals of 1, 3, 5, 7 and 24 h, and the supernatants were obtained by centrifuging the particles. The UV absorbance of the supernatants allowed measuring the amount of the protein released from the particles. Figure 3.13 shows that the

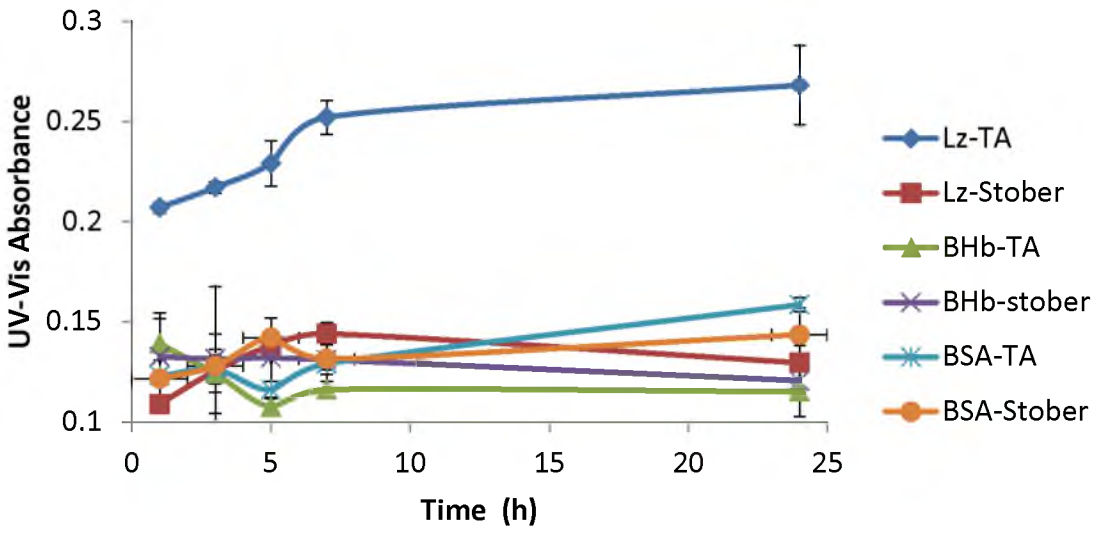

Figure 3.13. Protein-releasing kinetics of TA-TEOS and nonporous SiNPs.

adsorption of larger proteins on TA-TEOS appeared to be irreversible; meanwhile the small globular protein, lysozyme, with its low molecular weight, was slightly released by the TA-TEOS particles. None of the other proteins desorbed from the solid silica particles. The intensities below 0.15 were induced by the light scattering from the SiNP residues that were not completely removed by the centrifugation.

3.3.5 Immobilization of mitochondrial malic dehydrogenase

Immobilized proteins, such as enzymes and antibodies, are useful in catalysis, sensors, and separation applications due to their potential to improve the stability and activity under extreme conditions[59] Malic Dehydrogenase (dimentions = 6.4 × 6.4 ×4.5 nm, isoelectric point = 8.0-8.5[60]) is an enzyme found in animals. This protein contains two identical subunits with a combined molecular weight of 70K Da. Eukaryotic cells contain two different types of malate dehydrogenase: mitochondrial (m-MDH) and soluble or cytoplasmic (s-MDH). In our work, we used mitochondrial Malic

Dehydrogenase from porcine heart (m-MDH) to study the catalytic activity of immobilized enzymes. The reason for choosing this enzyme is that it is relatively cheap; it participates in many biological cycles; the detection of its catalytic behaviour is simple and straightforward; and abundant knowledge is available in literature. Furthermore, m-MDH has similar molecule weight, dimensions and isoelectric point to BHb, which we successfully immobilized in TA-TEOS NPs, as discussed in the previous section. Thus, we expected that m-MDH would be adsorbed into the pores of the TA-TEOS.

We studied the adsorption of m-MDH by TA-TEOS SiNPs using the same conditions as in the protein adsorption experiments above. The nonporous Stöber particles with the diameter of 240 nm were used as a reference. The adsorption data is shown in Table 3.5. The adsorbed amount of m-MDH by TA-TEOS NPs was double the amount of enzyme that was adsorbed by nonporous SiNPs, indicating that the enzymes were immobilized not only on the external surface of the TA-TEOS NPs, but also inside the pores (Table 3.5). Moreover, the fact that adsorption behavior of m-MDH was

Table 3.5 The m-MDH adsorption by TA-TEOS and nonporous SiNPs

	TA-TEOS	**Stöber SiNPs**
Initial Conc. (mM)	0.05	0.05
m-MDH Adsorption %	31.4±1.0	15.9±1.4
m-MDH Adsorption (mg/g)	420.7±12.9	213.6±18.8

comparable with BHb (Table 3.2) indicates that proteins possessing comparable size, weight and surface charge show similar adsorption capacity on the SiNPs, which is not significantly affected by the primary and secondary structures of the biomolecules (eg. the amino acid sequence).

Our earlier adsorption experiments were conducted at room temperature, which may cause the denaturation of the enzymes. To test the m-MDH catalytic activity, the adsorption took place in the refrigerator, where the temperature was maintained at 4 ºC. Since it is known that the diffusion rate depends on temperature, we incubated the particles with the enzyme at 4 ºC for a longer time period, 2 days, to ensure the completion of the maximum adsorption of m-MDH. The concentration of the enzyme solution was lower than in the protein adsorption capacity experiments because high enzyme concentrations led to faster catalysis, which could not be recorded by the UV-vis spectroscopy. The resulting solutions were centrifuged at 4 °C and the particles loaded with m-MDH were redispersed in phosphate buffer. The catalytic reaction of m-MDH (Figure 3.14) took place at pH 7.5 and at room temperature to maximize the activity of m-MDH. By measuring the UV-Vis absorbance of β-NADH at the wavelength of 340 nm, which indicated the converting amount of oxaloacetic acid into maleic acid, we obtained the activity of the enzymes immobilized on the TA-TEOS and on nonporous SiNPs. A solution of free enzymes with the same concentration as the enzymes that were adsorbed by the TA-TEOS particles was prepared as a reference. Both of the immobilized m-MDH and free m-MDH solution were diluted a 100 fold due to the fast reaction rate.

Figure 3.15 shows the change of β-NADH concentration as a function of time. The slopes of the plots represented the conversion rates of the β-NADH and the catalytic

Figure 3.14. The reversible conversion reaction of oxaloacetate to L-Malate catalysed by m-MDH.

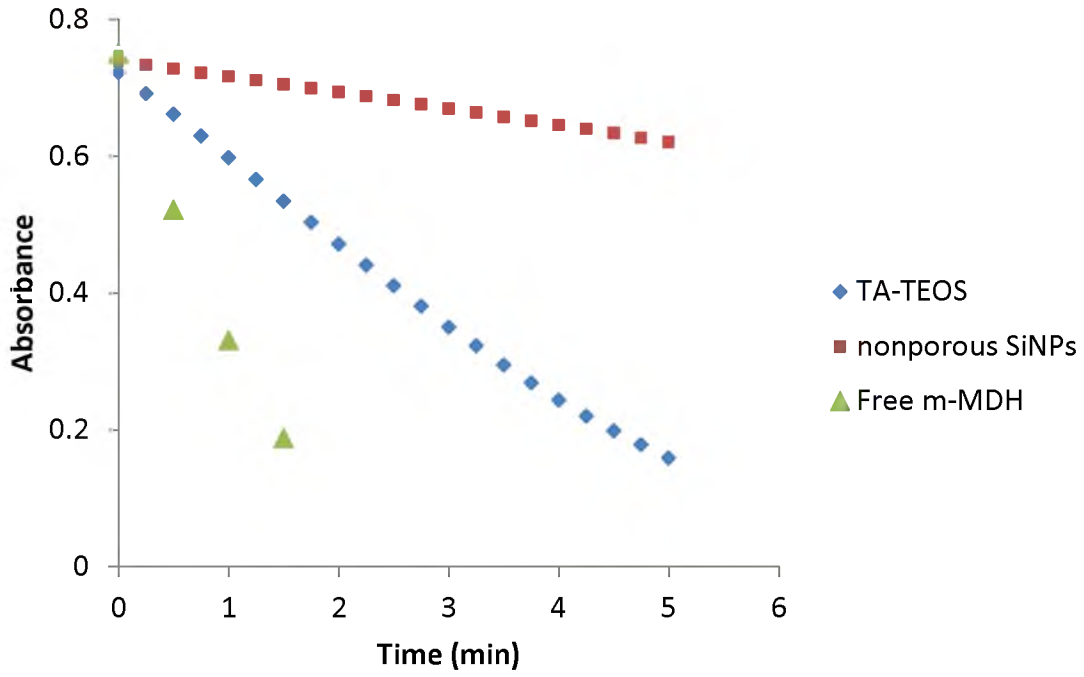

Figure 3.15. Catalysis activities of m-MDH immobilized in TA-TEOS and nonporous SiNPs and free m-MDH with the same concentration as the immobilized ones.

activities. The activity of m-MDH immobilized on the TA-TEOS was calculated using the equation below:

$$\frac{\text{Units}}{\text{mL}} = \frac{(\Delta Atest(min) - \Delta Ablank(min)) \times Vf(mL) \times df}{6.22 \times Ve(mL)}$$

where Vf is the total volume of the assay, df is the dilution factor, 6.22 is the millimolar extinction coefficient of β-NADH at 340 nm, and Ve is the volume of enzyme used. According to the calculations, the average activity of m-MDH immobilized in TA-TEOS at room temperature was 56.8±2.9, while it was 11.6±0.4 for the m-MDH immobilized in nonporous SiNPs. The difference in activity is due to the different immobilization locations of the enzymes and the amount of the enzymes. In nonporous SiNP the m-MDH was adsorbed only on the surface while in the case of TA-TEOS, the enzymes were immobilized both on the external surface and inside the pores of the particles. The amount of the enzyme that was adsorbed by TA-TEOS was double the amount adsorbed by nonporous SiNPs, while the activity of m-MDH on TA-TEOS exceeded those on the nonporous SiNPs by five times. We conclude that the m-MDH that were adsorbed inside the pores have higher activity than the ones that were immobilized on the surface. The free enzymes have a four-fold higher catalytic activity (202.4) compared to the enzymes trapped inside the pores because the free enzymes are more accessible to the oxaloacetate molecules.

The denaturation of the enzymes at room temperature was evident by the reduced catalytic activity as shown in Figure 3.16. The activity of free m-MDH decreased 40-fold, and the consumption of β-NDAH decreased from 100% to 5% in 40 minutes at room

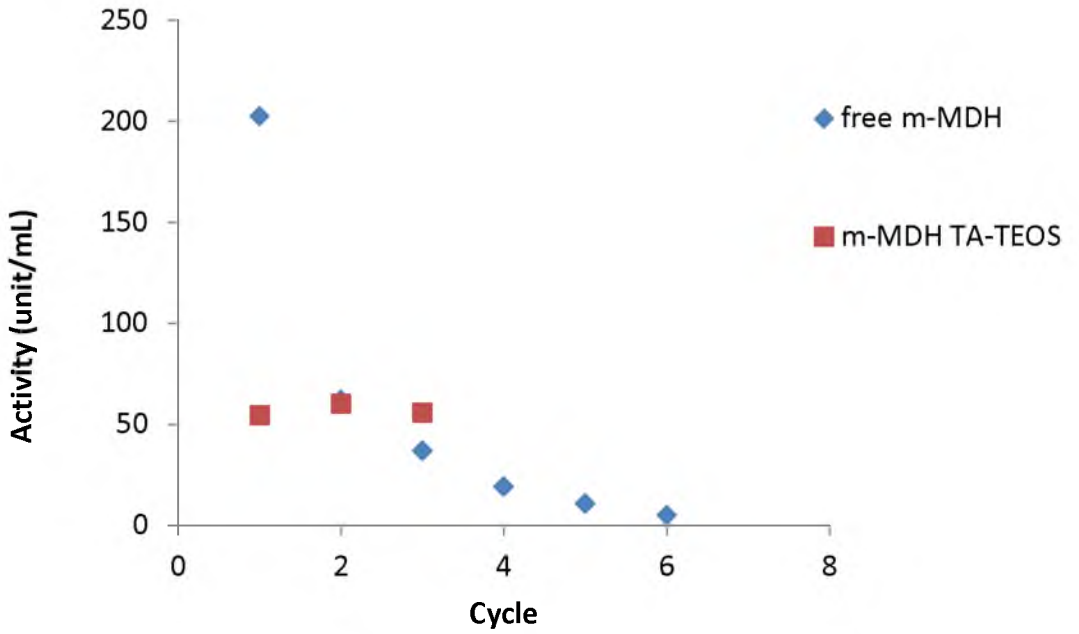

Figure 3.16. Catalysis activity of free m-MDH and m-MDH immobilized in TA-TEOS at room temperature.

temperature. At the same time, the enzymes loaded in the TA-TEOS did not show any reduction of reaction rate, and the conversion percentage of β-NDAH remained at 76%, which means the enzymes were protected by the silica matrix. The denaturation of m-MDH was due to the unfolding of the 3D structure of the enzyme in room temperature. The enhanced thermal stability of the m-MDH immobilized in TA contributed to the confinement of the 3D structure of the enzyme in the mesopores. This discovery is consistent with the report of Orita *et al.*[61] who immobilized antibodies into the MSNs with various pore sizes. Although the antibodies that were immobilized deeper in the large-pore MSNs showed lower activity, they possessed better stability in organic solvents and under thermal treatment.

3.4 Conclusion

We developed the use of tannic acid (TA) as a template to form a new type of relatively monodisperse mesoporous silica nanoparticles with a large pore volume and narrow pore size distribution. The particles were synthesised in the mixture of ethanol and ammonia giving them uniform, nearly spherical shapes with diameters smaller than 200 nm. The pore size could be tuned from 5 to 13 nm by varying the concentration of TA. Fluorescent tags were attached onto the surfaces and into the interior of the particles after the amination of the particles with APTES. We have explored the potential applications of the new materials in protein immobilization. The mesoporous TA-TEOS nanoparticles showed a high protein adsorption capacity of 77.1 mg/g for Lz, 396.5 mg/g for BHb and 130.0 mg/g for BSA in PBS buffer. The effects of electrostatic interactions and hydrogen bonding were illustrated by increasing the ionic strength of the media. We also demonstrated that TA-TEOS nanoparticles can encapsulate an enzyme, m-MDH, which showed enhanced stability at room temperature compared to the enzyme in free solution; and higher catalytic activity compared to the enzyme adsorbed on the surface of nonporous SiNPs. The TA SiNPs can be considered a prototype mesoporous SiNP that inspires the discovery of new mesoporous SiNPs prepared using other nonsurfactant molecules with rigid structure and abundant sites that are able to associate with silica precursors as a pore-generating template.

3.5 References

[1] Wu, S.; Hung, Y.; Mou, C. *Chem. Commun.* **2011**, *47*, 9972-9985.

[2] Vivero-Escoto, J. L.; Slowing, I. I.; Trewyn, B. G.; Lin, V. S.-Y. *Small* **2010**, *6*, 1952-1967.

[3] Trewyn, B. G., Giri, S., Slowing, I. I., and Lin, V. S.-Y. *Chem. Commun.***2007**, 3236-3245.

[4] Zhao, D.; Feng, J.; Huo, Q.; Melosh, N.; Fredrickson, G. H.; Chmelka, B. F.; Stucky, G. D. *Science* **1998**, *279*, 548-552.

[5] Hartmann, M. *Chem. Mater.* **2005**, *17*, 4577-4593.

[6] Kim, T.; Slowing, I. I.; Chung, P.; Lin, V. S. *ACS Nano* **2011**, *5*, 360-366.

[7] Slowing, I. I.; Vivero-Escoto, J. L.; Trewyn, B. G.; Lin, V. S.-Y. *J. Mater. Chem.***2010**, *20*, 7924-7937.

[8] Tang F.; Li, L.; Chen, D. *Adv. Mater.* **2012**, *24*, 1504-1534.

[9] Lu, F.; Wu, S. H.; Hung, Y.; Mou, C. Y. *Small* **2009**, *5*, 1408-1413.

[10] Tallury, P.; Payton, K.; Santra, S. *Nanomedicine* **2008**, *3*, 579-592.

[11] Lu, F.; Wu, S.; Hung, Y.; Mou, C. *Small*, **2009**, *5*(12), 1408-1413.

[12] Zhao, D.; Feng, J.; Hou, Q.; Melosh, N.; Fredrickson, G. H.; Chmelka, B. F.; Stucky, G. D. *Science,***1998**, *279*, 548-552.

[13] Rejman, J.; Oberle, V.; Zuhorn, I. S.; Hoekstra, D. *Biochem. J.* **2004**, *377*, 159–169.

[14] Kim, T.; Slowing, I. I.; Chung, P.; Lin, V. S. Y-. *ACS Nano*, **2011**, *5*, 360-366.

[15] Han, Y.; Ying, J. Y. *Angew. Chem. Int. Ed.* **2005**, *44,* 288-292.

[16] Gao, F.; Botella, P.; Corma, A.; Blesa, J.; Dong, L. *J. Phys. Chem. B* **2009**, *113*, 1796-1804.

[17] Stober, W.; Fink, A.; Bohn, E. *J. Collid. Interface Sci.* **1968**, *26*, 62-69.

[18] Wang, W.; Gu, B.; Liang, L.; Hamilton, W. *J. Phys. Chem. B* **2003**, *107*, 3400-3404.

[19] He, Q.; Shi, J.; Zhu, M.; Chen, Y.; Chen. F *Micropor. Mesopor, Mater.* **2010**, *131*, 314-320.

[20] Wei, Y.; Jin, D.; Ding, T.; Shih, W.-H.; Liu, X.; Cheng, S. Z. D.; Fu, Q. *Adv. Mater.* **1998**, *10*, 313-316.

[21] Wei, Y.; Xu, J.; Dong, H; Dong, J. H.; Qiu, K.; Jansen-Varnum, S.A. *Chem. Mater.* **1999**, *11*, 2023-2029.

[22] Erel-Unal, I.; Sukhishvili, S. A. *Macromolecules*, **2008**, *41*, 3962-3970.

[23] Shchepelina, O.; Kozlovskaya, V.; Kharlampieva, E.; Mao, W.; Alexeev, A.; Tsukruk, V. V. *Macromol. Rapid Commun.* **2010**, *31*, 2041–2046.

[24] Chen, S. C.; Chung, K. T. *Food and Chemical Toxicology* **2000**, *38,* 1-5.

[25] Gulcin, I.; Huyut, Z.; Elmastas, M.; Aboul-Enein, H. Y. *Arabian Journal of Chemistry,* **2010**, *3*, 43-53.

[26] Vance, R. E.; Teel, R. W. *Cancer Letters* **1989**, *47*, 37-44.

[27] Khan, W.A.; Wang, Z.Y.; Athar, M.; Bickers, D.R.; Mukhtar, H. *Cancer Letters* **1988**, *42,* 7-12.

[28] Aromal, S. A.; Philip, D. *Physica E*, **2012**, *44*, 1329-1334.

[29] Zhang, Y.; Chang, G.; Liu, S.; Lu, W.; Tian, J.; Sun, X. *Biosensors and Bioelectronics* **2011**,*28*(1), 344-348.

[30] Zhang, J.; Wu, J.; Feng, H.; Xu, P. *Xiandai Huagong*, **2011**, *3*, 56-60.

[31] Coenen, S; De Kruif, C. J. *J. Collid. Interface Sci.* **1988**, *124*, 104-110.

[32] Smith, M. A.; Lobo, R. F. *Microporous and Mesoporous Materials* **2010**,*131*(1-3), 204–209.

[33] Storck, S.; Bretinger, H.; Maier, W. F. *Applied Catalysis A: General* **1998**, *174*, 137-146.

[34] Yamada, H.; Urata, C.; Aoyama, Y.; Osada, S.; Yamauchi, Y.; Kuroda, K. *Chem. Mater.* **2012**, *24*, 1462-1471.

[35] Chen, K.; Zhang, J.; Gu, H. *J. Mater. Chem.*, **2012**, *22*, 22005-22012.

[36] Coradin, T; Eglin, D.; Livage, J. *Spectroscopy* **2004**, *18*, 567-576.

[37] Flocha, J.; Blaina, S.; Birotb, D.; Treguer, P. *Analytica Chimica Acta* **1998**, *377*, 157-166.

[38] Li, X.; Zhang, L.; Dong, X.; Liang, J.; Shi, J. *Microporous Mesoporous Mater.* **2007**, *102*, 151-158.

[39] Mitchell, K. K. P.; Liberman, Alexander; Kummel, A. C.; Trogler, W. C. *J. Am. Chem. Soc.* **2012**, *134*, 13997-14003.

[40] He, Q.; Shi, J.; Zhu, M.; Chen, Y.; Chen. F *Micropor. Mesopor, Mater.* **2010**, *131*, 314-320.

[41] Unger, K.K . In Porous Silica- Its Properties and Use as Support in Column Liquid Chromatography, Vol. 16, Elsevier: Amsterdam, **1979**

[42] Popat, A.; Hartonon, S. B.; Stahr, F.; Liu, J.; Qian S. Z.; Lu, G. Q. *Nanoscale*, **2011**, *3*, 2801-2818.

[43] Sun, Z.; Deng, Y.; Wei, J.; Gu, D.; Tu, B.; Zhao, D. *Chem. Mater.* **2011**, *23*, 2176-2184.

[44] Hudson S.; Cooney J.; Magner E. *Angew. Chem. Int. Ed.* **2008**, *47*, 8582-8594.

[45] Wang, Y.; Caruso, F. *Chem. Commun.* **2004**,1528-1529.

[46] Jin, W.; Brennan, J. D. *Anal. Chim. Acta* **2002**, *461*, 1-36.

[47] Wang, Y.; He,J.; Chen, J.; Ren, L.; Jiang, B.; Zhao, J. *ACS Appl. Mater. Interfaces*, **2012**, *4*, 2735-2742.

[48] Kisler, J. M.; Daehler, A.; Stevens, G. W.: O'Connor, A. J. *Microporous Mesoporous Mater.*, **2001**, *44-45*, 769-774.

[49] Vinu, A.; Murugesan, V.; Tangermann, O.; Hartmann, M. *Chem. Mater.*, **2004**, *16*, 3056-3065.

[50] Lei, C.H.; Shin, Y.S.; Liu, J.; Ackerman, E.J. *J. Am. Chem. Soc.* **2002**, *124*, 11242-11243.

[51] Han, Y.J.; Stucky, G.D.: Butler, A. . *J. Am. Chem. Soc.* **1999**, *121*, 9897-9898.

[52] Katiyar, A.; Ji, L.; Smirniotis, P. G.; Pinto, N. G. *Microporous Mesoporous Mater.* **2005**, *80*, 311-320.

[53] Yu, S.; Lee, S.B.; Kang, M.; Martin, C.R. *Nano Lett.* **2001**, *1*, 495-498.

[54] Leoni, L.; Attiah, D.; Desai, T. A. *Sensors* **2002**, *2*, 111-120.

[55] Smith, C.; Kirk, R.; West, T.; Bratzel, M.; Cohen, M.; Martin, F.; Boiarski, A.; Rampersaud, A.A. *Diabetes Technol. Therap.* **2005**, *7*, 151-162.

[56] Fan, J.; Lei, J.; Wang, L. M.; Yu, C. Z.; Tu, B.; Zhao, D. Y. *Chem. Commun.* **2003**, 2140-2141.

[57] Deere, J.; Magner, E.; Wall, J. G.; Hodnett, B. K. *Chem. Commun.* **2001**, 465-466.

[58] Katiyar, A.; Yadav, S.; Smirniotis, P. G.; Pinto, N. G. *J. Chromatogr. A* **2006**, 1122, 13−20.

[59] Bornscheuer, U. T. *Angew. Chem. Int. Ed.* **2003**, *42*, 3336-3337.

[60] Righetti, P.G.; Tudor, G. J. Chromatography, **1981**, *220*, 115-194.

[61] Orita,T.; Kato, K.; Tomita, M. J. Ceram. Soc. Jpn. **2011**, *119*, 238-245.

CHAPTER 4

DEGRADABLE BRIDGED SILSESQUIOXANE SILICA NANOPARTICLES

4.1 Introduction

Silica nanoparticles (SiNPs) offer an attractive platform for biomedical applications such as drug delivery and bioimaging, biocatalysis and bio-sensing.[1,2] Silica consists of silicon and oxygen atoms connected by very strong covalent bonds making SiNPs not particularly biodegradable and not vulnerable to microbial attacks.[3] In this respect, their application in vivo is problematic due to the accumulation of SiNPs in the liver, kidneys, bladder, spleen and lungs.[4] To obviate this problem, degradable silica-based materials have been proposed and synthesized.[5,6] Several recent reports describe some destabilization of silica by preparation conditions[7-10] and inclusion of biodegradable polymers, such as poly(L-lactic acid).[11,12] Doping metal cations into the silica matrix alters the composition of the SiNPs[13,14] and consequent removal of the cations by diffusion and chelation results in the destabilization of the silica structure.

SiNPs with controllable sizes from 20 to 1000 nm can be produced according to the well-established Stöber method.[15] Traditionally, the silica precursor used is tetraethoxysilane or tetramethoxysilane. We hypothesized that the incorporation of organic groups into SiNPs will result in tunable destabilization and porosity of silica. Although a number of SiNPs have already been produced from individual

organosilanes,[16] the organically modified silica nanoparticle technology is not fully developed.

Our hypothesis was that the silica lattice could be effectively destabilized by introducing degradable organic groups into its structure, leading to the formation of more hydrolysable SiNPs. Our goal was to achieve silica biodegradability via an entirely new approach— by using bridged silsesquioxane precursors. Recently, bridged silsesquioxane was used as a silica precursor to produce functional silica nanomaterials.[17-19] However, there are only a few publications about the synthesis of spherical bridged silsesquioxane SiNPs.[20] This chapter will describe the preparation of new hybrid SiNPs, including the design and synthesis of bridged silsesquioxanes with a cleavable ester as the linker; preparation of hybrid SiNPs; and investigation of the degradability of the novel particles. We expected that when the particles are placed in an aqueous environment, the ester would hydrolyze and this would weaken the structure, making degradable particles.

4.2 Experimental

4.2.1 Chemicals and instruments

All reagent-grade chemicals were used as received. Chloromethyl ester (CME, Alfa Aesar), 3-aminopropyltriethoxysilane (APTES, 99%, Sigma-Aldrich), ethylene glycol (EG, Mallinkrodt), tetraethoxysilane (TEOS, 99.999+%, Alfa Aesar), ammonium hydroxide (NH_4OH, 28-30% as NH_3, EMD Chemicals, Inc.), anhydrous potassium carbonate (K_2CO_3, EMD Chemicals, Inc.), 3-isocyanatopropyltriethoxysilane (ICPTES, Gelest), D-sorbitol (Sigma-Aldrich), sodium silicate solution (27% SiO_2, Riedel-de Haën), ammonium molybdate tetrahydrate (Alfa Aesar), sulfuric acid (Fisher Scientific), oxalic acid dehydrates (Aldrich), L- ascorbic acid (Research Products International Corp.) were

all used as received. Dichloromethane (CH_2Cl_2, reagent grade, Fisher Scientific) and triethylamine (Sigma-Aldrich) were freshly distilled. N,N-dimethylformamide (DMF, Mallinckrodt) was dried by anhydrous magnesium sulphate (Mallinckrodt). Methanol (ACS Reagent, Sigma-Aldrich), ethanol (200 proof, ACS-grade, Pharmaco-Aaper) and isopropyl alcohol (MACRON) were used as solvents without further purification. Millipore water (18 MΩ • cm) used in all experiments was obtained from a Barnstead "E-pure" water purification system.

The visual characterization was carried out by scanning electron microscopy (SEM, FEI NanoNova instrument) and transmission electron microscopy (TEM, FEI Philips Tecnai T-12 instrument). All the electronic spectrometry samples were prepared by drying particle from aqueous or ethanolic suspensions on silica nitride wafers for SEM or on holey carbon-coated Cu grids for TEM. The surface area and pore volume were measured by nitrogen sorption measurements, which were collected on a Micrometrics ASAP 2010 instrument at 77.3 K. All samples (~ 0.1 g) were degassed in the degassing port of the adsorption apparatus at 80 ℃ for approximately 6 h prior to the nitrogen sorption measurements. The surface-area measurement was based on the Brunauer-Emmett-Teller (BET) calculation method in a linear, relative pressure range between 0.05 and 0.25, and the pore-size distribution was based on the Barrett-Joyner-Halenda (BJH) method. UV-Vis measurements were performed using an Ocean Optics USB4000 instrument using a quartz cuvette. The particle hydrodynamic size and zeta-potential measurements were conducted in water using a NICOMP 380 ZLS ZetaPotential/Particle Sizer (PSS • NICOMP Particle Sizing Systems) at room temperature. Thermogravimetric analyses were performed by using a TA Instruments TGA 2950 Thermogravimetric

Analyzer under an N_2 atmosphere from 35 to 800 °C at a heating rate of 20 °C/min. FT-IR spectrometer (Thermo Scientific Nicolet 8700 model) was used for surface functional group detection. A Clay Adams Compact II Centrifuge (3200 rpm, Becton Dickinson) and ultracentrifuge Sorvall RC5B Plus (15000 rpm on a SA-600 rotor) were used for all centrifugations.

4.2.2 Synthesis of chloromethyl ester bridged (3-aminopropyl) triethoxysilane

All glassware was cleaned with millipore water and dried in the oven prior to use. Ten point two six mL (0.044 mol) of APTES and four g of anhydrous K_2CO_3 were added into a 250 mL round-bottomed flask with 100 mL of dichloride methane. One point seven six mL (0.02 mol) of CME were added to the flask, drop wise. The mixture was stirred and refluxed for 36 h under nitrogen atmosphere in an oil bath. After cooling down to room temperature, the K_2CO_3 was removed by filtration. The chloromethyl ester bridged (3-aminopropyl) triethoxysilane (CME-APTES) was obtained by rotary evaporation. Figure 4.1 shows the reaction. ^{1}H NMR (300 MHz, $CDCl_3$, δ): 8.28 (s, 1H), 5.73 (s, 2H), 3.86 – 3.75 (m, 12H), 3.22 (dd, J = 12.9, 6.8 Hz, 2H), 3.04 – 2.94 (m, 2H), 1.87 (dt, J = 15.3, 7.8 Hz, 2H), 1.74 – 1.54 (m, 2H), 1.28 – 1.14 (m, 18H), 0.77 – 0.56 (m, 4H).

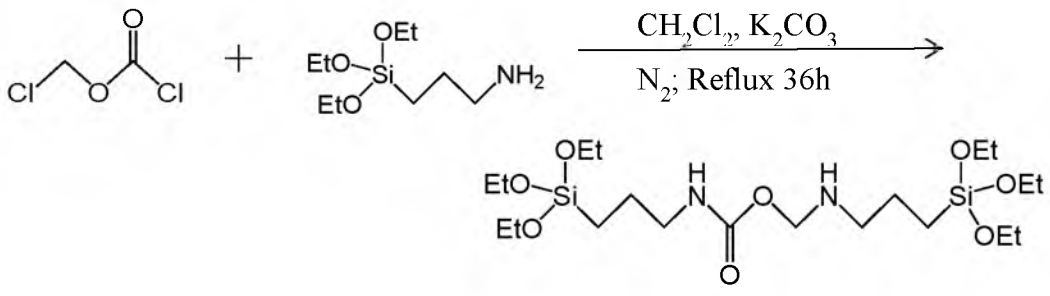

Figure 4.1. The synthesis of CME-APTES silsesquioxane.

4.2.3 Preparation of CME-APTES silica spheres

Both hydrochloride and ammonium hydroxide were employed as acid and base catalysts, respectively, for the sol-gel reaction. Water from the concentrated ammonium hydrochloride was the source of water for the sol−gel hydrolysis reaction to occur. Varied amounts of 2 M HCl and concentrated NH_4OH were added to ethanol solutions of CME-APTES. After stirring for 2 h under N_2, the materials were separated by centrifugation and purified with multiple washes with ethanol and water.

4.2.4 Preliminary study of degradation behavior of CME-APTES silica spheres

Ten mg of CME-APTES particles were suspended in 3 mL of either basic or acidic solution for different time spans. The resulting particles were centrifuged and washed with water. DLS, SEM and TEM were employed to visualize the changes in morphology of the particles.

4.2.5 Synthesis of ethylene glycol bridged isocyanatopropyltriethoxysilane

Fifteen mL of anhydrous $MgSO_4$-dried DMF were flushed repeatedly with nitrogen in the 50ml round bottom flask in an oil bath. After the addition of 27.9 μL (0.5 mmol) of ethylene glycol and 264.4 μL (1.05 mL) of 3-isocyanatopropyltriethoxysilane (ICPTES), the flask was heated to 80 °C. The reaction continued under nitrogen for 12 h and cooled to room temperature. The product was rotary-evaporated and characterized by NMR. Figure 4.2 shows the reaction of ethylene glycol bridged isocyanatopropyltriethoxysilane synthesis. ^{1}H NMR (300 MHz, $CDCl_3$) δ 8.21 (s, 2H), 4.62 (s, 4H), 3.94 – 3.66 (m, 12H), 3.30 – 3.05 (m, 4H), 1.68 – 1.51 (m, 4H), 1.31 – 1.13 (m, 18H), 0.71 – 0.53 (m, 4H).

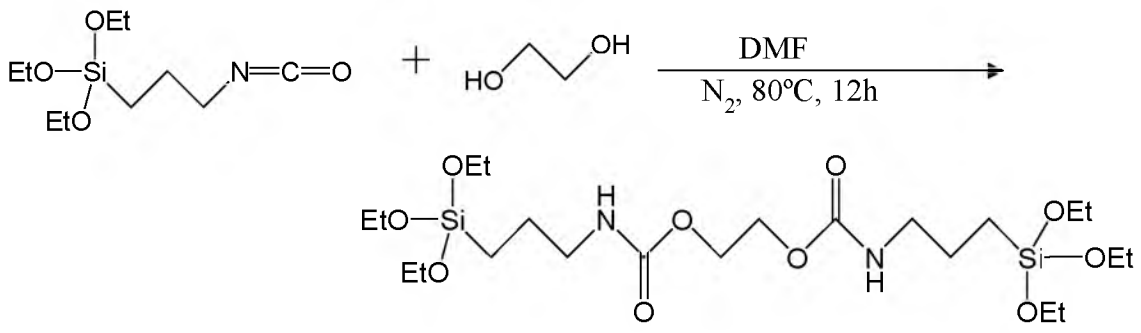

Figure 4.2. The synthesis of ICPTES-EG silsesquioxane.

4.2.6 Synthesis of ethylene glycol bridged isocyanatopropyltriethoxysilane particles

The ICPTES-EG SiNPs were produced by co-condensation. Point four g of ICPTES-EG were dissolved in 9 mL of ethanol by sonication, followed by the addition of 3 mL of NH_4OH and 0.304 mL of TEOS. The mixture was stirred at room temperature for 2 h. The resulting particles were collected by centrifugation, and washed with ethanol and water to remove ammonium hydroxide and the excess of silica precursors. The resulting particles were air-dried and stored in powder form.

4.2.7 Synthesis of sorbitol-bridged isocyanatopropyltriethoxysilane

Sorbitol-bridged isocyanatopropyltriethoxysilane (ICPTES-sorbitol) was prepared following a published approach.[21] Point two g of sorbitol were added to 3 mL dry DMF in a round bottom flask, soaked in an oil bath under continuous flow of nitrogen. The temperature was elevated to 40 °C to accelerate the dissolving rate of sorbitol. When the sorbitol fully dissolved in DMF, 306 μL of freshly distilled triethylamine and 542 μL of

ICPTES were added to the mixture. The temperature of the solution was maintained at 90 ºC for the next 3 days. The product consisting of pale yellow solids was collected by rotary evaporator. The reaction is shown in Figure 4.3. ^{1}H NMR (300 MHz, $CDCl_3$, δ): 8.01 (s, 2H), 4.36 – 4.00 (m, 4H), 3.90 – 3.72 (m, 12H), 3.70 (s, 2H), 3.14 (d, J = 22.3 Hz, 4H), 1.87 (s, 6H), 1.62 (s, 6H), 1.32 – 1.12 (m, 18H), 0.62 (s, 4H).

4.2.8 Synthesis of sorbitol bridged isocyanatopropyltriethoxysilane SiNPs

The ICPTES-sorbitol SiNPs were synthesized by co-condensation of TEOS with ICPTES-sorbitol under the basic condition. The reaction conditions were manipulated to achieve the optimum production of monodisperse silica spheres. A typical ICPTES-sorbitol SiNPs synthesis method is described as follows: point zero four g of ICPTES-sorbitol were dissolved in 10 mL of ethanol by 1 h sonication. Any remaining undissolved solids were excluded from the reaction by using the clear supernatant. Five mL of NH_4OH were added to this supernatant followed by the addition of 0.06 mL of TEOS with vigorous stirring. The onset of turbidity after a short while indicated the start of silica sphere formation. The reaction was conducted at room temperature for 2 h. The particles were washed with ethanol and water, and collected by 40 min centrifugation.

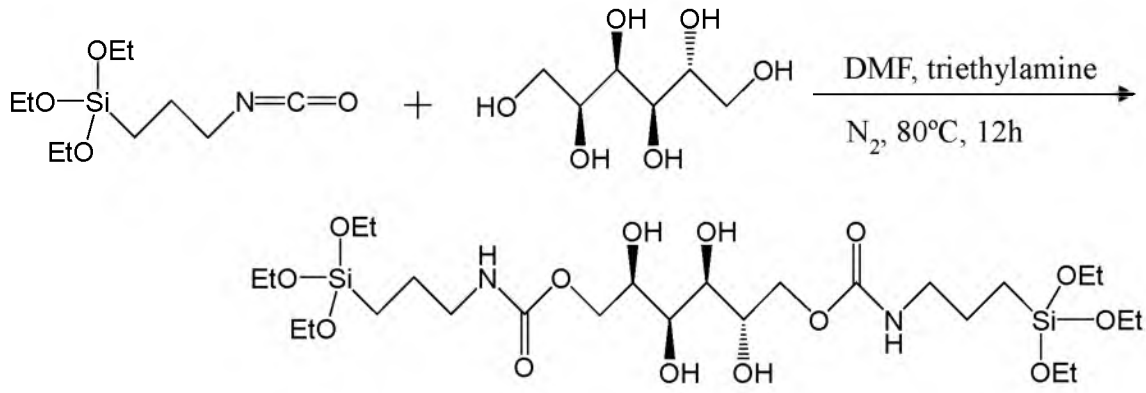

Figure 4.3. The synthesis of ICPTES-sorbitol silsesquioxane

SiNPs synthesized under the same condition without the addition of ICPTES-sorbitol were also prepared as a reference. All the resulting particles were air-dried and stored in powder form.

4.2.9 Synthesis of 340 nm SiNPs

The 340 nm silica spheres were prepared according to modifications of previously reported procedures.[22] Five hundred mL of an ethanolic solution containing TEOS (51.4 mL, 0.20 mol) was mixed with 500.0 mL of an ethanolic solution containing NH_4OH (70.0 mL, 1.1 mol) and water (257 g, 14.3 mol). These two solutions were poured simultaneously in a 2 L Erlenmeyer flask and vigorously stirred. The resulting mixture has final concentrations of 0.2 M TEOS, 1.1 M NH_3 and 17.0 M H_2O. After 24 h, the mixture was then poured into 15 mL centrifuge tubes and centrifuged for 10 min. The supernatant was discarded, leaving the spheres as pellets at the bottom of the centrifuge tubes. Purification of the spheres was achieved by a repetitive cycle of suspending the spheres via sonication for 10 min followed by centrifugation for 10 min in a gradient series of 10 mL supernatant: 100% water, then 25% ethanol, then 50% ethanol, then twice in 75% ethanol, and finally in 100% ethanol. After the final rinsing, the supernatant was decanted and the silica spheres were air-dried overnight.

4.2.10 Molybdenum blue colorimetric experiment

All the solutions were contained in polyethylene bottles. Standard silicic acid solution was made by diluting sodium silicate solution ($Na_2Si_3O_7$, 242.23 g/mol). Three solution stocks were prepared:[23] (1) 3.1 g of ammonium molybdate tetrahydrate dissolved in 50 mL of 1 M sulfuric acid, (2) 6.3 g of oxalic acid dihydrate dissolved in 50 mL of millipore water and (3) 1.76 g of ascorbic acid dissolved in 50 mL of millipore water.

Sonication was used to help dissolve the salts. In order to make a calibration curve, the standard silicic solutions with concentrations of 1.72×10^{-5} M, 8.56×10^{-5} M, 1.703×10^{-4} M, 2.54×10^{-4} M, 3.37×10^{-4} M, and 4.195×10^{-4} M respectively were prepared. 100 μL of Solution 1 was added to 2 mL of the sample. After 10 min, the solution became yellow due to the formation of yellow phosphate molybdenum complex. 100 μL of Solution 2 was then added and the yellow color faded in 1 min. The addition of 100 μL of Solution 3 resulted in a color change to blue. The mixture was allowed to sit for an additional 10 min until the completion of the blue complex formation. The UV-vis spectrum featured a molybdenum blue peak at 810 nm. The concentration of silicic acid was calculated from the calibration curve.

10 mg of 340 nm Stöber SiNPs and ICPTES-sorbitol SiNPS were each separately dispersed in 20 mL of millipore water. An aliquot of each solution was centrifuged every hour. 100 μL of each supernatant was diluted by 2 mL of water, and the resulting solutions were tested by the procedure aforementioned.

4.3 Results and discussion

4.3.1 Synthesis of bridged silsesquioxanes

The aim of this project was to produce novel degradable SiNPs by using alkoxysilane precursors carrying organic groups to destabilize the silica network. Aryltrialkoxy- and diaryldialkoxysilanes were tried first due to the assumption that their electron-withdrawing aromatic structure might weaken the Si-O bonds. However, because of the steric repulsion, the aryltrialkoxy- and diaryldialkoxysilanes did not form monodisperse SiNPs. Thus, an alternative strategy of introducing bridged silsesquioxane

with cleavable linkers into the silica network was performed (Figure 4.4). We synthesised a series of ester-bridged silanes as silica precursors, including the chloromethyl ester (CME)-bridged silane, ethylene glycol (EG)-bridged silane, and sorbitol-bridged silane. While the preparation of the sorbitol-bridged silane was accomplished according to the approach published by the Corriu group,[21] we also developed the synthesis of two new bridged silanes.

4.3.2 Synthesis and characterization of CME-APTES SiNPs

There are currently no reports on the synthesis of CME-APTES in the literature, thus the reaction conditions were adapted from other reactions involving the APTES and chloride molecules.[24] However, we came across problems while purifying the product. The column silica gel, which contains moisture, accelerates the degradation of the silane since the carbamate linkers of CME-APTES are highly hydrolysable. Moreover, the high affinity between the silica gel and product silane prolonged the retention time in the column during purification, which further enhanced the hydrolysis of the product. As verified by its NMR spectrum, the column-purified sample degraded into some other products, while the unpurified product revealed expected NMR peaks. The product was stored in a dessicator to prevent the degradation caused by the moisture in the air. The NMR spectrum of CME-APTES stored in the dessicator for a week displayed some noise

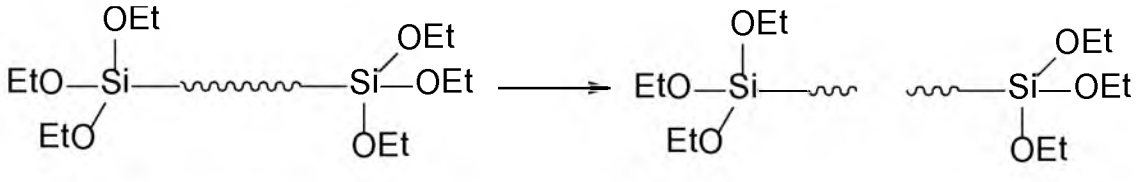

Figure 4.4. Schematic illustration of bridged silsesquioxane with cleavable linker.

peaks indicating degradation of the silane. Therefore, to produce the hybrid SiNPs, freshly produced bridged silsesquioxane products were used.

The goal of this project was to produce spherical and monodispersed degradable SiNPs for bio-applications. Various reaction conditions that were used to optimize the preparation conditions of CME-APTES SiNPs are listed in Table 4.1. Both HCl and ammonium hydroxide were used to catalyse the hydrolysis and condensation of bridged silsesquioxanes. It is known that acidic conditions are more likely to yield silica gels or other soft networks of silica rather than uniform particles.[25] In our case, the acid-catalysed products were irregularly shaped aggregates. In the base-catalysed reactions, the ratio between ammonium hydroxide and ethanol, the amount of the silica precursor, as well as the reaction time were manipulated to obtain spherical nanoparticles. With a low ratio (< 1:3) between the ammonium hydroxide and ethanol, the reaction solution remained clear after 2 h and no particles were obtained after the centrifugation. Therefore, we increased the concentration of the catalyst in order to accelerate the reaction. With extremely high concentration of ammonium hydroxide (1:2 v/v), we obtained silica gel after 2 h with and without stirring. Based on the SEM images of products prepared by various reaction conditions, we focused on CME-APTES-B-3-02, which corresponds to SiNPs synthesised under the condition of 1:3 ratio of ammonium hydroxide and ethanol with 0.2 g of CME-APTES (Figure 4.5). The hydrodynamic diameter of CME-APTES is shown in table 4.2. After the CME addition, the mixture became opalescent in several minutes and became increasingly opaque in the following hours, indicating the growth of the particles. The resulting particles were spherical with an average diameter of 2.3±0.2 μm. Reaction time was varied from 2 h to 18 h. The resulting particles showed increasing

Table 4.1. Production conditions for CME-APTES SiNPs

Sample	Catalyst	EtOH	CME-APTES	Reaction Time
CME-APTES-HCl-10-01-2h	1 ml HCl 2M	10 mL	0.1 g	2 hours
CME-APTES-HCl-3-01-2h	3 ml HCl 2M	9 mL	0.1 g	2 hours
CME-APTES-HCl-10-02-18h	1 ml HCl 2M	10 mL	0.2 g	18 hours
CME-APTES-B-10-01-2h	1 ml NH_4OH	10 mL	0.1 g	2 hours
CME-APTES-B-3-02-2h	3 ml NH_4OH	9 mL	0.2 g	2 hours
CME-APTES-B-2-02-2h	4 ml NH_4OH	8 mL	0.2 g	2 hours
CME-APTES-B-1-02-2h	5 ml NH_4OH	5 mL	0.2 g	2 hours
CME-APTES-B-3-04-2h	3 ml NH_4OH	9 mL	0.4 g	2 hours
CME-APTES-B-3-02-4h	3 ml NH_4OH	9 mL	0.2 g	4 hours
CME-APTES-B-3-02-6h	3 ml NH_4OH	9 mL	0.2 g	6 hours
CME-APTES-N-3-02-18h	3 ml NH_4OH	9 mL	0.2 g	18 hours

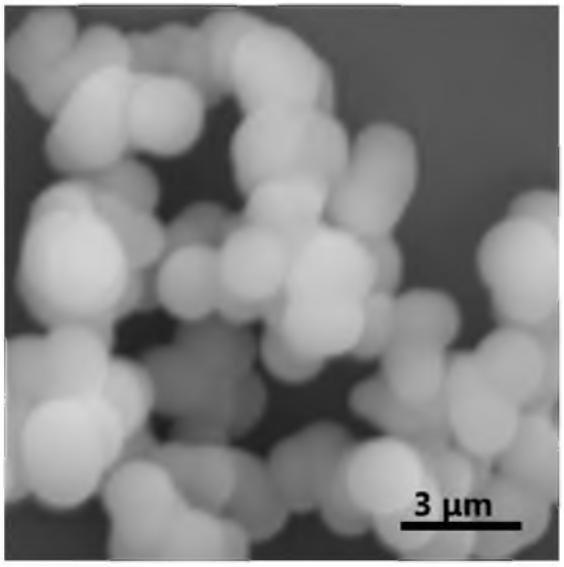

Figure 4.5. SEM images of CME-APTES-B-3-04-2h (CME-APTES SiNPs).

size polydispersity with longer reaction time. Below, CME-APTES-B-3-02-2h is referred to as CME-APTES SiNPs.

Because of the low yield of CME SiNPs, another kind of SiNPs involving the use size polydispersity with longer reaction time. Below, CME-APTES-B-3-02-2h is referred to as CME-APTES SiNPs. of CME-APTES silane was produced. TEOS is commonly used as a silica precursor.[16] CME-APTES co-condensed with TEOS led to the formation of nanoparticles wherein the TEOS reinforced the spherical skeleton; while the organosilane CME-APTES, which is assumed to be uniformly present throughout the particle body, destabilized the particles. Different reaction times, namely 2 h and 18 h, were employed with a high concentration of NH_4OH (1:3 v/v). The resulting particles had no significant differences in size and morphology according to the SEM images. Similar to CME-APTES SiNPs, the synthesis conditions were optimized. The resulting CME-APTES-TEOS SiNPs were polydisperse according to the DLS data. This was due to the aggregation of the particles as shown in the SEM and TEM images (Figure 4.6).

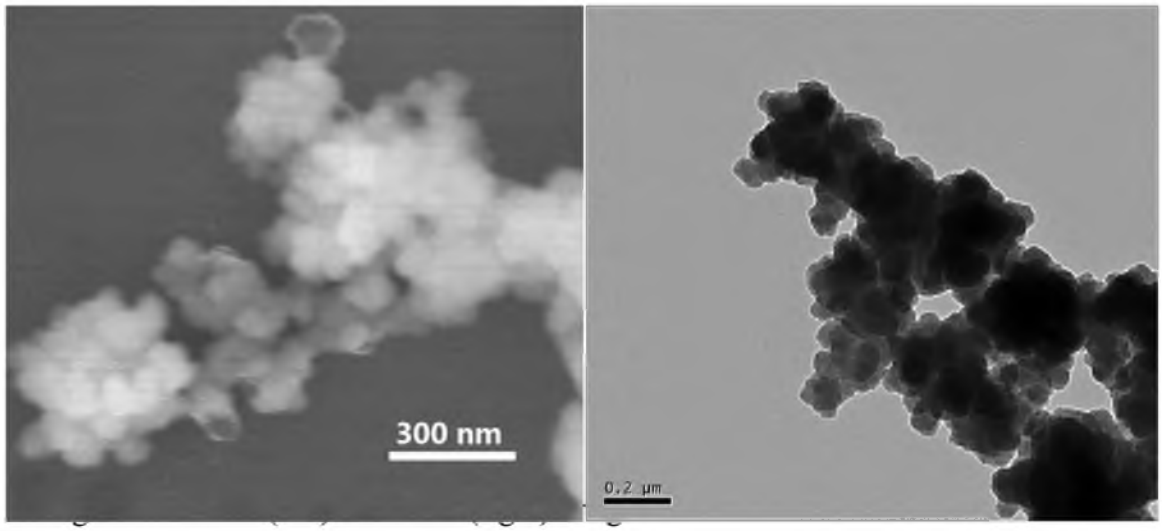

4.3.3 Degradation of CME-APTES SiNPs

The CME-APTES particles were difficult to disperse in aqueous solutions. The DLS data showed aggregation of the particles in water even after hours of sonication (Table 4.2). The CME-APTES SiNPs dissolved in 1 M NaOH solution in 30 min, while the reference 340 nm SiNPs produced via Stöber method fully dissolved in the same solution after 45 min. The dissolution of the particles was monitored by DLS. DLS data of CME-APTES SiNPs in water and under acidic condition (HCl pH=2) are summarized in Table 4.2. The SEM images showed that after 3 days under the acidic condition, the diameter of the particles decreased, and the residue of the dissolved material was observed around the particles (Figure 4.7). The particles shrank continuously and started to aggregate after 10 days. With a longer immersion time, the particles formed irregularly shaped aggregates.

Table 4.2. DLS data of CME-APTES SiNPs

	Average Diameter	**Distribution**
CME SiNPs	1580.9 ± 274.7 nm	100%
CME SiNPs in acid 3 days	341.1 ±76.3 nm	87.6%
	1800.1 ± 320.9 nm	12.4%
CME SiNPs in acid 10 days	215.1 ±51.3 nm	85.8%
	1800.1 ± 172.3 nm	14.2%

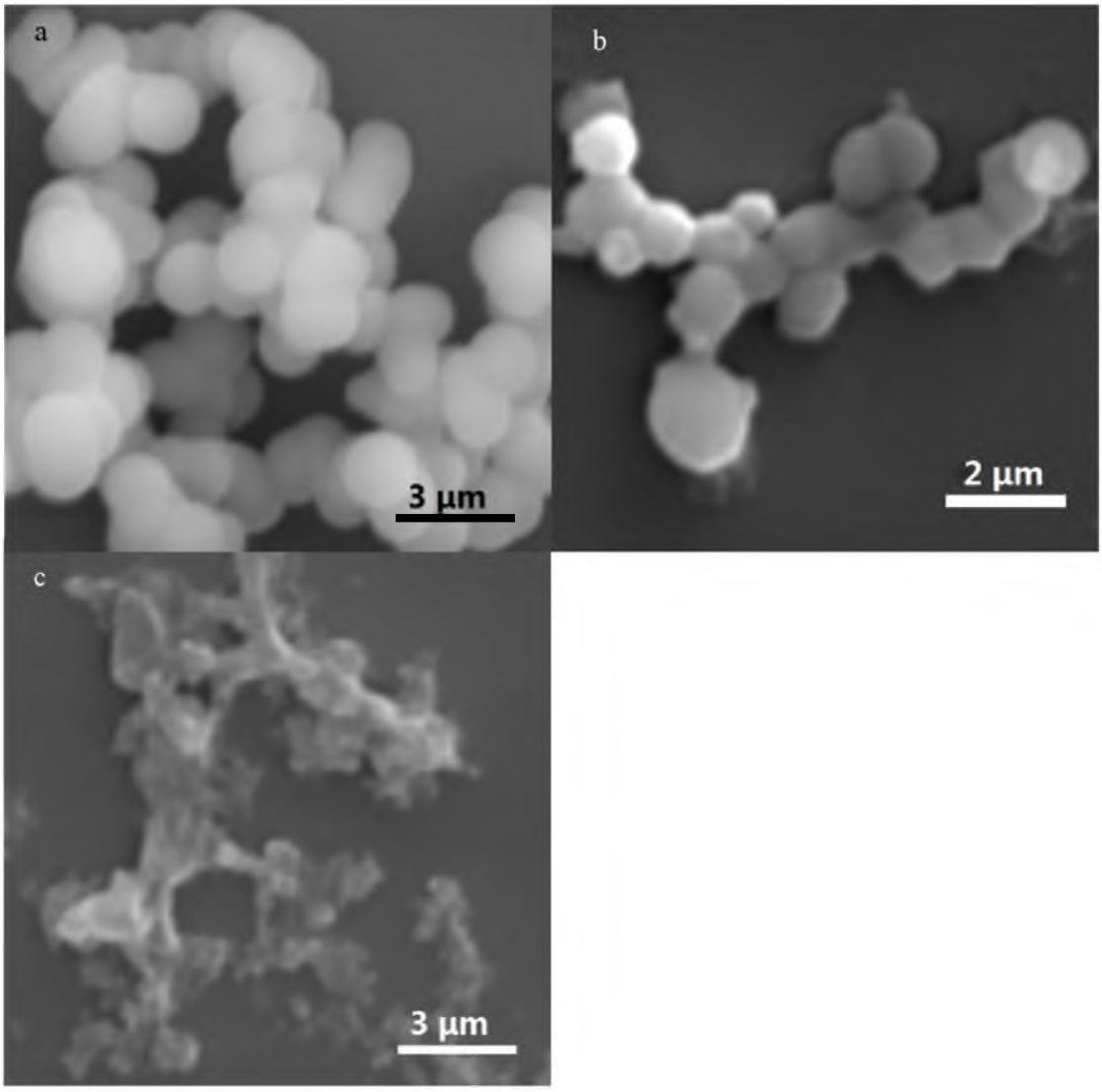

Figure 4.7. SEM images of CME-APTES SiNPs in a) ethanol b) HCl solution for 3 days and c) HCl solution for 10 days

All stability tests for CME-APTES-TEOS SiNPs were based on the particles that were synthesised under the conditions of 0.4 g CME-APTES silane, 0.38 mL of TEOS, 3.8 mL of NH_4OH and 11.4 mL of ethanol. The degradability of the CME-APTES-TEOS SiNPs was tested under the acidic conditions. The agglomeration of the particles dispersed after 6 days in acidic solution is shown in SEM images, and was also corroborated by DLS data (Table 4.3). The high-resolution TEM images showed that the edge of the particles degraded and became smoother after the immersion in acidic solution (Figure 4.8). After 2.5 months, the particles dissolved into flakes and no aggregation or spherical particles were observed. In contrast, the SiNPs synthesised without CME-APTES remained spherical with no obvious shape change in the acidic solution. The preliminary results from the degradability tests verified that by using the cleavable bridges silsesquioxane as the silica precursor, degradable silica nanoparticles can be created. However, both of the CME-APTES and CME-APTES-TEOS NPs suffered from aggregation, which might cause adverse effects in biomedical applications. Thus, we prepared other ester-bridged silsesquioxanes and explored their ability to produce degradable SiNPs.

Table 4.3. DLS data of CME –TEOS SiNPs

	Average Diameter	**Distribution**
CME-APTES-TEOS SiNPs	626.6 ± 103.6 nm	62.3%
	2428.3 ± 302.5 nm	37.7%
CME-APTES-TEOS SiNPs in acid 6 days	240.5 ± 45.7 nm	91.9%
	1132.6 ± 186.0 nm	8.9%
CME-APTES-TEOS SiNPs in acid 2.5 months	19.7 ± 1.1 nm	100%

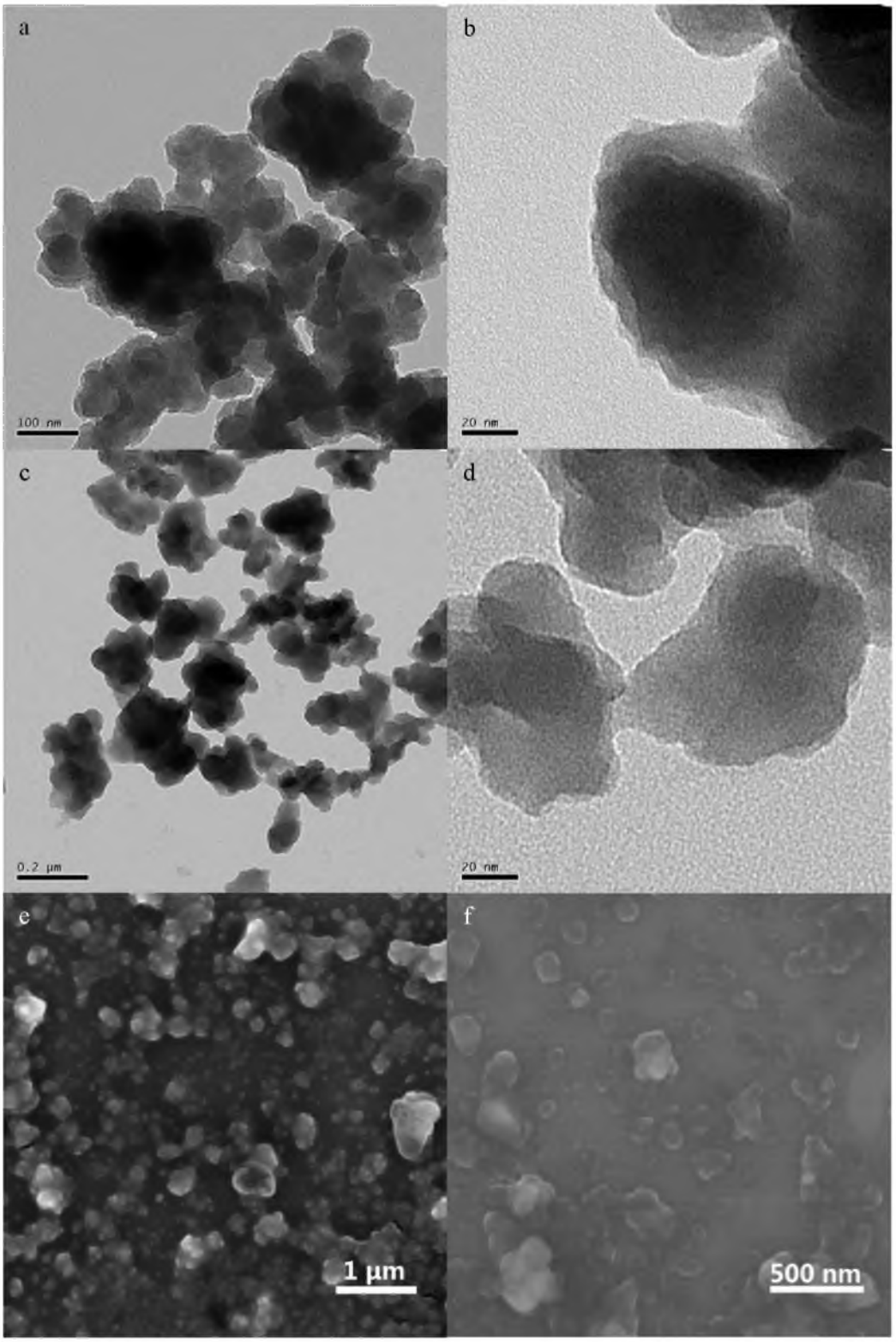

Figure 4.8. TEM images of CME-APTES-TEOS SiNPs (a,b) in ethanol, (c,d) in acidic solution for 10 days. SEM images of e) CME-SiNPs in HCl solution for 1.5 months and f) CME-SiNPs in HCl solution for 2.5 months.

4.3.4 ICPTES-EG SiNPs

ICPTES-EG does not form nanoparticles by itself under the basic catalysis. With the use of TEOS as a co-condensation agent, we were able to obtain small particle clusters, which were observed using SEM and TEM (Figure 4.9). After 1 week in HCl solution, significant coalescence took place to form larger clusters. This appreciable interparticle conglutination is likely due to the continuous hydrolysis and condensation of the silica particles.

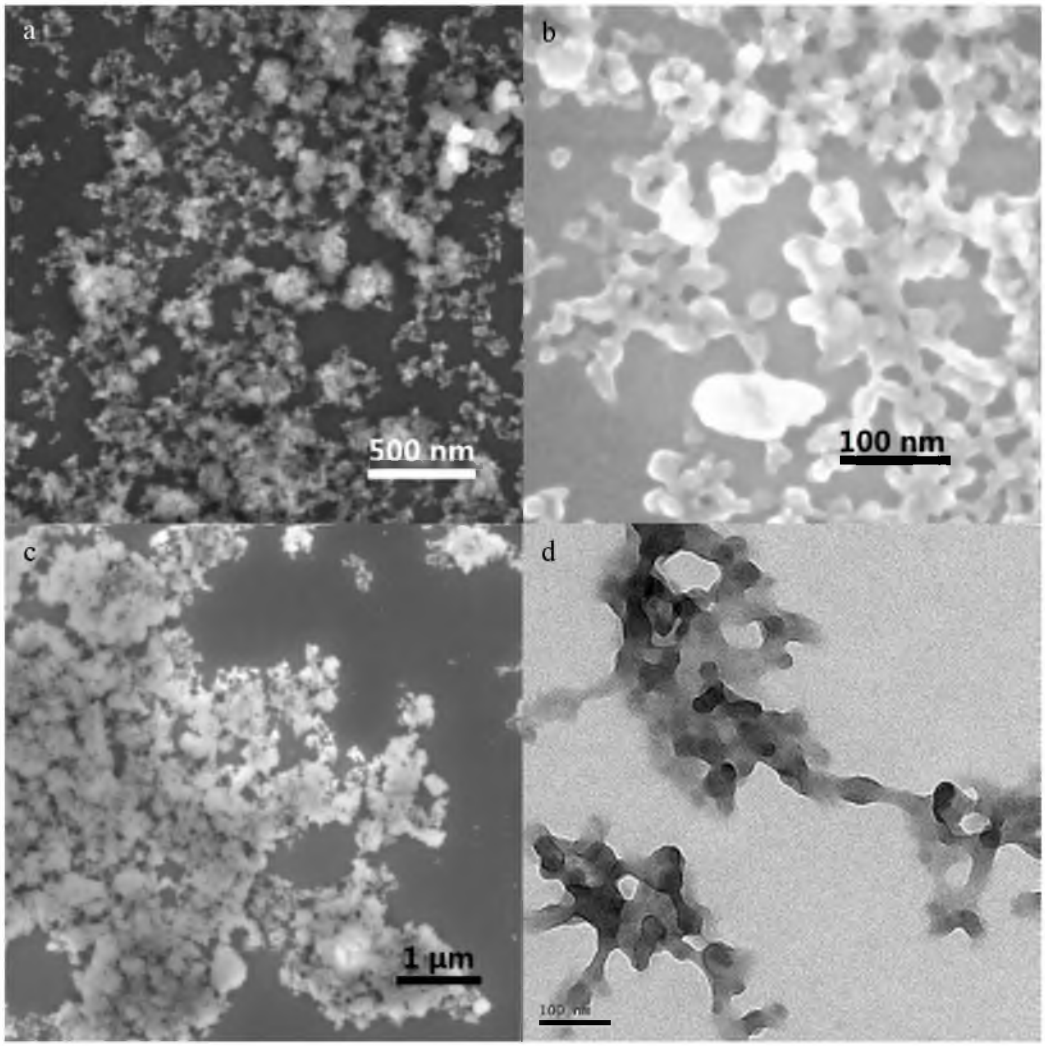

Figure 4.9. SEM images of a,b) ICPTES-EG-TEOS SiNPs c) ICPTES-EG-TEOS SiNPs in HCl solution for 1 week d) TEM image of ICPTES-EG-TEOS SiNPs.

4.3.5 Synthesis and characterization of ICPTES-Sorbitol SiNPs

The ICPTES-sobitol was synthesized according to a published method.[21] The ICPTES-sorbitol has two carbamate functionalities as cleavable sites. Sorbitol is used as a sweetener in the food industry. It is nontoxic and can be absorbed and recycled by the human body;[26] hence the degradation of the ICPTES-sorbitol should not induce adverse biological reactions.

Similar to ICPTES-EG, the use of pure ICPTES-sorbitol did not produce SiNPs. Thus, we first intended to coat 50 nm Stöber SiNPs[27] with ICPTES-sorbitol shell under the basic catalysis conditions. Preshrunk SiNPs (subjected to a thermal treatment up to 600 °C for 4 h) were used first. After the overnight reaction, the particles could be separated from the solution by 3400-rpm centrifugation, while the Stöber 50 nm nanoparticle required 15000-rpm centrifugation to collect. However, the shorter centrifugation time was not due to the increase of the particle size, but due to the aggregation caused by the addition of ICPTES-sorbitol, which interconnected the particles. 50 nm SiNPs and the SiNPs with the addition of ICPTES-sorbitol showed similar average size: 80.2 ± 9.3 nm and 76.0 ± 5.6 nm. We had hoped that by doubling the amount of the bridged silsesquioxane we would be able to grow a shell around the original SiNPs. However, no increase in the particle size was observed. Fresh 50 nm SiNPs were prepared because they possess higher density of the silanol groups on the surface, which offer more condensation sites for ICPTES-sorbitol. The zeta potential of preshrunk SiNP (-34.6 ± 0.2 mV) vs. fresh SiNPs (-47.0 ± 0.5 mV) illustrated that the fresh SiNPs had higher silanol coverage because the negative surface charge was mainly due to the negatively charged silanol groups. We tried two different concentrations of

ICPTES-sorbitol to produce the shell, but according to SEM, no silica shell was formed onto the particles.

Spherical SiNPs were only produced when the ICPTES-sorbitol functioned as a co-silica precursor and co-condensed with TEOS under the basic condition. We optimized the concentration ratios of precursors, solvent and catalyst as listed in Table 4.4. We confirmed particle formation under different reaction conditions by SEM. Longer reaction time led to the aggregation of the particles, assuming that the particles were formed in the first 2 h due to the fast hydrolysis and condensation rate. Then the excess silica precursors condense loosely on the surface of the particles forming interconnections between the particles. The ratio between the TEOS and ICPTES-sorbitol also played a critical role, where the spherical shape mainly depends on TEOS concentration (Figure 4.10). Too much ICPTES-sorbitol prevented the formation of the uniform spherical structure of the particles; on the other hand, too much TEOS led to the formation of particles with limited degradability. Therefore, after several trials, we found that the best ratio between the ICPTES-sorbitol and TEOS was approximately 1:5, which led to the formation of uniform nanospheres with the largest proportion of the organosilane as the degradable component and average diameter of 122.2±12.3 nm. The typical spherical ICPTES-sorbitol SiNPs are shown in Figure 4.11.

As a control, TEOS SiNPs nanoparticles were synthesized under the same condition as ICPTES-sorbitol-7 (referred to as ICPTES-sorbitol) (Table 4.4) without adding ICPTES-sorbitol and utilizing TEOS as the only silica source. The reference SiNPs synthesized from TEOS condensation had the average diameter of 426.9±28.8 nm (Figure 4.11), which was significantly larger than the hybrid ICPTES-sorbitol SiNPs.

Table 4.4. The reaction conditions of ICPTES-sorbitol SiNPs.

	ICPTES-sorbitol	TEOS	EtOH	NH_4OH	Time
1	0.2 g (3.0×10^{-4} mol)	0.15 ml (6.8×10^{-4} mol)	10 mL	5 mL	18 hours
2	0.2 g (3.0×10^{-4} mol)	0.3 ml (1.4×10^{-3} mol)	10 mL	5 mL	18 hours
3	0.2 g (3.0×10^{-4} mol)	1 ml (4.5×10^{-3} mol)	10 mL	5 mL	18 hours
4	0.2 g (3.0×10^{-4} mol)	1 ml (4.5×10^{-3} mol)	11.25 mL	3.75 mL	18 hours
5	0.2 g (3.0×10^{-4} mol)	2 ml (9.0×10^{-3} mol)	12 mL	4 mL	18 hours
6	0.02 g (3.0×10^{-5} mol)	0.03 ml (1.4×10^{-4} mol)	10 mL	5 mL	2 hour
7	0.04 g (6.0×10^{-5} mol)	0.06 ml (2.8×10^{-4} mol)	10 mL	5 mL	2 hours

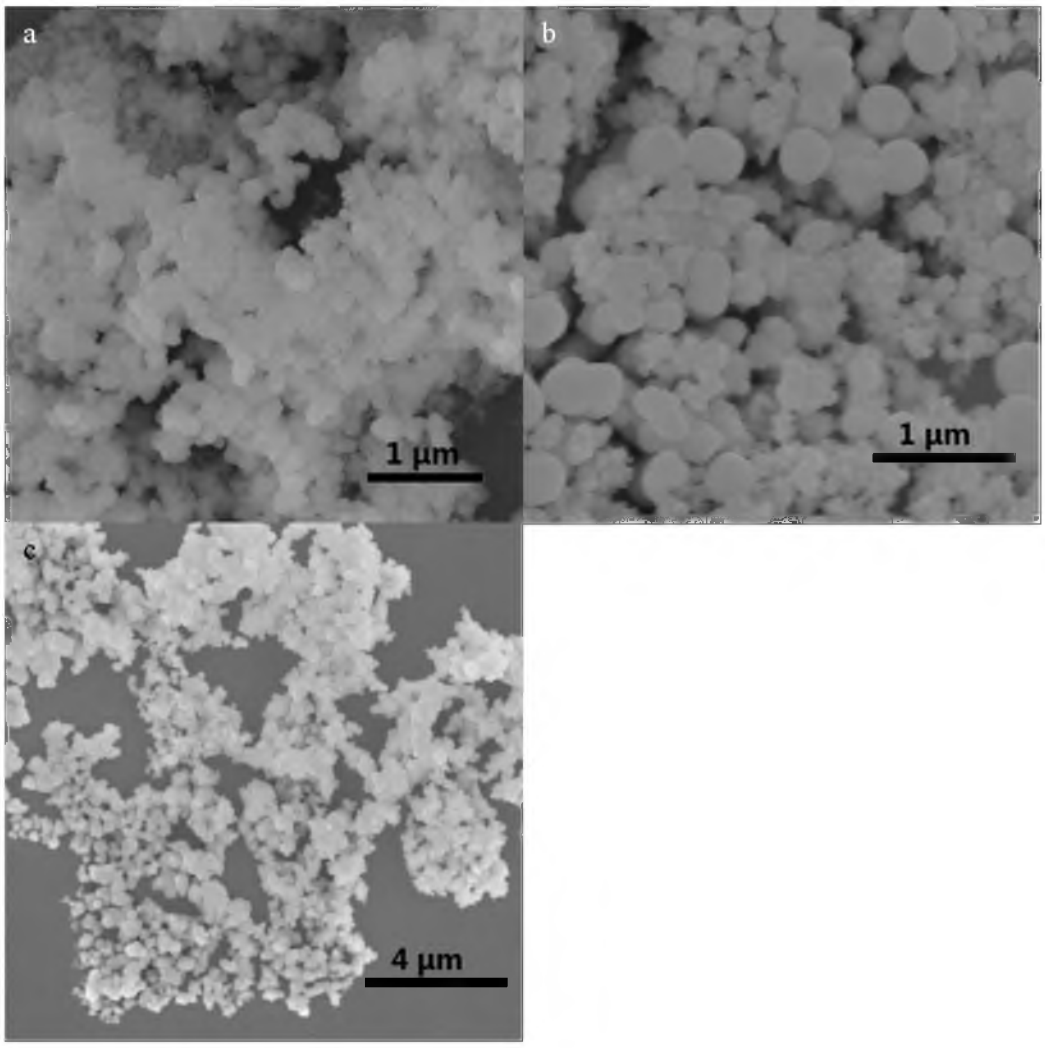

Figure 4.10. SEM images of ICPTES-TEOS SiNPs synthesized with increasing (a < b < c) concentration of TEOS.

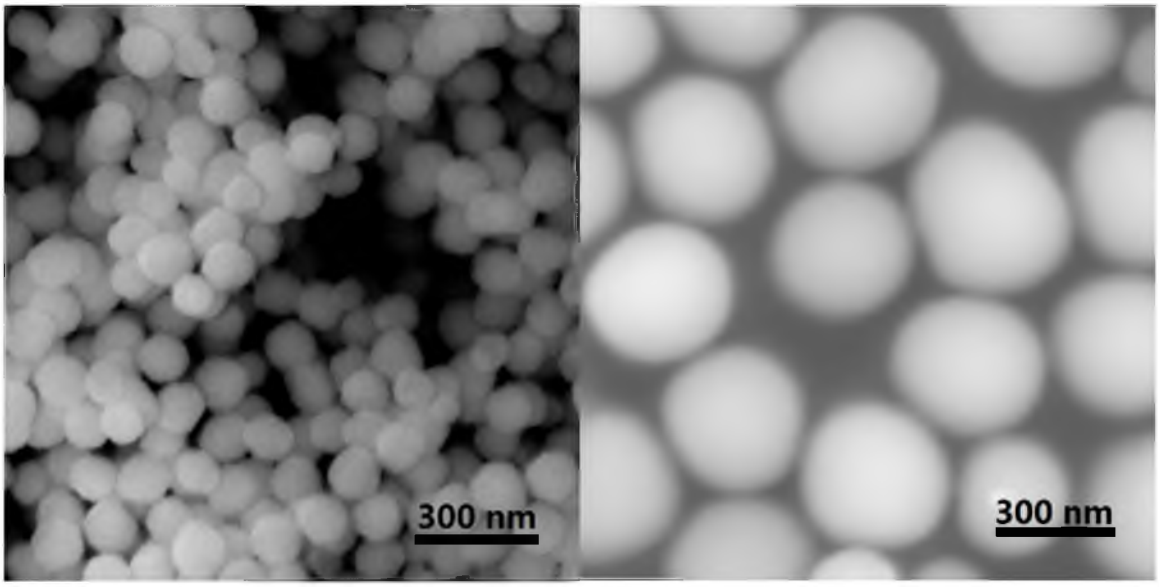

Figure 4.11. SEM images of a) ICPTES-sorbitol NPs and b)SiNPs produced in the same condition using TEOS as the only silica precursor.

The TGA measurements also demonstrated the incorporation of organic groups in the ICPTES-sorbitol NPs. 10 mg of ICPTES-sorbitol NPs and reference SiNPs were analyzed by TGA, and the weight loss from 35-800 °C was recorded. The weight loss under the temperature of 150 ℃ resulted from the loss of moisture while the weight losses at higher temperature were attributed to the calcination of the organic groups (Figure 4.12). A weight loss difference of 6.2% between the ICPTES-sorbitol SiNPs and TEOS SiNPs suggested that the ICPTES-sorbitol was incorporated into the silica network of the ICPTES-sorbitol SiNPs. Assuming the 6% weight loss all comes from the organo substituents, 1.5% molar of ICPETS-sorbitol was incorporated into the hybrid SiNPs by calculation. The incorporation percentage of ICPTE-sorbitol was much lower than the initial molar ratio of ICPTES-sorbitol that added to the reaction solution. The excess of ICPTES-sorbitol was removed by centrifugation.

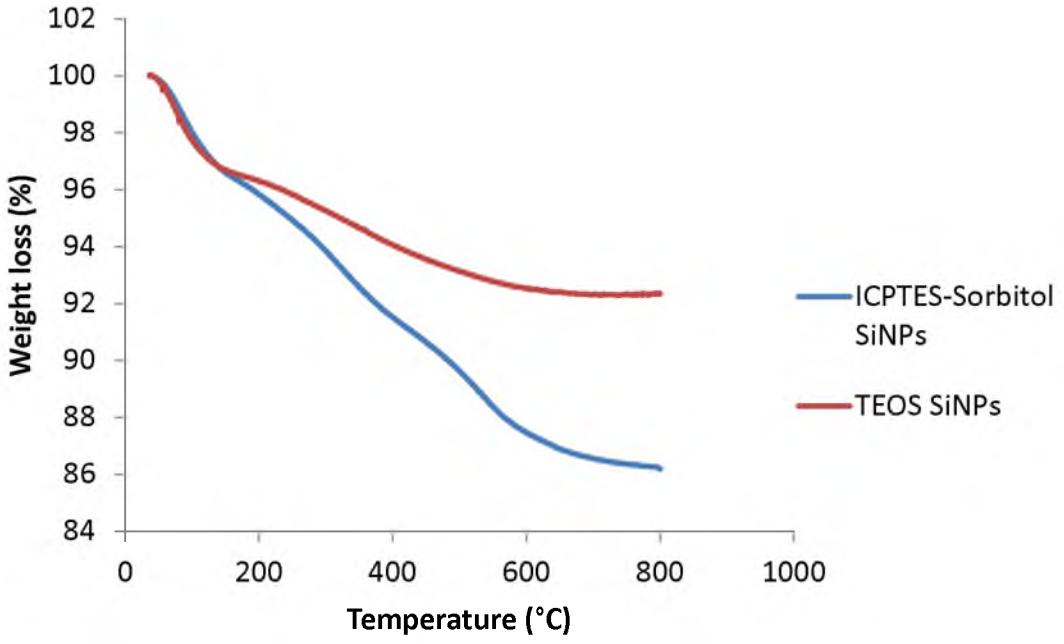

Figure 4.12. TGA data of ICPTES-sorbitol SiNPs and TEOS SiNPs

4.3.6 Degradability of ICPTES-Sorbitol SiNPs

The ICPTES-sorbitol has carbamate groups that are easily hydrolyzed in acidic solutions (Figure 4.13).[28] Carbamate hydrolysis half-lives range from seconds to 10^5 years depending on the substituent groups. In our case, the ICPTES-sorbitol is a primary carbamate which hydrolyzes much faster than the secondary carbamates.

To study the hydrolysis of ICPTES-sorbitol SiNPs, zeta potential measurememts, IR, and colorimetric spectroscopic methods were employed. The ICPTES-sorbitol SiNPs were suspended in HCl aqueous solution (pH=4) and, after 12 days, the particles were collected from the solution and washed with water to remove the HCl. The particles were redispersed in water. The zeta potential measurements of fresh ICPTES-sorbitol SiNPs were compared to that of particles treated with acid (Table 4.5). The zeta potential of

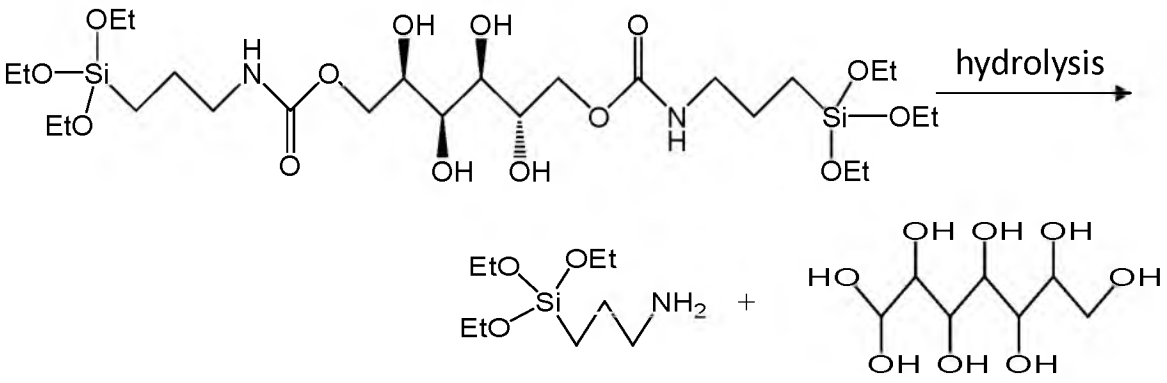

Figure 4.13. Hydrolysis of ICPTES-sorbitol.

Table 4.5. Zeta potential of ICPTES-sorbitol NPs

Sample	**Zeta-Potential**
ICPTES-Sorbitol-TEOS	-44.3±0.5 mV
ICPTES-Sorbitol-TEOS-HCl 12d	42.0±0.8 mV

fresh ICPTES-sorbitol SiNPs was similar to the Stöber particles where the large negative charge results from the surface silanol groups. For ICPTES-sorbitol SiNPs treated with acid for 12 days, the positive zeta potential demonstrated that the dominant groups on the SiNPs had changed from silanols to positively charged groups.

There are several possible hydrolysis products: carboxylic acids or primary amines according to the mechanism of carbamate hydrolysis. Since the zeta potential of

the hydrolyzed particles was positive, we believe that the ICPTES-sorbitol hydrolyzed into primary amines in the silica network. In order to verify our assumption, a colorimetric experiment was designed. Dansyl chloride is a fluorescent dye that emits green fluorescence after adduct formation with primary amines. Several ICPTES-sorbitol suspensions at different pH were prepared along with suspensions of Stöber particles for reference. After the addition of 3 drops of dansyl chloride solution, the ICPTES-sorbitol suspension treated at pH 4-8 exhibited green fluorescence under the UV light indicating the presence of primary amines on the particles. On the other hand, the ICPTES-sorbitol SiNPs treated at pH 2 solution and the Stöber particles showed no obvious fluorescent emission (Figure 4.14). This is in agreement with the report from the Yeh group that silica nanotubes were resistant to degradation at very acidic conditions.[29] One can take

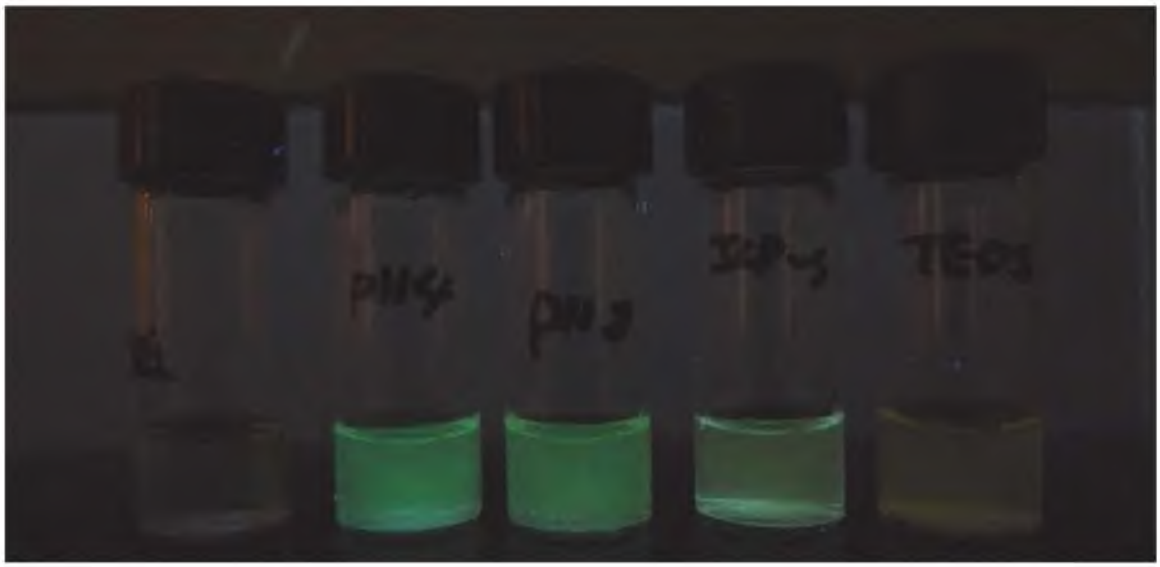

Figure 4.14. Dansyl chloride reacted with primary amines from the hydrolysis of the particles: (left to right) ICPTES-sorbitiol SiNPS in pH 2, pH 4, pH 8, pH 7, TEOS NPs in pH 7 aqueous solutions.

advantage of the degradation resistance at low pH value of ICPTES-sorbitol SiNPs in the application of oral-based drug carriers, since it will withstand the acidic environment in the stomach but degrade in the neutral to slightly acidic conditions.

The hydrolysis of the particles was also studied by IR spectrometry. 10 mg of ICPTES-sorbitol SiNPs were placed in 3 mL of aqueous HCl solutions for 1 week, and IR spectra of the supernatants were measured. As shown in the IR spectra, the supernatant of ICPTES-sorbitol SiNPs in pH 4 solution showed traces of the hydroxyl group vibration stemming from the release of sorbitol by the hydrolysis process. Meanwhile, there was no obvious sorbitol signal in the IR spectrum of ICPTES-sorbitol SiNPs supernatant obtained at pH 2. (Figure 4.15) The as-made ICPTES-sorbitol SiNPs and degraded ICPTES-sorbitol SiNPs were collected by centrifugation and measured gravimetrically. The weight losses of the as-synthesized ICPTES-sorbitol SiNPs, and the ICPTES-sorbitol SiNPs after incubation in the acidic solutions successively are shown in Table 4.6. The ICPTES-sorbitol SiNPs lost weight due to degradation; the particles degrade more in pH 4 solution compared to pH 2 solution.

In order to elucidate the degradation mechanism of the ICPTES-sorbitol SiNPs, the particles were redispersed in aqueous solutions for different time spans, and the morphology evolution during the degradation process was investigated by SEM and TEM. The ICPTES-sorbitol-2 sample degraded into irregularly shaped silica species under the acidic condition for 2 weeks. In contrast, the Stöber SiNPs maintained their spherical shape and diameter (Figure 4.16).

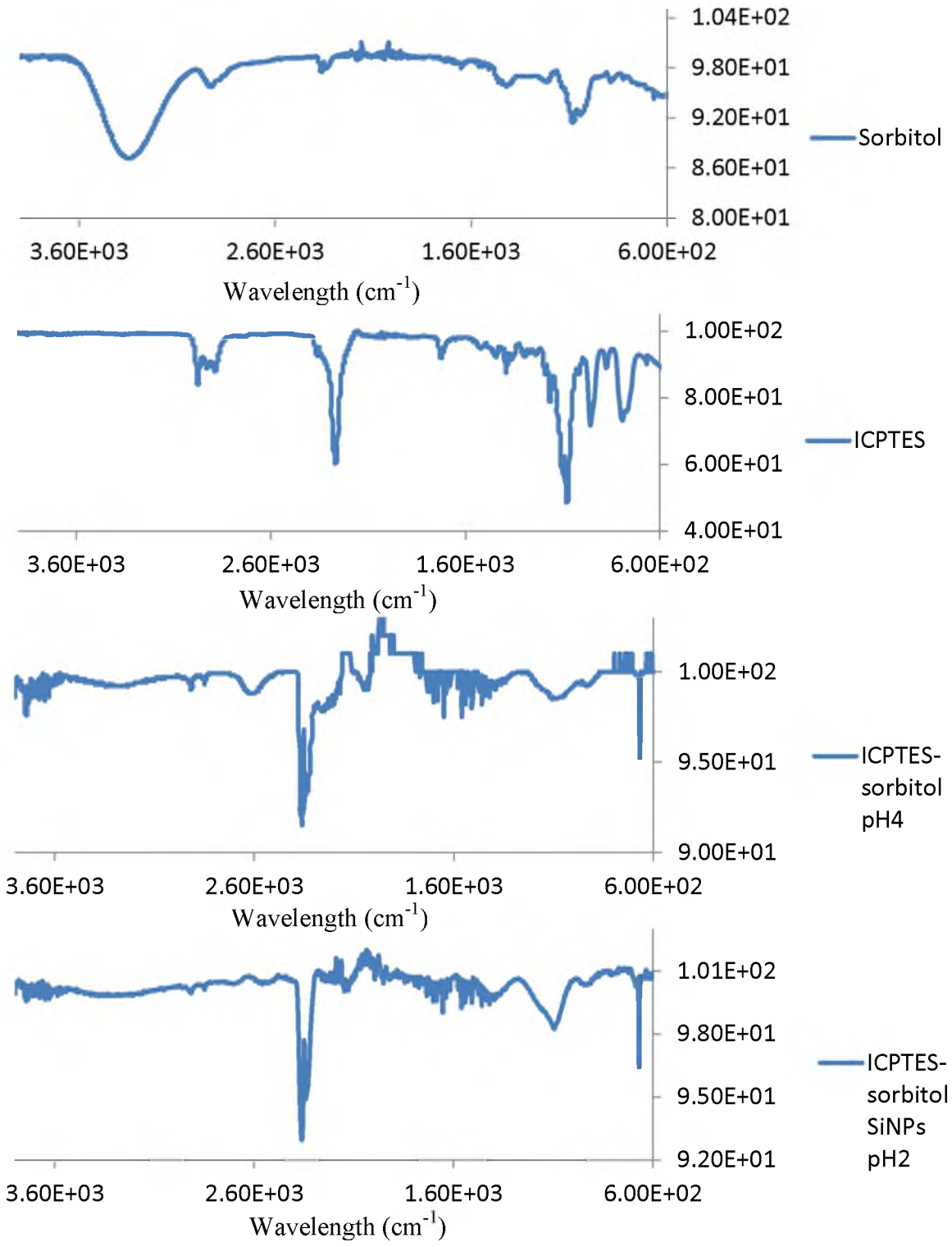

Figure 4.15. IR spectra of sorbitol, ICPTES, ICPTES-sorbitol SiNPs pH 4 supernatant and pH 2 supernatant.

Table 4.6. The weight loss of ICPTES-sorbitol is acidic solutions

ICPTES-sorbitol SiNPs initial	**ICPTES-sorbitol SiNPs pH2 1 week**	**ICPTES-sorbitol SiNPs pH4 1 week**
9.50 mg	6.64 mg	4.46mg

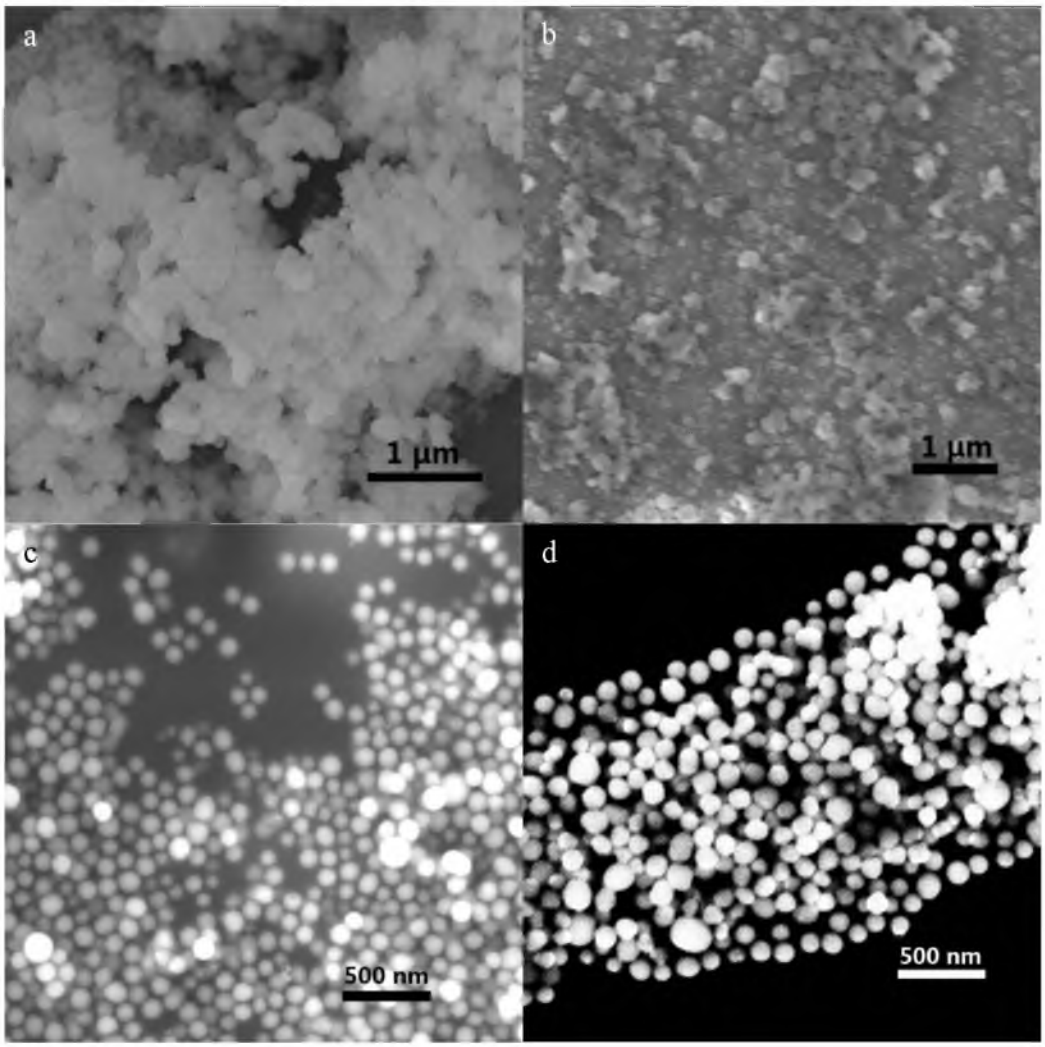

Figure 4.16. SEM images of a) ICPTES-sorbitol-2 SiNPs b) ICPTES-sorbitol-2 SiNPs in HCl solution for 2 weeks c) TEOS SiNPs d) TEOS SiNPs in HCl solution for 2 weeks.

The degradation of ICPTES-sorbitol SiNPs was demonstrated by various characterization methods, but the diameter of the monodisperse spherical ICPTES-sorbitol-7 (referred as to ICPTES-sorbitol) SiNPs remained unchanged in aqueous solutions according to the SEM images (Figure 4.17). The SEM images revealed that the ICPTES-sorbitol SiNPs neither deformed into irregular shaped silica clusters, or shrunk their size in either acidic or neutral conditions.

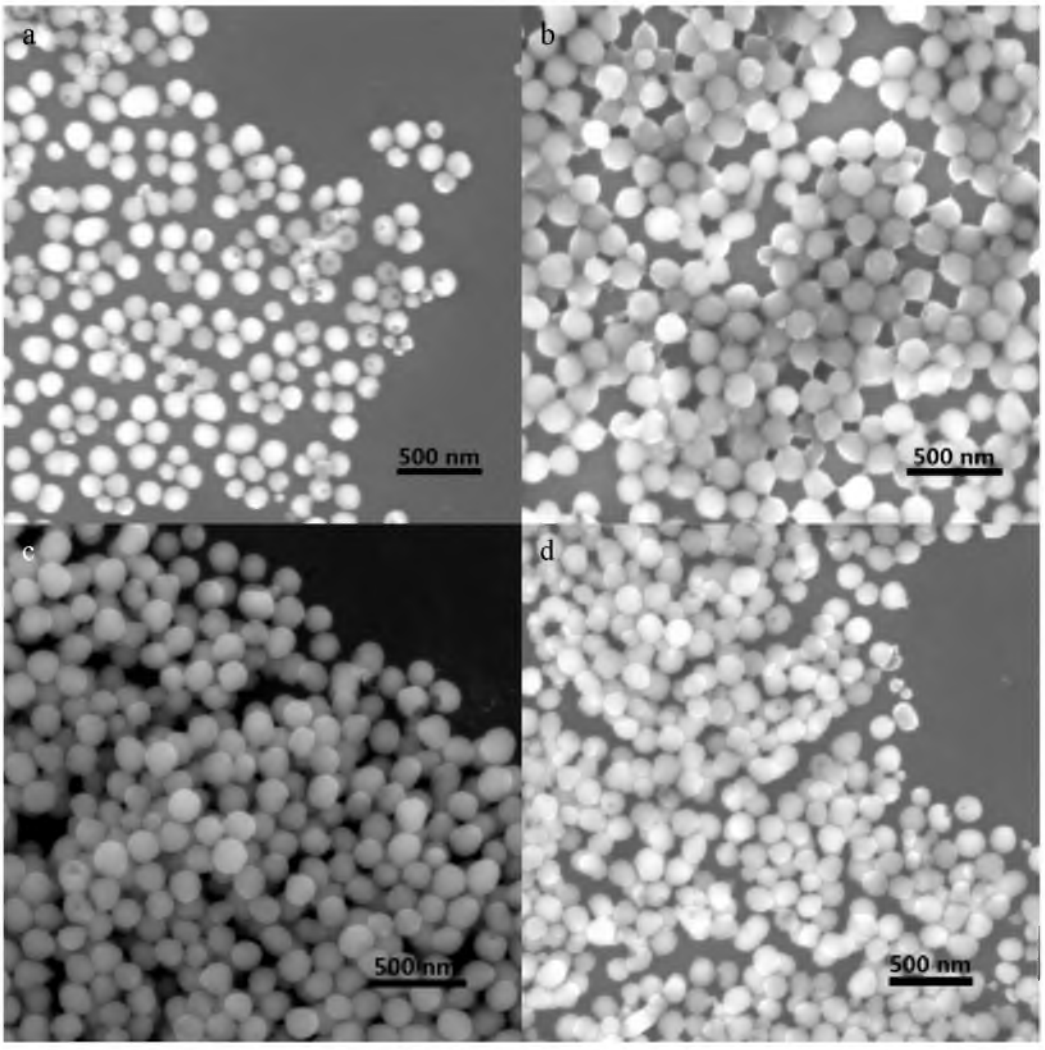

Figure 4.17. SEM images of ICPTES-sorbitol SiNPs a) in pH 4 solution for 1 days b) in pH 4 solution for 7 days c) in water for 1 days d) in water for 7 days.

Since SEM is restricted to the surface morphology detection, TEM (which is able to reveal the internal structure of the materials) was employed to study the transformation of ICPTES-sorbitol nanospheres due to the degradation. Figure 4.18 shows typical TEM images of ICPTES-sorbitol and Stöber SiNPs after different degradation times in water. The TEM images showed that the as-made ICPTES-sorbitol SiNPs were solid with slightly rough surfaces, and became porous after immersion in water. Instead of degradation from the external surfaces, the spherical ICPTES-sorbitol SiNPs maintained their general appearances and uniform sizes, and degraded inside the spheres creating porosity. In contrast, the TEOS SiNPs retained their morphology and remained nonporous, even after a month of immersion in water. All the latter ICPTES-sorbitol SiNPs gradation experiments were done in water since the aforementioned measurement demonstrated that ICPTES-sorbitol hydrolysed in water, and the pure millipore water is a more simple medium in which to study compared to acidic solutions.

Quantitative study of the nanoparticle morphology was carried out by nitrogen sorption analysis. Figure 4.19 presents the nitrogen sorption isotherms for ICPTES-sorbitol particles before and after hydrolysis. The sorption isotherm of as-made ICPTES-sorbitol SiNPs exhibited a type II isotherm corresponding to a macroporous structure or a nonporous structure with rough surface. An additional capillarity condensation at the high relative pressure was caused by textural roughness. A type IV isotherm of ICPTES-sorbitol SiNPs verb (ending –ed) in water for a week indicated a mesoporous structure. There were two hysteresis loops in the isotherm of degraded ICPTES-sorbitol SiNPs. The hysteresis loop at lower relative pressure from 0.2 to 0.8 P/P_o was attributed to the filling

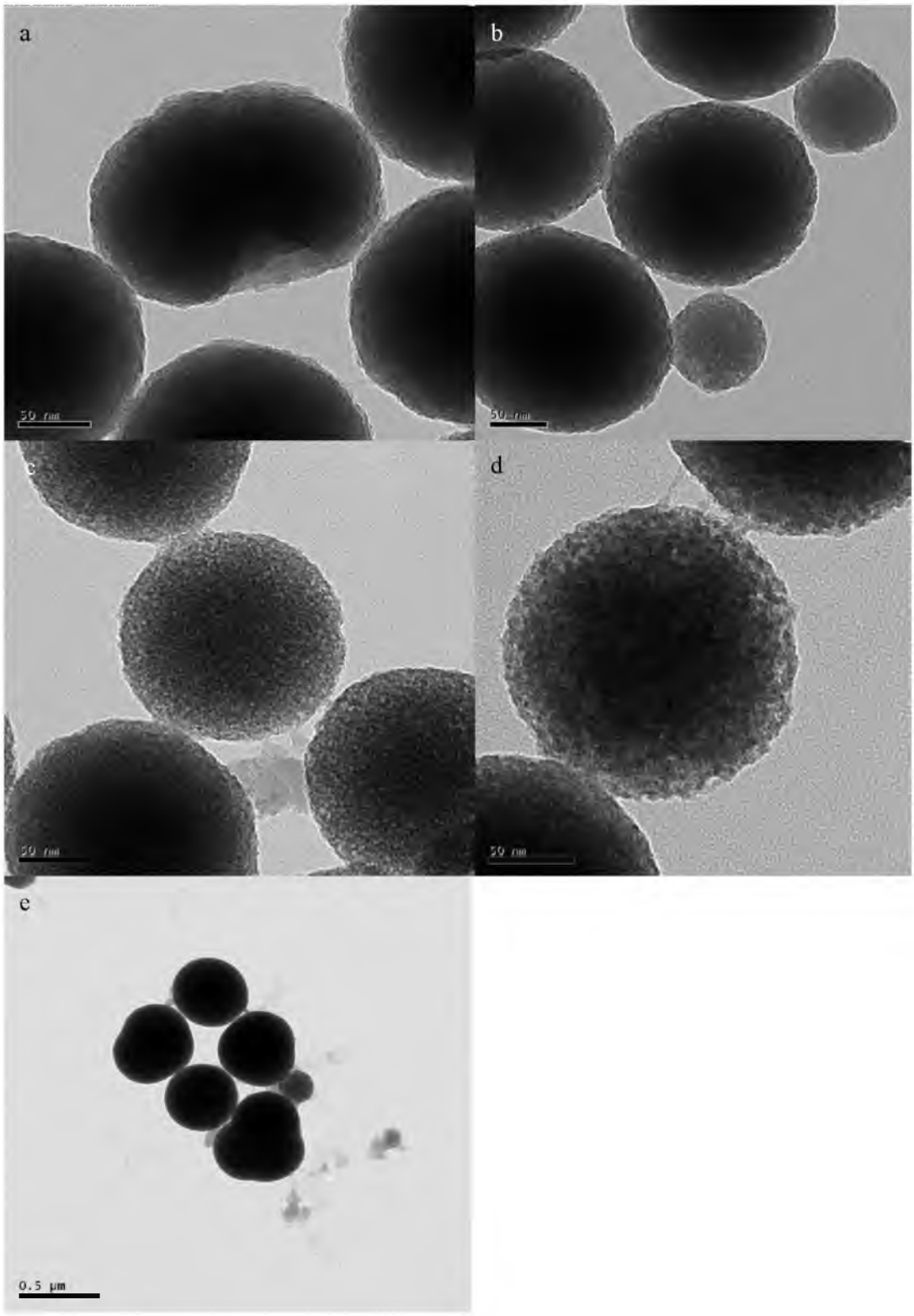

Figure 4.18. The TEM images of ICPTES-Sorbitol SiNPs in a) Ethanol; b) aqueous solution for 2 days; c) aqueous solution for 7 days; d) aqueous solution for a month e) TEOS SiNPs in water for a month.

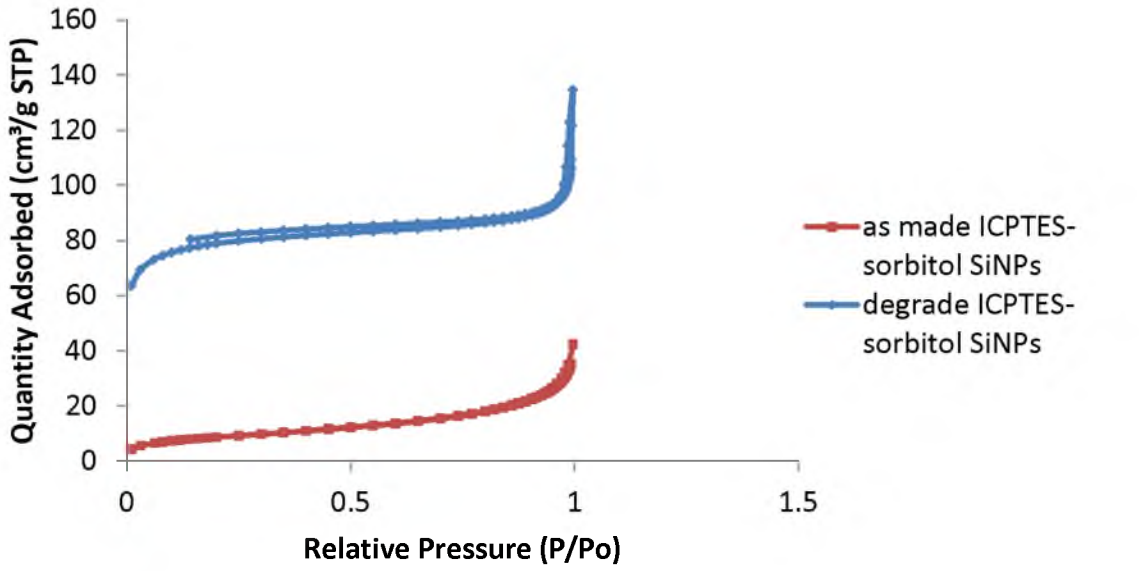

Figure 4.19. Sorption isothermals of ICPTES-sorbitol SiNPs before (red) and after (Blue) immersion in water for a week.

of the mesopores, and the broad range of the relative pressure where the loop was located indicating the wide distribution of the pore-size. The second hysteresis loop located at 0.9 P/P_o was due to the interparticle aggregation. The Brunauer-Emmett-Teller (BET) surface area was 31.0 m^2/g and 266.5 m^2/g for ICPTES-sorbitol particle before and after the degradation, respectively. The hydrolysed particles displayed a broad distribution of pore sizes, which centred around 7.1 nm in diameter as determined by the BJH method.

The major silica dissolution product is monosilicic acid, which is nontoxic and can be transferred through the tissues, enter blood vessels, and eventually be excreted with urine.[30] There are two quantitative methods that can be used to measure the amount of silicic acid. Inductively coupled plasma optical emission spectroscopy (ICP-OES) is used as a bulk analysis method to quantify the trace amounts of elements in solution.[31] We measured the degradation rate of ICPETS-sorbitol using the alternatve, well-established molybdenum blue colorimetric method. The degradation product, $Si(OH)_4$,

was detected by the reaction of molybdic acid with $Si(OH)_4$, leading to yellow silicomolybdate. To increase the spectrophotometric sensitivity, the silicomolybdate was further reduced by hydrated ammonium iron sulfate to yield silicomolybdenum blue complex. This method has been used to detect trace concentrations of monosilicic acids by recording the UV-vis absorbance at 810 nm of silicomolybdenum blue complex.[23,32,33]

ICPTES-sorbitol SiNPs and SiNPs synthesized by Stöber method were dispersed in millipore water. Aliquots of each suspension were taken out and centrifuged hourly for the first 5 h and then every 24 h. The supernatants were analyzed by the molybdenum blue method. Figure 4.20 shows that the degradation of ICPTES-sorbitol SiNPs was much faster compared to the Stöber method particles, which almost did not dissolve in water. The fast degradation was not only due to the cleavage of carbamate groups, but also because of the higher surface area caused by the resulting porous structure, which increased the contact area between the silica and water. The ICPTES-sorbitol SiNP degradation proceeds by a fast bulk degradation within the first several hours followed by slower degradation, in agreement with other reports on the degradation behavior of mesoporous silica materials.[31,34,35]

Several reports describing the degradation behavior of mesoporous silica nanoparticles were published recently.[34-39] The highly-ordered mesoporous structure was eventually destroyed in phosphate buffer or simulated human serum. Since our particles became porous during the degradation, we believe that the increasing porosity destabilizes the silica matrix. Figure 4.21 shows that some of the ICPTES-sorbitol SiNPs started to fall apart after the immersion in water for 2 months. This slow degradation attributed to the saturation of the silica species in the solution since the ICPTES-sorbitol

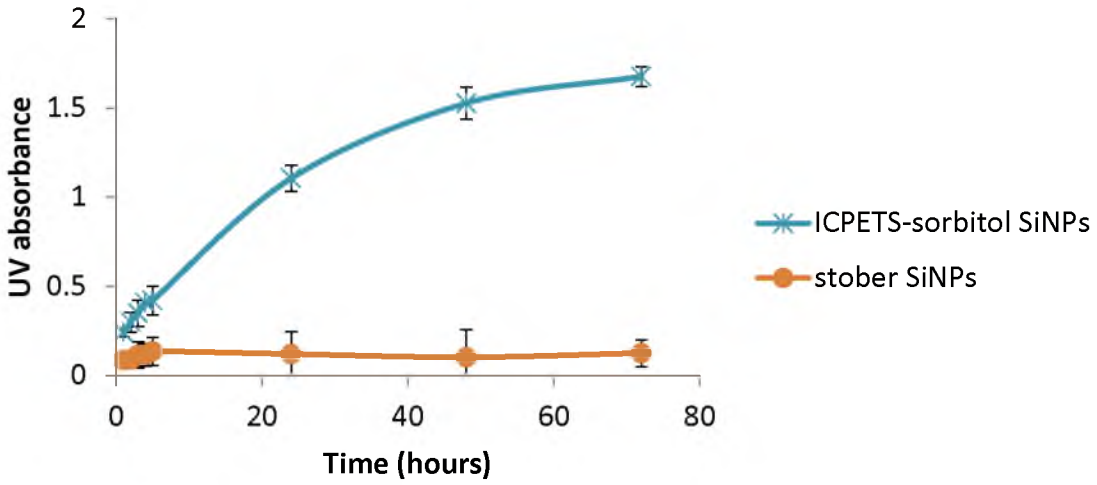

Figure 4.20 Molybdenum blue tests result of ICPTES-sorbitol and TEOS SiNPs dissolution in milipore water.

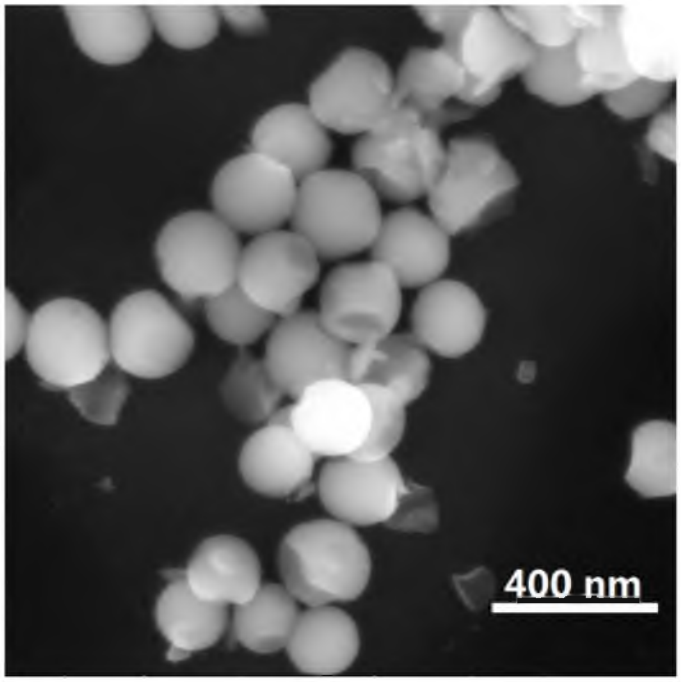

Figure 4.21. SEM image of ICPTES-sorbitol SiNPs in aqueous solution for 3 months.

SiNPs were suspended in the same solution constantly. A faster degradation behavior would be observed if a flow system was used, continuously refreshing the solvent.

4.4 Conclusion

Our work aimed to address the limitation of in vivo silica nanoparticles applications due to their undesirable bioaccumulation by producing novel degradable SiNPs via the incorporation of organic groups. Bridged silsesquioxanes CME-APTES, ICPTES-EG and ICPTES-sorbitol were synthesized and used as silica precursors to produce nanoparticles. CME-APTES produced micro-sized SiNPs with degradability in acidic aqueous solution. SiNPs were produced from CME-APTES, ICPTES-EG and ICPTES-sorbitol by co-condensation with TEOS. Although CME-APTES, CME-APTES-TEOS and ICPTES-EG-TEOS SiNPs were degradable in acidic aqueous solution, their application was limited due to the sever agglomeration. Multiple analysis methods were used to characterize the ICPTES-Sorbitol SiNPs, and confirmed that the carbamate linkage of the precursor decomposed in aqueous solutions. Novel SiNPs, with water-contact triggered porosity and active amine groups in the pores, are of great interest for future biomedical applications.

4.5 References

[1] Onclin, S.; Ravoo, B. J.; Reinhoudt, D. N., *Angew. Chem. Int. Edit.* **2005**, *44*, 6282-6304.

[2] Xu, Z. P.; Zeng, Q. H.; Lu, G. Q.; Yu, A. B. *Chem. Eng. Sci.* **2006**, *61*, 1027-1040.

[3] Jutzi, P.; Schubert, U. Silicon chemistry: from the atom to extended systems. Wiley-VCH, **2003**.

[4] a) He, Q.; Shi, J. *J. Mater. Chem.* **2011**, *21*, 5845−5855. b) He, X.; Nie, H.; Wang, K.; Tan, W.; Wu, X.; Zhang, P. *Anal. Chem. (Washington, DC, U. S.)* **2008**, *80*, 9597−9603. c) Huang, X.; Li, L.; Liu, T.; Hao, N.; Liu, H.; Chen, D.; Tang, F. *ACS Nano* **2011**, *5*, 5390−5399. d) Barbe, C.; Bartlett, J.; Kong, L.; Finnie, K.; Lin, H. Q.; Larkin, M.; Calleja, S.; Bush, A.; Calleja, G. *Adv. Mater. (Weinheim, Ger.)* **2004**, *16*, 1959−1966.

[5] Kortesuo, P.; Ahola, M.; Karlsson, S.; Kangasniemi, I.; Yli-Urpo, A.; Kiesvaara, J. *Biomaterials* **2000**, *21*, 193−198.

[6] Radin, S.; El-Bassyouni, G.; Vresilovic, E. J.; Schepers, E.; Ducheyne, P. *Biomaterials* **2005**, 26, 1043−1052.

[7] Viitala, R.; Jokinen, M.; Maunu, S. L.; Jalonen, H.; Rosenholm, J. B. *J. Non-Crystal. Solids* **2005**, *351*, 3225-3234.

[8] Livage, J.; Coradin, T.; Roux, C.; *J. Phys. Condes. Matter* **2001**, *13*, R673-R691.

[9] Radin, S.; El-Bassyouni, G.; Vresilovic, E. J.; Schepers, E.; Ducheyne, P. *Biomaterials* **2005**, *26*, 1043-1052.

[10] Kortesuo, P.; Ahola, M.; Karlsson, S.; Kangasniemi, I.; Yli-Urpo, A.; Kiesvaara, J. *Biomaterials* **2000**, *21*, 193-198.

[11] Avnir, D.; Zalzberg, L. *J. Sol-Gel. Sci. Technol.* **2008**, *48*, 47-50.

[12] Xue, J. M.; Tan, C. H.; Lukito, D. *J. Biomed. Mater. Res. B:* **2006**, *78B*, 417-422.

[13] Li, X.; Zhang, L.; Dong, X.; Liang, J.; Shi, J. *Microporous Mesoporous Mater.* **2007**, *102* (1−3), 151−158.

[14] Mitchell, K. K. P.; Liberman, Alexander; Kummel, A. C.; Trogler, W. C. *J. Am. Chem. Soc.* **2012**, *134*, 13997−14003.

[15] Stöber, W.; Fink, A.; Bahn, E. *J. Collid. Interface Sci.* **1968**, *26*, 62-69.

[16] Brozek, E. M.; Zharov, I. *Chem. Mater.*, **2009**, *21*, 1451-1456.

[17] Mizoshita, N.; Tani, T.; Inagaki, S. *Chem. Soc. Rev.*, **2011**, *40*, 789–800.

[18] Hu, L. –C.; Shea, K. J. *Chem. Soc. Rev.*, **2011**, *40*, 688–695.

[19] Hoffmann, F.; Fröba, M. *Chem. Soc. Rev.*, **2011**, *40*, 608–620.

[20] Khiterer, M.; Shea, K. J. *Nano Lett.* **2007**, *7*, 2684-2687.

[21] Hérault, D.; Rodembusch, F.; Campo, L.; Gingras, M.; Cerveau, G.; Corriu, R. J. P. *C. R. Chimie*, **2012**, *13*, 566-574.

[22] Wang, W.; Gu, B.; Liang, L.; Hamilton, W. *J. Phys. Chem. B* **2003**, *107*, 3400.

[23] Spinde, K.; Kammer, M.; Freyer, K.; Ehrlich, H.; Vournakis, J. N.; Brunner, E. *Chem. Mater.* **2011**, *23*, 2973–2978.

[24] Guo, X.; Bin, G.; Sun, X.; Zhang, Q.; Shi, T. *Chin. J. Chem.* **2011**, *29*, 363-368.

[25] Coenen, S; De Kruif, C. J. *J. Collid. Interface Sci.* **1988**, *124*, 104-110.

[26] Jamieson, P. R. *Alternative Sweeteners* (4th Edition) **2012**, 333-347.

[27] Hiramatsu, H.; Osterloh, F. E. *Langmuir* **2003**, *19*, 7003-7011.

[28] Vacondio, F.; Silva, C.; Marco, M.; Testa, B. *Drug Metabolism Reviews*, **2010**, *42*(4), 551–589.

[29] Hu, K. W.; Hsu, K. C. Yeh, C. S. *Biomaterials* **2010**, *31*, 6843-6848.

[30] Popplewell, J. F.; King, S. J.; Day, J. P.; Ackrill, P.; Fifield, L. K.; Cresswell, R. G. *J Inorg Biochem* **1998**, *69*, 177-180.

[31] Chen, K.; Zhang, J.; Gu, H. J. *Mater. Chem.*, **2012**, *22*, 22005–22012.

[32] Coradin, T; Eglin, D.; Livage, J. *Spectroscopy* **2004**, *18*, 567–576.

[33] Flocha, J.; Blaina, S.; Birotb, D.; Treguer, P. *Analytica Chimica Acta* **1998**, *377*, 157-166.

[34] He, Q.; Shi, J.; Zhu, M.; Chen, Y.; Chen. F *Micropor. Mesopor, Mater.* **2010**, *131*, 314-320.

[35] Yamada, H.; Urata, C.; Aoyama, Y.; Osada, S.; Yamauchi, Y.; Kuroda, K. *Chem. Mater.* **2012**, *24*, 1462-1471.

[36] Mortera,R.; Fiorilli, S.; Garrone, E.; Verné, E.; Onida, B. *Chem. Eur. J.,* **2010**, *156*, 184–192.

[37] Bass, J. D.; Grosso, D.; Boissiere, C.; Belamie, E.; Coradin, T.; Sanchez, C. *Chem. Mater*., **2007**, *19*, 4349–4356.

[38] Lin, Y. S.; Abadeer, N.; Haynes, C. L. *Chem. Commun*., **2011**, *47*, 532–534.

[39] Guthrie, C. P.; Reardon, E. J. *J. Phys. Chem*. A, **2008**, *112*, 3386–3390.

CHAPTER 5

CONCLUSIONS AND FUTURE DIRECTIONS

5.1 Conclusions

Design and synthesis of novel inorganic and organic/inorganic hybrid nanomaterials plays a crucial role in materials chemistry. In this thesis, we described the preparation of several new functional, inorganic and organic-inorganic hybrid nanoparticles, and characterized their properties with an eye on the potential bio-medical applications. Bio-compatible boron nanoparticles (BNPs) were produced by ligand exchange on fatty acid-covered boron nanoparticles. We demonstrated that the rigid bidentate diols replacing fatty acid on boron is a versatile ligand exchange strategy. The low cytotoxicity and easy cellular uptake make the prepared dopamine-coated BNPs (DA-BNPs) promising materials for Boron Neutron Capture Therapy (BNCT). Tannic Acid (TA) was used for the first time as a pore-directing agent to produce novel mesoporous silica nanoparticles (MSNs). The resulting particles possessed large pore size, unique pore structure, a narrow size distribution around 200 nm, and could immobilize proteins and enzymes. The tannic acid-templated mesoporous silica nanoparticles (TA-TEOS) may inspire the use of other nonsurfactant molecules as templates to produce MSNs. The study of protein immobilization suggested that electrostatic interaction and hydrogen bonding interaction are the important forces for protein adsorption on silica materials. The rate of protein adsorption on MSN is related to the sizes of the proteins:

the smaller the protein, the faster it reaches the adsorption saturation. The immobilization of the enzymes in TA-TEOS enhanced the thermal stability of the enzymes. Hybrid silica nanoparticles (SiNPs) were produced by incorporating hydrolysable silsesquioxanes into the silica matrix. The resulting particles showed different degradation behaviors depending on their composition. The ICPTES-sorbitol SiNPs displayed interesting degradation behavior, where the solid particles became porous after the hydrolysis. This project demonstrated the possibility of using bridged silsesquioxane with cleavable linkers to produce degradable SiNPs. It will inspire the preparation of novel SiNPs by bridged silsequioxanes with other cleavable linkers, such as the ones that respond to external stimuli.

Overall, this work described several strategies to produce novel boron and silica nanoparticles providing information about rationally designing nanoparticles for biomedical applications. It is of particular value for the fundamental studies of protein-silica interactions and silica material degradation behaviors.

5.2 Future directions

The long-term objective of the projects should be to explore the bio-medical applications of these novel NPs. This utility is governed by their toxicity. The in vitro study of the novel particles should be the next step. Although we obtained promising results in the preliminary study of DA-BNPs with the macrophage cell line, systematic *in vitro* studies of the particles, with varied concentrations and for various mammalian cell lines, are required to obtain a conclusive description of the BNPs behavior in vitro. This should be followed by cell targeting studies, both in vitro and in vivo using surface ligands, targeting receptors that are over-expressed on the cancer cells, such as folate

receptors,[1,2] or antibodies selective for tumor-associated receptors.[3] Targeting cancer cells with BNPs using the Enhanced Permeability and Retention (EPR) effect[4] should be studied also.

Our studies of new mesoporous silica nanoparticles showed that, although the immobilization of Malic Dehydrogenase (MDH) in TA-TEOS increases the stability of the enzymes at room temperature, the immobilization did not enhance the catalysis activity of m-MDH. There are reports suggesting that the change of the enzyme conformation due to the incorporation inside mesopores enhances the activity of the enzymes.[5] Thus, we should systematically study the influence of the pore size on the activity of the immobilized enzymes by encapsulation of MDH in TA-TEOS with different pore diameters.

Surface characteristics are important for the adsorption of proteins. Lei et al. showed that a higher amount of protein could be adsorbed, and protein stability was enhanced by choosing the optimal amount of functional groups on the surface of the mesopores.[6] Serra et al. showed that hydrophobic interactions between lipases and a methyl-functionalized surface preserved a higher catalytic activity of the adsorbed enzyme.[7] We should modify the TA-TEOS with multiple functional groups, and study the adsorption of the proteins and the interactions between the proteins and functionalized silica particles.

The TA templated mesoporous SiNPs has many other potential applications, including chromatography, membrane separations and adsorbtion. Mesoporous silica particles might be good candidates for hydrogen storage materials due to their large surface area and pore volume. However, there are only a few reports on the application of

MSNs for this purpose. Buckley et al. reported that MCM-41 at 77 K can reversibly absorb 1.6 wt% of hydrogen at 1.5 MPa.[8] We tested the hydrogen storage ability of TA-TEOS at room temperature and under 1.5 MPa, but observed no hydrogen absorption. We may encapsulate palladium in the pores[9] by reducing the palladium ions to achieve hydrogen storage. Since TA-TEOS has disordered and interconnected pore morphology, they may trap palladium nanoparticles more efficiently compared to conventional MSN with 2D channels.

It will be interesting to explore the ability of other molecules with rigid structures and multiple hydroxyl groups to perform as a pore-directing agent to produce the MSNs.

5.3 References

[1] Low, P. S.;Henne,W.A.;Doorneweerd, D. D. **Acc. Chem. Res. 2008**, *41*, 120-129.

[2] Lee, S.-M.; Chen, H.; O'Halloran, T. V.; Nguyen, S. T. *J. Am. Chem. Soc.* **2009**, *131*, 9311-9320.

[3] Randy, L.; Seo, S. S. *Analytical Letters*, Ahead of Print

[4] Blanco, E.; Hsiao, A.; Mann, A. P.; Landry, M. G.; Meric-Bernstam, F.; Ferrari, M. *Cancer Sci.* **2011**, *102*, 1247-1252.

[5] Teichroeb, J. H.: Forrest J. A.; Jones, L. W. *Eur. Phys. J. E*, **2008**, *26*, 411-415.

[6] C. Lei, Y. Shin, J. Liu and E. J. Ackerman, *J. Am. Chem. Soc.,* **2002**, *124*, 11242-11243.

[7] Serra, E.; Mayoral, A.; Sakamoto,Y.; Blanco R. M. ; Díaz, I. *Microporous Mesoporous Mater.*, **2008**, *114*, 201-213.

[8] Sheppard, D. A.; Maitland, C. F.; Buckley, C. E. J. Alloy. Compd. **2005**, 404-408.

[9] Schlapbach, L.; Züttel, A. *Nature* **2001**, *414*, 353-358.